

REPORT DOCUMENTATION PAGE				Form Approved OMB NO. 0704-0188	
<p>The public reporting burden for this collection of information is estimated to average 1 hour per response, including the time for reviewing instructions, searching existing data sources, gathering and maintaining the data needed, and completing and reviewing the collection of information. Send comments regarding this burden estimate or any other aspect of this collection of information, including suggestions for reducing this burden, to Washington Headquarters Services, Directorate for Information Operations and Reports, 1215 Jefferson Davis Highway, Suite 1204, Arlington VA, 22202-4302. Respondents should be aware that notwithstanding any other provision of law, no person shall be subject to any penalty for failing to comply with a collection of information if it does not display a currently valid OMB control number.</p> <p>PLEASE DO NOT RETURN YOUR FORM TO THE ABOVE ADDRESS.</p>					
1. REPORT DATE (DD-MM-YYYY) 23-10-2013		2. REPORT TYPE Final Report		3. DATES COVERED (From - To) 1-Jul-2007 - 30-Sep-2012	
4. TITLE AND SUBTITLE Ultrasmall Microfabricated Laser Cavities				5a. CONTRACT NUMBER W911NF-07-1-0277	
				5b. GRANT NUMBER	
				5c. PROGRAM ELEMENT NUMBER 7D10AI	
6. AUTHORS Oskar Painter, Eli Yablonovitch, Axel Scherer				5d. PROJECT NUMBER	
				5e. TASK NUMBER	
				5f. WORK UNIT NUMBER	
7. PERFORMING ORGANIZATION NAMES AND ADDRESSES California Institute of Technology Sponsored Research MC 201-15 1200 E. California Blvd. Pasadena, CA 91125 -0001				8. PERFORMING ORGANIZATION REPORT NUMBER	
9. SPONSORING/MONITORING AGENCY NAME(S) AND ADDRESS(ES) U.S. Army Research Office P.O. Box 12211 Research Triangle Park, NC 27709-2211				10. SPONSOR/MONITOR'S ACRONYM(S) ARO	
				11. SPONSOR/MONITOR'S REPORT NUMBER(S) 53043-EL-DRP.18	
12. DISTRIBUTION AVAILABILITY STATEMENT Approved for Public Release; Distribution Unlimited					
13. SUPPLEMENTARY NOTES The views, opinions and/or findings contained in this report are those of the author(s) and should not be construed as an official Department of the Army position, policy or decision, unless so designated by other documentation.					
14. ABSTRACT Established cavity designs for commercial semiconductor lasers are mostly based on Fabry-Perot etalons for edge or surface emission. Similar to the trend of miniaturization of integrated electronics, there is a quest to shrink the size of semiconductor lasers, in order to pack more devices on less material and in the hope of modifying the laser efficiency with control over spontaneous emission in tiny cavities. In this program, we have used microdisk, vertical-cavity and photonic crystal cavities to confine light into smaller and smaller volumes.					
15. SUBJECT TERMS Microcavities, Lasers, Plasmon, Nanophotonics					
16. SECURITY CLASSIFICATION OF:			17. LIMITATION OF ABSTRACT UU	15. NUMBER OF PAGES	19a. NAME OF RESPONSIBLE PERSON Axel Scherer
a. REPORT UU	b. ABSTRACT UU	c. THIS PAGE UU			19b. TELEPHONE NUMBER 626-627-6785

Report Title

Ultrasmall Microfabricated Laser Cavities

ABSTRACT

Established cavity designs for commercial semiconductor lasers are mostly based on Fabry-Perot etalons for edge or surface emission. Similar to the trend of miniaturization of integrated electronics, there is a quest to shrink the size of semiconductor lasers, in order to pack more devices on less material and in the hope of modifying the laser efficiency with control over spontaneous emission in tiny cavities. In this program, we have used microdisk, vertical-cavity and photonic crystal cavities to confine light into smaller and smaller volumes.

Enter List of papers submitted or published that acknowledge ARO support from the start of the project to the date of this printing. List the papers, including journal references, in the following categories:

(a) Papers published in peer-reviewed journals (N/A for none)

ReceivedPaper

- 12/08/2012 2.00 Se-Heon Kim, Jingqing Huang, Axel Scherer. From vertical-cavities to hybrid metal/photonic-crystal nanocavities: towards high-efficiency nanolasers, Journal of the Optical Society of America B, (03 2012): 0. doi: 10.1364/JOSAB.29.000577
- 12/08/2012 13.00 John Liu, Yan Chen, Clive R. Taylor, Axel Scherer, Emil P. Kartalov. Elastomeric microfluidic diode and rectifier work with Newtonian fluids, Journal of Applied Physics, (2009): 0. doi: 10.1063/1.3268463
- 12/08/2012 11.00 Hyun-Joo Chang, Se-Heon Kim, Yong-Hee Lee, Emil P. Kartalov, Axel Scherer. A photonic-crystal optical antenna for extremely large local-field enhancement, Optics Express, (11 2010): 0. doi: 10.1364/OE.18.024163
- 12/08/2012 10.00 Sameer S. Walavalkar, Andrew P. Homyk, M. David Henry, Axel Scherer. Controllable deformation of silicon nanowires with strain up to 24%, Journal of Applied Physics, (2010): 0. doi: 10.1063/1.3436589
- 12/08/2012 9.00 Jingqing Huang, Se-Heon Kim, Axel Scherer. Design of a surface-emitting, subwavelength metal-clad disk laser in the visible spectrum, Optics Express, (08 2010): 0. doi: 10.1364/OE.18.019581
- 12/08/2012 8.00 Sameer S. Walavalkar, Carrie E. Hofmann, Andrew P. Homyk, M. David Henry, Harry A. Atwater, Axel Scherer. Tunable Visible and Near-IR Emission from Sub-10 nm Etched Single-Crystal Si Nanopillars, Nano Letters, (11 2010): 0. doi: 10.1021/nl102140k
- 12/08/2012 7.00 Adam C. Scofield, Se-Heon Kim, Joshua N. Shapiro, Andrew Lin, Baolai Liang, Axel Scherer, Diana L. Huffaker. Bottom-up Photonic Crystal Lasers, Nano Letters, (12 2011): 0. doi: 10.1021/nl2030163
- 12/08/2012 6.00 L. Feng, M. Ayache, J. Huang, Y.-L. Xu, M.-H. Lu, Y.-F. Chen, Y. Fainman, A. Scherer. Nonreciprocal Light Propagation in a Silicon Photonic Circuit, Science, (08 2011): 0. doi: 10.1126/science.1206038
- 12/08/2012 5.00 Jingqing Huang, Se-Heon Kim, Jonathan Gardner, Philippe Regreny, Christian Seassal, Pablo Aitor Postigo, Axel Scherer. Room temperature, continuous-wave coupled-cavity InAsP/InP photonic crystal laser with enhanced far-field emission directionality, Applied Physics Letters, (2011): 0. doi: 10.1063/1.3633120
- 12/08/2012 4.00 Sameer S. Walavalkar, Andrew P. Homyk, Carrie E. Hofmann, M. David Henry, Claudia Shin, Harry A. Atwater, Axel Scherer. Size tunable visible and near-infrared photoluminescence from vertically etched silicon quantum dots, Applied Physics Letters, (2011): 0. doi: 10.1063/1.3580768
- 12/08/2012 3.00 Jingqing Huang, Axel Scherer, Se-Heon Kim. Photonic crystal nanocavity laser in an optically very thick slab, Optics Letters, (02 2012): 0. doi: 10.1364/OL.37.000488
- 12/10/2012 16.00 R. Perahia, J. D. Cohen, S. Meenehan, T. P. Mayer Alegre, O. Painter. Electrostatically tunable optomechanical “zipper” cavity laser, Applied Physics Letters, (11 2010): 191112. doi: 10.1063/1.3515296
- 12/10/2012 17.00 R. Perahia, T. P. Mayer Alegre, A. H. Safavi-Naeini, O. Painter. Surface-plasmon mode hybridization in subwavelength microdisk lasers, Applied Physics Letters, (11 2009): 201114. doi: 10.1063/1.3266843

TOTAL:**13**

Number of Papers published in peer-reviewed journals:

(b) Papers published in non-peer-reviewed journals (N/A for none)

Received Paper

TOTAL:

Number of Papers published in non peer-reviewed journals:

(c) Presentations

Number of Presentations: 0.00

Non Peer-Reviewed Conference Proceeding publications (other than abstracts):

Received Paper

TOTAL:

Number of Non Peer-Reviewed Conference Proceeding publications (other than abstracts):

Peer-Reviewed Conference Proceeding publications (other than abstracts):

Received Paper

12/08/2012 12.00 Se-Heon Kim, Yong-Hee Lee, Jingqing Huang, Axel Scherer. Unidirectional vertical emission from photonic crystal nanolasers, 2009 11th International Conference on Transparent Optical Networks (ICTON). 2009/06/27 03:00:00, Ponta Delgada, Portugal. : ,

TOTAL: 1

(d) Manuscripts

Received

Paper

12/08/2012 14.00 Se-Heon Kim, Jingqing Huang, Axel Scherer. Higher-order defect mode laser in an optically thick photonic crystal slab, Optics Letters (accepted) (10 2012)

12/08/2012 15.00 Andrew Homyk, Sameer Walavalkar,, Axel Scherer, Se-Heon Kim. High-Q impurity photon states bounded by a photonic band pseudogap in an optically thick photonic crystal slab, Physical Review B (accepted) (09 2012)

TOTAL: 2

Number of Manuscripts:

Books

Received

Paper

TOTAL:

Patents Submitted

Methods of Fabrication of Microfluidic Systems on Printed Circuit Boards

Multi-Valve Microfluidic Devices and Methods

Photonic Crystal Cavities and Related Devices and Methods

Methods for Designing, Fabricating and Predicting Shape Formations in a Material

Method for Fabricating Self-Aligning Arrangements on Semiconductors

Chemical Sensing and/or Measuring Devices and Methods

Chemically-Etched Nanostructures and Related Devices

Patents Awarded

Multi-Valve Microfluidic Devices and Methods

Awards

Graduate Students

<u>NAME</u>	<u>PERCENT SUPPORTED</u>	Discipline
Adalian, Dvin Artashes Boghos	0.00	
dos Santos Fegadolli, William	0.00	
Homyk, Andrew Peter	0.00	
Huang, Jingqing	0.00	
Jones, William Maxwell	0.00	
Malik, Imran Raouf	0.00	
Rajagopal, Aditya	0.00	
Sadek, Akram Sarwat	0.00	
Shearn, Michael Joseph	0.00	
Walker, Christopher Ian	0.00	
Chan, Jasper	0.00	
Cohen, Justin Daniel	0.00	
Meenehan, Sean Michael	0.00	
Perahia, Raviv	0.00	
Rastogi, Chaitanya	0.00	
Nikhil Kumar	0.00	
Peter Debackere	0.00	
FTE Equivalent:	0.00	
Total Number:	17	

Names of Post Doctorates

<u>NAME</u>	<u>PERCENT SUPPORTED</u>
Kim, Seheon	0.00
Zhang, Zhaoyu	0.00
Alegre, Thiago Pedro Mayer	0.00
Camacho, Ryan	0.00
Mohageg, Makan	0.00
Perahia, Raviv	0.00
FTE Equivalent:	0.00
Total Number:	6

Names of Faculty Supported

<u>NAME</u>	<u>PERCENT SUPPORTED</u>	National Academy Member
Scherer, Axel	0.00	
Yablonovitch, Eli	0.00	
Painter, Oskar	0.00	
FTE Equivalent:	0.00	
Total Number:	3	

Names of Under Graduate students supported

<u>NAME</u>	<u>PERCENT SUPPORTED</u>	Discipline
Chen, Samson	0.00	
Gwinn, Thomas Oren	0.00	
Latawiec, Pawel Michal	0.00	
Marzen, Sarah Epstein	0.00	
Petykiewicz, Jan Aksel	0.00	
Cheng, Linlin	0.00	
Tai, Ming Eric	0.00	
FTE Equivalent:	0.00	
Total Number:	7	

Student Metrics

This section only applies to graduating undergraduates supported by this agreement in this reporting period

The number of undergraduates funded by this agreement who graduated during this period: 0.00

The number of undergraduates funded by this agreement who graduated during this period with a degree in science, mathematics, engineering, or technology fields:..... 0.00

The number of undergraduates funded by your agreement who graduated during this period and will continue to pursue a graduate or Ph.D. degree in science, mathematics, engineering, or technology fields:..... 0.00

Number of graduating undergraduates who achieved a 3.5 GPA to 4.0 (4.0 max scale):..... 0.00

Number of graduating undergraduates funded by a DoD funded Center of Excellence grant for Education, Research and Engineering:..... 0.00

The number of undergraduates funded by your agreement who graduated during this period and intend to work for the Department of Defense 0.00

The number of undergraduates funded by your agreement who graduated during this period and will receive scholarships or fellowships for further studies in science, mathematics, engineering or technology fields: 0.00

Names of Personnel receiving masters degrees

NAME

Total Number:

Names of personnel receiving PhDs

NAME

Huang, Jingqing

Shearn, Michael Joseph

Walker, Christopher Ian

Total Number:

3

Names of other research staff

NAME

PERCENT SUPPORTED

Gudlewski, Benjamin John

0.00

Shin, Claudia H

0.00

Vyawahare, Saurabh

0.00

FTE Equivalent:

0.00

Total Number:

3

Sub Contractors (DD882)

Inventions (DD882)

5 Chemical Sensing and/or Measuring Devices and Methods

Patent Filed in US? (5d-1) Y

Patent Filed in Foreign Countries? (5d-2) N

Was the assignment forwarded to the contracting officer? (5e) N

Foreign Countries of application (5g-2):

5a: Sameer Walavalkar

5f-1a: California Institute of Technology

5f-c: 1200 E California Blvd

Pasadena CA 91125

5a: Axel Scherer

5f-1a: California Institute of Technology

5f-c: 1200 E California Blvd

Pasadena CA 91125

5a: Michael D. Henry

5f-1a: California Institute of Technology

5f-c: 1200 E California Blvd

Pasadena CA 91125

5a: Andrew P. Homyk

5f-1a: California Institute of Technology

5f-c: 1200 E California Blvd

Pasadena CA 91125

5 Chemically-Etched Nanostructures and Related Devices

Patent Filed in US? (5d-1) Y

Patent Filed in Foreign Countries? (5d-2) Y

Was the assignment forwarded to the contracting officer? (5e) N

Foreign Countries of application (5g-2):

5a: Jingqing Huang

5f-1a: California Institute of Technology

5f-c: 1200 E California Blvd

Pasadena CA 91125

5a: Dong Yoon Oh

5f-1a: California Institute of Technology

5f-c: 1200 E California Blvd

Pasadena CA 91125

5a: Axel Scherer

5f-1a: California Institute of Technology

5f-c: 1200 E California Blvd

Pasadena CA 91125

5a: Seheon Kim

5f-1a: California Institute of Technology

5f-c: 1200 E California Blvd

Pasadena CA 91125

5 Method for Fabricating Self-Aligning Arrangements on Semiconductors

Patent Filed in US? (5d-1) Y

Patent Filed in Foreign Countries? (5d-2) N

Was the assignment forwarded to the contracting officer? (5e) N

Foreign Countries of application (5g-2):

5a: Sameer Walavalkar

5f-1a: California Institute of Technology

5f-c: 1200 E California Blvd

Pasadena CA 91125

5a: Michael D. Henry

5f-1a: California Institute of Technology

5f-c: 1200 E California Blvd

Pasadena CA 91125

5a: Axel Scherer

5f-1a: California Institute of Technology

5f-c: 1200 E California Blvd

Pasadena CA 91125

5a: Andrew P. Homyk

5f-1a: California Institute of Technology

5f-c: 1200 E California Blvd

Pasadena CA 91125

5 Methods for Designing, Fabricating and Predicting Shape Formations in a Material

Patent Filed in US? (5d-1) Y

Patent Filed in Foreign Countries? (5d-2) N

Was the assignment forwarded to the contracting officer? (5e) N

Foreign Countries of application (5g-2):

5a: Michael J. Shearn

5f-1a: California Institute of Technology

5f-c: 1200 E California Blvd

Pasadena CA 91125

5a: Michael D. Henry

5f-1a: California Institute of Technology

5f-c: 1200 E California Blvd

Pasadena CA 91125

5a: Axel Scherer

5f-1a: California Institute of Technology

5f-c: 1200 E California Blvd

Pasadena CA 91125

5 Methods of Fabrication of Microfluidic Systems on Printed Circuit Boards

Patent Filed in US? (5d-1) Y

Patent Filed in Foreign Countries? (5d-2) N

Was the assignment forwarded to the contracting officer? (5e) N

Foreign Countries of application (5g-2):

5a: Axel Scherer

5f-1a: California Institute of Technology

5f-c: 1200 E California Blvd

Pasadena CA 91125

5a: Aditya Rajagopal

5f-1a: California Institute of Technology

5f-c: 1200 E California Blvd

Pasadena CA 91125

5a: Christopher I. Walker

5f-1a: California Institute of Technology

5f-c: 1200 E California Blvd

Pasadena CA 91125

5 Multi-Valve Microfluidic Devices and Methods

Patent Filed in US? (5d-1) Y

Patent Filed in Foreign Countries? (5d-2) N

Was the assignment forwarded to the contracting officer? (5e) N

Foreign Countries of application (5g-2):

5a: John Liu

5f-1a: California Institute of Technology

5f-c: 1200 E California Blvd

Pasadena CA 91125

5a: Axel Scherer

5f-1a: California Institute of Technology

5f-c: 1200 E California Blvd

Pasadena CA 91125

5a: Clive Taylor

5f-1a: University of Southern California

5f-c:

5a: Emil P. Kartalov

5f-1a: California Institute of Technology

5f-c: 1200 E California Blvd

Pasadena CA 91125

5 Photonic Crystal Cavities and Related Devices and Methods

Patent Filed in US? (5d-1) Y

Patent Filed in Foreign Countries? (5d-2) N

Was the assignment forwarded to the contracting officer? (5e) N

Foreign Countries of application (5g-2):

5a: Seheon Kim

5f-1a: California Institute of Technology

5f-c: 1200 E California Blvd

Pasadena CA 91125

5a: Axel Scherer

5f-1a: California Institute of Technology

5f-c: 1200 E California Blvd

Pasadena CA 91125

Scientific Progress

Technology Transfer

DARPA/NACHOS Technical Report: W911NF-07-1-9277

Ultrasmall microfabricated laser cavities

Axel Scherer, Oskar Painter, Eli Yablonovitch

Established cavity designs for commercial semiconductor lasers are mostly based on Fabry-Perot etalons for edge or surface emission. Similar to the trend of miniaturization of integrated electronics, there is a quest to shrink the size of semiconductor lasers, in order to pack more devices on less material and in the hope of modifying the laser efficiency with control over spontaneous emission in tiny cavities. In this program, we have used microdisk, vertical-cavity and photonic crystal cavities to confine light into smaller and smaller volumes.

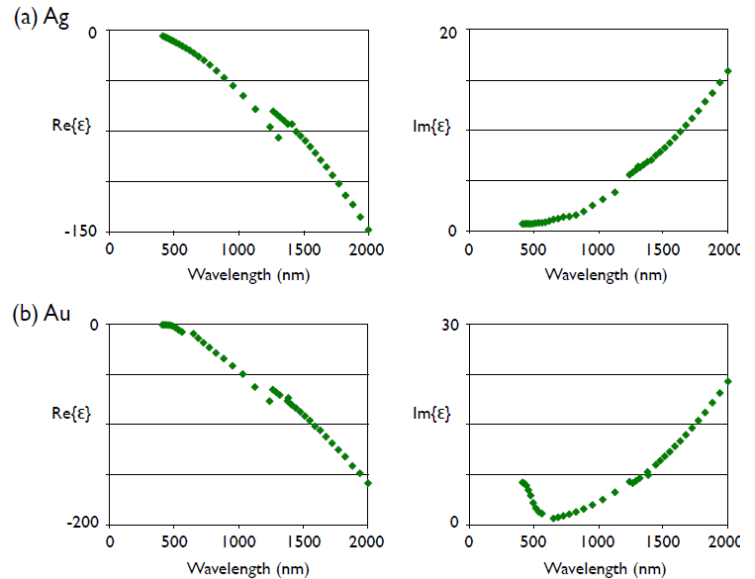
Two figures of merit are generally used to quantify a cavity design: the quality factor Q and the volume of the cavity V . To achieve strong confinement of light, one method is to use total internal reflection, which can theoretically exhibit perfect reflectivity. Disk and toroid resonators both operate on this principle. However, perfect TIR is only possible for plane waves with a narrow range of wave vectors, not when cavity size approaches wavelength scales so that the momentum space (i.e., k -space) field distribution is much broadened. Indeed, microtoroid cavities can reach Q s of 10^8 with V of over $100 (\lambda/n)^3$; microdisks have Q s of 10^6 with V around $6(\lambda/n)^3$. Yet as cavity size shrinks, light experiences only partial reflection at the dielectric-air interface; radiation loss dominates and limits the maximum achievable Q . On the other hand, carefully designed reflectors surrounding a cavity, such as periodic dielectric structures or metal mirrors, can achieve much higher Q with $V < (\lambda/n)^3$.

Drude-Sommerfeld fit of dielectric functions of silver and gold at room temperature

Material	Wavelength range	ϵ_∞	ω_p	γ_c
Silver	1260 ~ 2000 nm	1.722	1.155×10^{16}	1.108×10^{14}
	375 ~ 1240 nm	3.9943	1.329×10^{16}	1.128×10^{14}
Gold	1250 ~ 1800 nm	1	1.207×10^{16}	1.362×10^{14}
	650 ~ 1250 nm	12.99	1.453×10^{16}	1.109×10^{14}

Metals are natural reflectors due to their large negative real part of dielectric constant in a wide range of telecommunications frequencies. For microwave to far-infrared frequencies, only a negligible fraction of the electromagnetic waves penetrates into the metal; therefore, metals are often approximated as perfect conductors. At the optical frequencies of NIR and visible ranges, field penetration increases, leading to increased dissipation. At UV frequencies, however, metals acquire dielectric-like characteristics and allow the propagation of electromagnetic waves with varying degrees of attenuation. At NIR and visible wavelengths, noble metals such as gold and silver are among the most

commonly used materials, as they have large negative real dielectric constants and relatively low complex dielectric constants, leading to lower optical loss. These are plotted in Figure 1. We have developed modeling tools to design optical metallo-dielectric cavities.



Functional similarities between metals and photonic crystals

It would seem that metals and photonic crystals are very different mirrors – the former reflect light due to the materials large negative real part of the dielectric function, the latter reflect by Bragg reflection as a result of periodic dielectric structures. The same material property that makes metals reflective also leads to other interesting consequences that have captured the interest of the optics research community in recent years, namely, surface plasmon polaritons (SPP), metallic nano-antennas with hot spots of extremely concentrated light, and negative refractive index meta-materials. However, all of these metallic phenomena have counterparts in photonic crystals made of only lossless dielectrics. Surface modes can occur at the interface of air and 2D or 3D photonic crystals with dispersion relations and evanescent mode profiles similar to those of SPP, where the E-field decays evanescently into both the photonic crystal and air. The big difference between metals and photonic crystals is in essence the trade-off between size and lossiness. Metals are known to obtain their bulk plasmonic properties even when they are tiny nuggets of <10nm across. However, their positive imaginary part of the dielectric function means room temperature metallic devices are accompanied by non-negligible ohmic loss. In contrast, photonic are made of lossless dielectrics, but necessarily have dimensions on the order of a few wavelengths, since at least several lattice periods are needed to achieve the collective band structure and PBG.

We have examined and compared dielectric and metallic cavities with respect to their abilities to provide lasing with efficient light generation and extraction at room temperature. To understand these differences, we use numerical finite-difference time domain calculations as well as experimental results, and use figure of merits such as the Purcell factors, laser threshold gain, and photon confinement to design the cavities. Of course, the alignment, both spectrally and spatially, of the emitter with the resonant mode of the cavity and the accuracy of the microfabrication contribute to losses within realistic devices, and these could only be evaluated experimentally.

Room-Temperature CW lasing within Ultrasmall Optical Cavities

Theoretical investigations establish that the effect of spontaneous emission modification is more pronounced in a cavity with high $Q=V$ [11] and that the control of spontaneous emission coupling to a cavity's optical modes could lead us to build high modulation rate light sources [91], low noise [92] and thresholdless [93, 94] laser, and single-photon source [95]. At the time this work began, researchers had long recognized the potential of photonic crystals as a way to design high $Q=V$ laser cavities. VCSELs and the related micropillars are essentially 1D photonic crystal lasers with strong light confinement [7, 8]. The first 2D slab photonic crystal laser with a V_{eff} about the volume of a half cubic wavelength was reported by Painter and colleagues in [90] with Q of 250 and pulsed lasing at a temperature of 143 K. Since then, many more optically pumped photonic crystal lasers have been reported and studied, however, mostly with pulsed operation at room temperature due to device thermal resistance as high as 10^5 - 10^6 K/W, where material gain saturates and nonradiative processes overwhelm before the device can go into stimulated emission [17, 90, 96]. At the same time, the photonic crystal community learnt to design extremely high Q/V cavities $Q > 10^6$ in nanobeam photonic crystal cavities [58]. To alleviate thermal resistance, many proposed or tried bonding photonic crystal membranes to a thermally conductive substrate such as the lower index aluminum oxide [97, 98] or DBR mirrors [99] with varying degrees of success; however, most low-index materials are electrically insulating, complicating potential designs to build current-injection photonic crystal lasers. Another solution is to reduce the lasing threshold by increasing Q or decreasing the transparency carrier density N_{tr} required for lasing [19, 86].

Our goal in this program was to build a room temperature, CW microlaser within a volume smaller than a cubic wavelength. In the subsequent sections, we present the device design progress made in this work. We begin by studying the possibility of using metal to improve disk lasers' cavity Q , V_{eff} , and emission directionality [27]. We then investigated the merit of using metal in conjunction with photonic crystal nanocavity to serve as both a thermal and electrical conduction path, which helps achieve room temperature CW lasing by current injection [32]. In looking at the confinement mechanisms of photonic crystal cavity on metal, we found that optical confinement can be obtained in optically thick photonic crystal slab with $Q > 1000$ while keeping V_{eff} below a cubic wavelength. We show this structure is feasible to lase [101] and that the thicker slab gives us more space to properly design a vertical p-i-n stack, where gain is in the intrinsic region, for current-injection operation. Following that, we turn our attention back to photonic crystal cavities in optically thin slabs and evaluate ways to improve the far-field emission directionality using coupled-cavity designs [102]. Lastly, we pushed the limit of optical confinement in semiconductor dielectrics with the nanobeam photonic crystal designs. We expect their small V_{eff} will result in a high F_p laser with a soft threshold transition, and their small cross-sectional area will reduce the effect of feedback from surrounding structures, compared with 2-D photonic crystal cavities [87].

3.1 Metal-clad disk laser

Metal-optic and plasmonic cavities have in recent years been of particular interest. It is well known that metals present considerable optical loss that worsens as wavelength decreases from NIR to visible. As a result, most subwavelength metallic cavities have room temperature Q factors of below 100, and thus can only lase in cryogenic temperatures with III-V semiconductor as the gain material [20, 107, 108]. Mizrahi, Nezhad, Fainman, and colleagues have proposed and demonstrated higher Q metallic cavities by inserting a low-index silicon dioxide SiO_2 layer around the semiconductor gain material. This layer is thick enough to push the optical mode away from the metal [109, 110]. However, this complicates the realization of an electrically pumped lasers based on the same design and precludes the use of metal as an effective heat sink, a feature that is proving to be important for small volume semiconductor lasers [96, 111]. In this section, we present a design of surface-emitting, subwavelength metal-clad disk laser cavities that have a room temperature Q -factor of 200 to 300 at the visible red wavelength of $\lambda \sim 670$ nm. Non-degenerate single-mode operation can be achieved by shrinking device size, retaining only the TE_{011} mode, and thereby increasing the spontaneous emission coupling factor. The laser cavity's Q and extraction efficiencies can be tuned by placing a reflector directly under the device's bottom surface. The TE_{011} mode can have a Q of 230 and a V_{eff} of $0.46(\lambda/n)^3$ with a 400×400 nm² footprint. Far-field radiation pattern and emission directionality were also evaluated.

Laser cavity design

Dielectric disk laser cavities have Q -factors limited by radiation loss in the horizontal direction, which imposes a lower limit of $d_0 \sim 0.7 - 0.8 \lambda$ on device size [112, 113, 114], where d_0 is the dielectric disk diameter. We consider specifically, as an example, a disk laser cavity designed for the more localized transverse electric-like TE_{mpq} modes (m , p , and q are the azimuthal, radial, and axial mode numbers, respectively) at $\lambda = 670$ nm. It has a thickness of $T = 210$ nm and a dielectric constant of $\epsilon_d = 11$, corresponding to the commonly used red laser material AlGaInP [115]. The cavity Q falls sharply as the disk diameter shrinks, and a resonant mode with $m < 3$ can hardly exist.

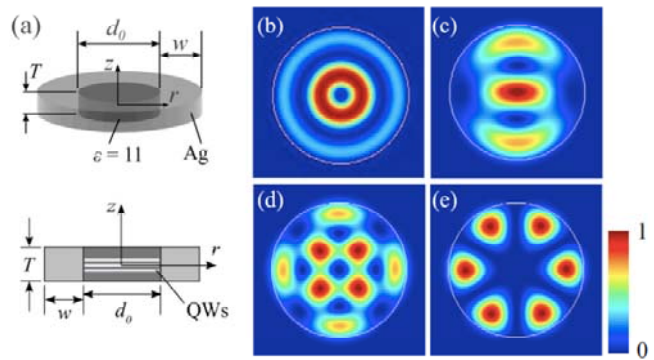


Figure 2 (a) 3D schematic and side view cross-section of the silver-clad disk cavity, the origin of the coordinate system is located at the center of the dielectric disk; (b)-(e) Electric-field intensity distribution $|E|^2$ of resonant modes in a $d_0 = 420$ nm cavity, $m = 0$ (TE_{021} , $\lambda = 642$ nm, $Q = 240$), $m = 1$ (TE_{122} , $\lambda = 660$ nm, $Q = 160$), $m = 2$ (TE_{221} , $\lambda = 676$ nm, $Q = 230$), and $m = 3$ (TE_{311} , $\lambda = 675$ nm, $Q = 290$), respectively.

To curb radiation loss, we clad the semiconductor disk's curved surface in an optically thick, reflective, and low loss metal layer, shown schematically in Figure 3.2(a). We choose to use silver, because it is a relatively low loss metal in the visible spectrum. Its dispersive dielectric function can be described by fitting experimental data to the Drude-Sommerfeld model [28, 103, 116]. The skin depth of silver at this wavelength is about 25 nm, so a metal thickness of 100 nm in the radial direction is sufficient. We use a high resolution of 2 nm in the FDTD simulations to capture the rapid attenuation of electromagnetic fields in metal. A sub-wavelength sized device with $d_0 = 420$ nm forms a multimode resonator and, due to the effective radiation loss inhibition by the silver cladding, supports the lowest order $m = 0; 1; 2; 3$ modes with Q-factors of 160 to 290. The non-degenerate $m = 0$ mode has a Q of 240. Normalized mode profiles are shown in Figure 2(b)(e). To obtain non-degenerate single-mode operation, the device needs to be shrunk to $d_0 = 220$ nm, where only the TE_{011} mode is supported with a Q of 210; its mode profile is shown in Figure 3 (a)(b). We note that the presence of silver cladding enables the co-existence of a 670 nm SPP resonant mode, distinguished by its electric field maximum at the silver-dielectric interface, as shown in Figure 3 (c)(d); however, it has a material absorption limited low Q of about 50, since a large fraction of the electromagnetic field exists in the metal cladding and suffers much ohmic loss.

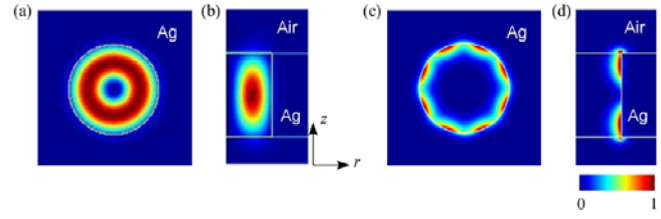
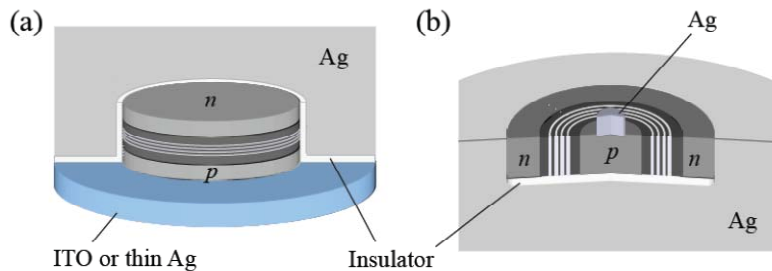


Figure 3. Electric field intensity distribution of modes in a $d=220$ nm cavity at 625nm.

	$d_0 = 220$ nm		$d_0 = 420$ nm			
	$m = 0$	SPP mode	$m = 0$	$m = 1$	$m = 2$	$m = 3$
Q_{tot}	210	54	240	160	230	290
λ [nm]	663	664	642	660	676	675
$V_{eff} [(\lambda/n)^3]$	0.46	0.23	0.71	0.80	1.27	1.36
F_p	35	18	26	15	14	16
η_{rad}	0.16	0.00017	0.47	0.72	0.39	0.33
Γ_E (7 QWs)	0.34	0.14	0.32	0.17	0.34	0.14
g_{th} [cm^{-1}]	5922	53837	5607	16016	5348	10409
Γ_E (9 QWs)	0.39	0.24	0.38	0.27	0.39	0.21
g_{th} [cm^{-1}]	5085	31896	4833	9810	4644	6831

With 7 QWs, the non-plasmonic modes g_{th} ranges between 5348 and 16016 cm^{-1} ; with 9 QWs, it is between 4644-9810 cm^{-1} . These threshold gain values are still not quite achievable in GaInP/AlGaInP

at room temperature [74, 118]. Therefore, still higher Qs are needed to bring down g_{th} and make room-temperature operation feasible. There are two loss channels for the metal-clad disk cavity: radiation loss into free-space and absorption loss mostly due to the metal. By separating out the Q_{rad} and Q_{abs} components, it is apparent that Q_{tot} is limited by material absorption. For the TE_{011} mode, for example, Q_{rad} is >1000 , while Q_{abs} is around 250 and dominates. Indeed for most metallic cavities at optical wavelengths, the material absorption limited room temperature Q is seldom greater than 100 and lasing only occurs at cryogenic temperatures [20, 107, 119]. That is why a low-index dielectric needs to be inserted between the semiconductor disk and the metal cladding to curb metallic absorption and to provide electrical insulation where needed.



Radiation characteristics

A metal-clad disk laser such as one shown in Figure 2(a) radiates through both its top and bottom surfaces. It is difficult to collect light in both directions; half of the radiated light would be lost. We can thus think of placing a reflector under the disk

to redirect the downward traveling light, as has been proposed for microcavity LEDs [121, 122] and photonic crystal resonators [51]. In Figure 4, two current-injection schemes for metal-clad disk laser design the sub-wavelength size and mode volume and to be able to place the reactor arbitrarily close to the resonator's bottom surface, we use an optically thick silver layer instead of Bragg reflectors. A silicon dioxide SiO_2 spacer of thickness h is used to tune the radiation characteristics. Other low index materials can also be used for better thermal conductivity, such as silicon nitride or aluminum oxide. The device structure is shown in Figure 5(a). To illustrate the effect of the bottom reactor, we study the non-degenerate TE_{011} mode (see Figure 3). The electric field has its maximum located at $z = 0$ and decays to small magnitude at the $d = 11$ dielectric disk's top and bottom surfaces. Silver has a large negative real dielectric constant 670 nm [28, 103].

Therefore, the bottom reactor results in little change in the resonant mode profile, even when it is in contact with the disk resonator, as shown in Figure 3.5(b). Although we are mostly interested in room temperature operation for laser applications, it is nevertheless instructive to look at the effect of the bottom reflector at lower temperatures. The low temperature metallic dielectric function can be estimated using the resistivity versus temperature data of silver [123]. The damping frequency is proportional to material resistivity, and is 18% of its room temperature value at $T = 80$ K. Loss due to metallic absorption does not change much, regardless of the presence of the bottom silver reactor or its position. Q_{abs} is consistently about 250 at room temperature and 1400 at 80 K. The increase in Q_{abs} with respect to temperature is as expected, due to the corresponding decrease in resistivity and thus ohmic loss in silver. On the other hand, Q_{rad} are strongly modulated by the bottom reactor. By varying the spacer thickness h , Q_{rad} changes between 225 and 2710, and thereby enhances or deteriorates Q_{tot} . When $h < 150$ nm, Q_{rad} is enhanced with no additional material absorption loss, consequently at room temperature Q_{tot} is increased to 230, from $Q_{\text{tot}} = 150$ for a laser cavity on SiO_2 substrate or $Q_{\text{tot}} = 210$ for one suspended in air with no bottom reflector. When $h \sim 250$ nm, however, Q_{rad} is at a minimum and Q_{tot} deteriorates to 120. The TE_{011} mode from a $d_0 = 220$ nm cavity exhibits a mostly -polarized far-field radiation with negligible polarization, which is analogous to the far-field pattern of the

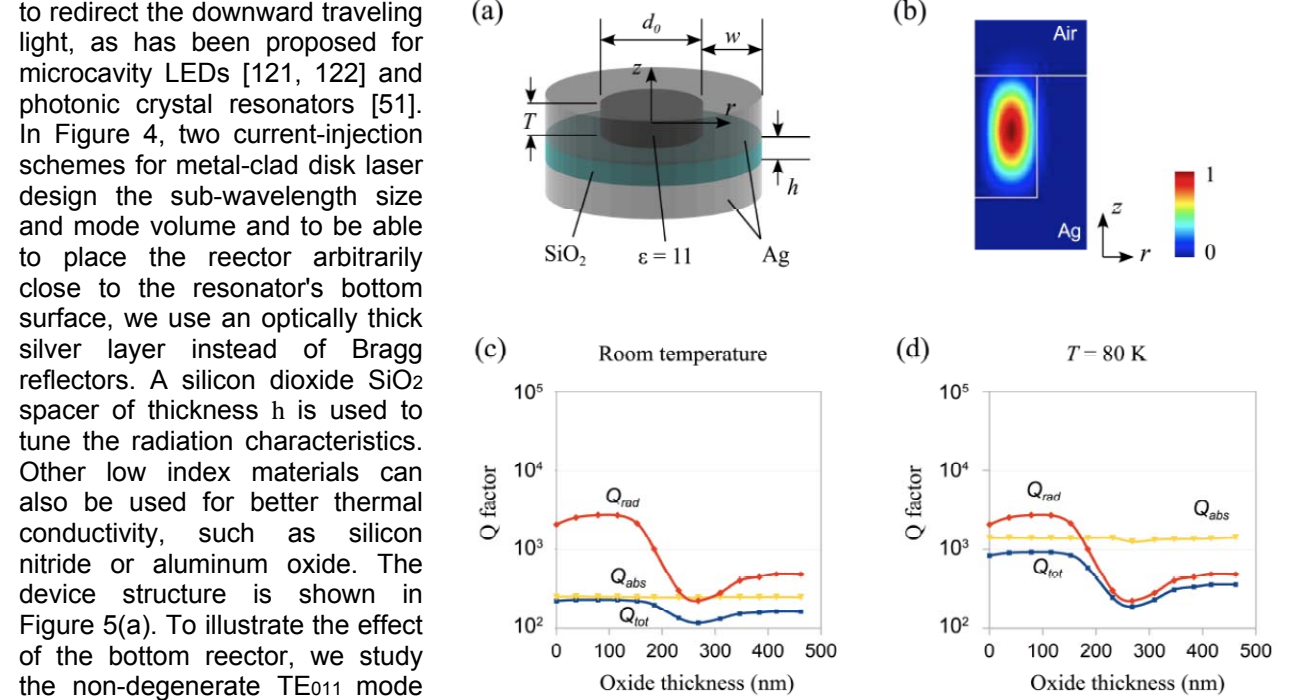
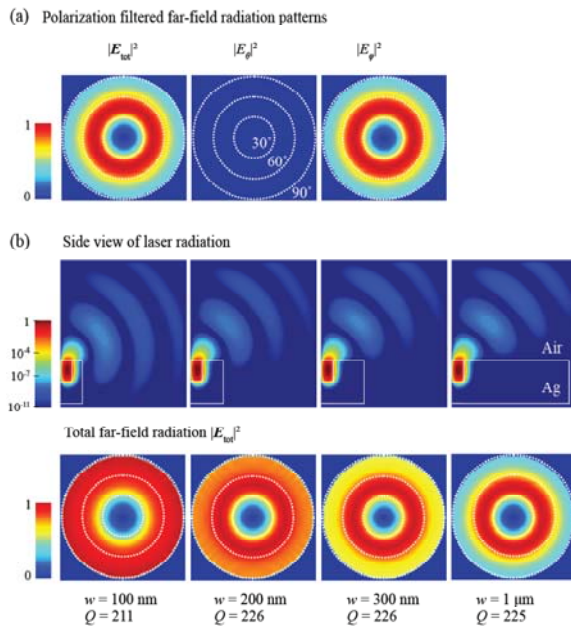


Figure 5: Q_{tot} , Q_{abs} , and Q_{rad} of metal-clad disk resonators with a bottom reflector. We proceed to study the far-field radiation pattern of the surface-emitting metal-clad disk laser. Normalized far-field intensities are plotted in Figure 3.6(b) and (c) with the laser surface normal at the center, and 30, 60, and 90 from surface normal are indicated with dotted white circles.



monopole mode in a single-defect photonic crystal cavity [51]. The radiation is directed upward, with the field intensity maximum at about 45° from surface normal, as shown in Figure 6(b). We find that the far-field pattern remains unchanged with or without the bottom rector and as we vary the spacer thickness h . As we reduce w , however, the radiated light interacts with the laser cavity's surroundings; the far-field pattern is strongly affected. Take the example of the TE_{011} mode with a bottom rector and $h = 0$, where the only light emission is through the laser cavity's top surface. Varying w from 1000 to 100 nm, the resonator retains its resonant wavelength of 660.2 nm and a Q_{tot} of 210 to 225. The far-field radiation remains λ -polarized, but its field intensity distribution changes from having a distinct maximum at 45° to spreading in the horizontal direction between 60° and 90° ; the device changes from a surface-emitting laser to a horizontal emitter with poorer directionality, as is evident in Figure 6(c). Thus, in designing sub-wavelength lasers, one needs to be aware of the influence on the directionality of the emitted light by structures surrounding the laser cavity. While a metal cladding thickness of several times the metal's skin depth is sufficient to suppress radiation loss and create a laser resonator, it may need to be of wavelength scale to obtain light emission in the desired direction.

2 Photonic crystal cavity bonded on metal

Photonic crystal defect cavity lasers are a relatively new design. The research field has so far been occupied with progress toward achieving stable lasing at room temperature with hope of demonstrating signatures of Purcell effect [6, 19, 124]. Much progress was made in fine-tuning the cavity geometry for high Q -V [49, 50, 52, 56, 125] and improving fabrication techniques [96, 126, 127, 128]. Interestingly, the basic device structure has not changed since the first 2D photonic crystal laser [15, 90] a regular array of air-holes are drilled into a suspended III-V semiconductor membrane to form the 2D photonic crystal, a

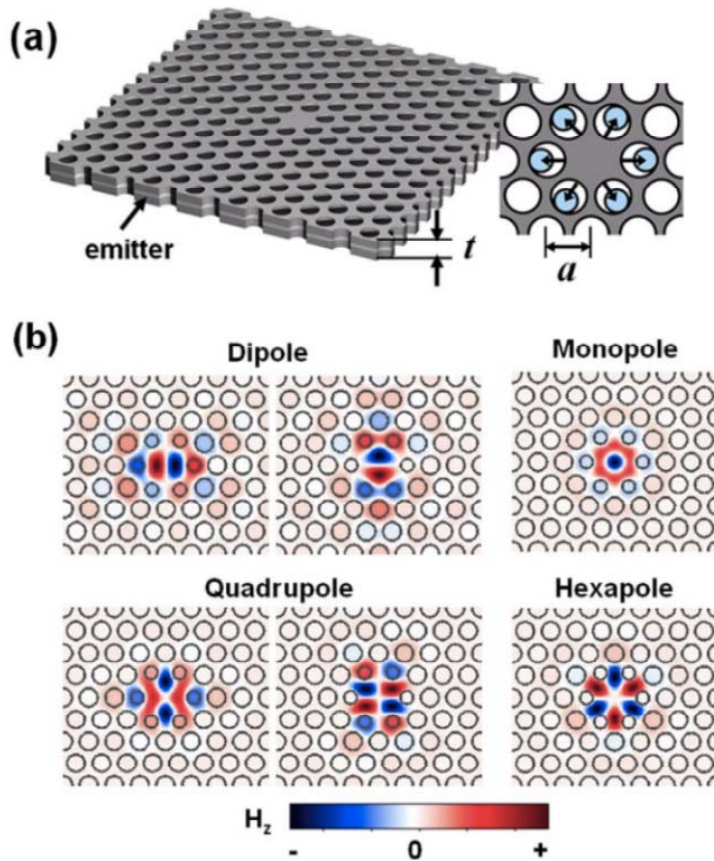


Figure 7: Electric field profile for monopole, dipole, quadrupole, and hexapole modes of a modified single defect photonic crystal cavity.

single defect or several adjacent defects where there is no air-hole form the cavity. In most cases, the membrane is suspended less than one free-space wavelength above the substrate. Research on now-established forms of lasers, including Fabry-Perot-type semiconductor diode lasers, have shown that feedback from a laser's output signal can significantly alter the device's linewidth and other noise characteristics; even 0.5% is considered a large feedback [71]. For photonic crystal lasers, Kim and colleagues [51] investigated the effect of the bottom substrate on a single-defect cavity's emission characteristics, calling to attention both the tunability of emission directionality and the effect of feedback from structures surrounding the suspended photonic crystal membrane.

We build upon this investigation using the single-defect cavity, whose structure and resonant mode profiles are reproduced in Figure 7. The dipole and hexapole modes are studied in particular, for they are able

to achieve vertical light emission with a small divergence angle, unlike the monopole and quadrupole modes.

Effects of feedback from the substrate

Let h be the air-gap size between the photonic crystal membrane and the underlying substrate; the device structure is shown in Figure 10(a). The background air-holes have radii of $R = 0.35a$. The air-holes nearest to the defect cavity are shrunk to $R_m = 0.25a$. Then to break the six-fold symmetry, two opposite air-holes are enlarged by $R_p = 0.05a$. We present an example of the effect of substrate feedback using the modified hexapole mode shown in Figure 3.10 [32]. h is varied between $0.5a$ and $5a$; $\lambda = 1.3 \mu\text{m} = 0.29a$. Three types of substrate are used in the simulations: perfect electric conductor (PEC), InP dielectric constant, and dielectric function of gold at room temperature fitted to the Drude-Sommerfeld model. Gold is used, because it is one of the least lossy metals. 3D FDTD simulations show that cavity Q and far-field radiation pattern vary as a function of h with a periodicity of 0.5λ . For example, Q reaches its minimum at $1.75a$ and $3.5a$, corresponding to 0.5λ . This periodic behavior maintains the same trend regardless of substrate material, though the effect is most pronounced with a PEC, weakest with a dielectric, and medium with a room temperature metal substrate, due to difference in the materials' reactivity.² The 0.5λ periodicity calls to mind the analogy of a dipole emitter in a planar Fabry-Perot cavity that can be modeled using plane wave interference [122, 129]. Using the model and validated by FDTD simulations, enhanced vertical emission due to constructive plane wave interference occurs. [51].

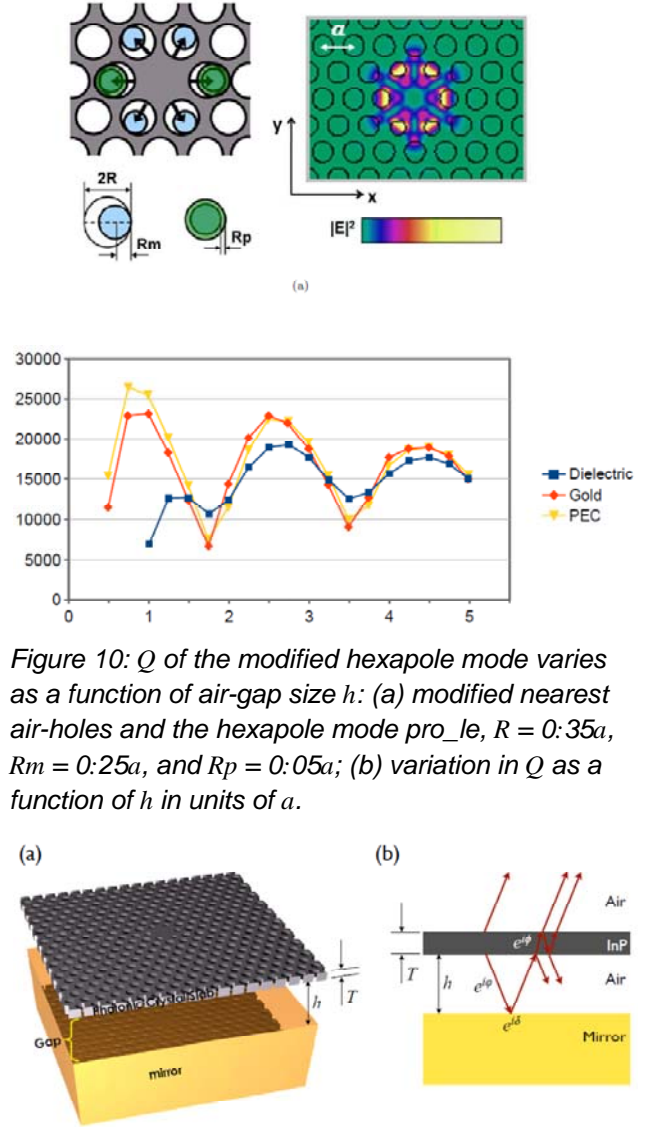


Figure 10: Q of the modified hexapole mode varies as a function of air-gap size h : (a) modified nearest air-holes and the hexapole mode profile, $R = 0.35a$, $R_m = 0.25a$, and $R_p = 0.05a$; (b) variation in Q as a function of h in units of a .

Cavity characteristics of photonic crystal on a metal substrate

In the previous section, we concerned with the case where the air-gap between the photonic crystal slab and the substrate is large enough, approximately $h > a$, such that the photon confinement mechanism of PBG is still effective. As h approaches 0, however, this is no longer the case. When the photonic crystal slab rests directly against a dielectric substrate such as InP, there is no more confinement, light leaks into the substrate. When the slab is bonded to a PEC or gold, a weaker confinement remains. For a slab thickness of $T = 0.9a$, $Q > 1000$ in the case of PEC, and is but a few hundred for gold. Such a low Q is insufficient for building room temperature CW lasers. That is unfortunate, as metals have very good thermal and electrical conductivity, a characteristic that would have been useful to relieve microlasers' huge thermal resistance and to make electrical contact for current-injection operation. Metal substrates also do not support downward propagating optical mode as do dielectric substrates, so the device only emits light through its top surface, showing promise of increased collection efficiency. Moreover, when the photonic crystal slab rests directly on the reactive metal, we eliminate a source of external feedback to

the microlaser, potentially simplifying device design and analysis. We have attempted to increase Q of this photonic crystal bonded on metal structure to a level at which room temperature CW lasing may be possible, and study its optical confinement mechanisms. Once a satisfactory Q is achieved, we tune the design parameters to obtain directional emission with very good linear polarization. The device schematic is given in Figure 12(a). We investigate, particularly, the modified dipole mode, whose mode profile is shown in Figure 12(b). We postulate two main channels of optical loss, which we need to mitigate in order to raise Q . First, metal absorption loss with an optically-thin slab, we would expect a significant electromagnetic field overlap with the gold substrate, leading to appreciable material absorption in room temperature gold. Second, a photonic crystal bonded on metal has a diminished PBG, if it has a PBG at all, thus in-plane confinement is compromised. One way to decrease modal overlap with the gold substrate is to simply increase the photonic crystal slab thickness T . Figures 13(a)-(b) show the 3D FDTD simulation results of effective mode. Interestingly, Q increases steadily as well. $Q > 600$ when $T > 2a$ (600 nm), and $Q > 3000$ when $T > 5a$ (1500 nm). What's more, Q seems to increase indefinitely with increasing T . On the other hand, unsurprisingly, V_{eff} increases monotonically though not drastically. F_p as a function of increasing T , calculated using our models and shown in Figure 13(c)-(d); (d) is calculated using emitter properties of the widely used InGaAsP QWs. Though $T = 450$ nm, there is still an appreciable TE-like bandgap when the slab is suspended in air. When it is on a metal or PEC substrate, however, there is no more bandgap.

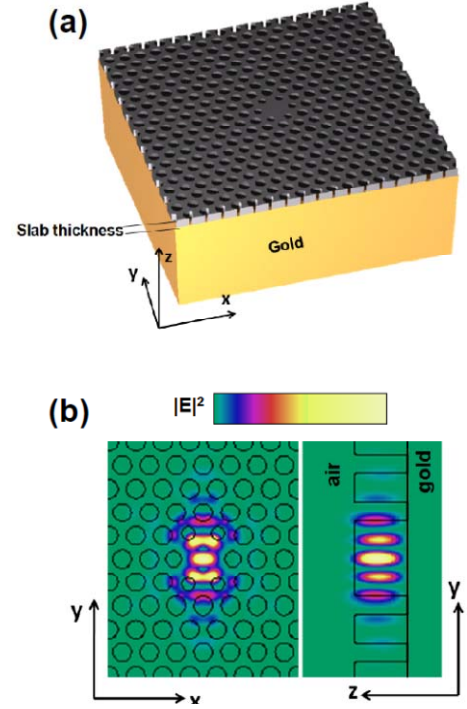


Figure 12: Modified single-defect cavity on gold substrate: (a) schematic of device structure; (b) mode profile of the modified dipole mode volume V_{eff}

Figure 14 shows the dispersion diagrams and mode profiles of the different metal/dielectric slab geometries investigated. We note that Figure 14(a), (b), and (d) look awfully similar to each other, with (b) and (d) being almost identical. This phenomenon is not surprising when we think about our metallo-

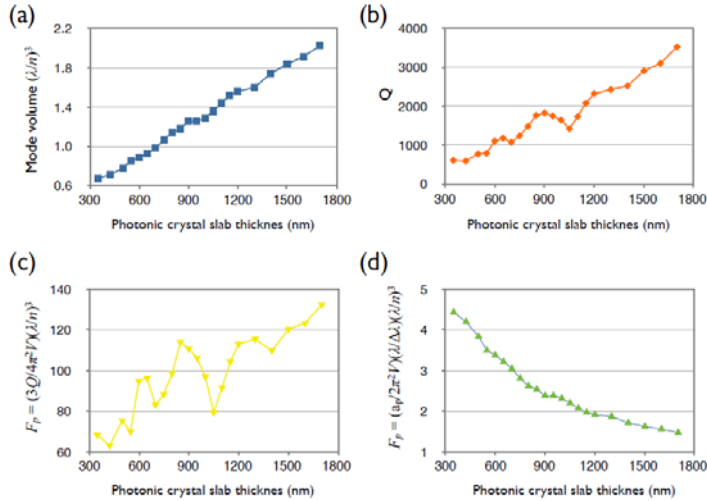


Figure 13: Modified dipole mode characteristics of photonic crystal slab bonded on gold, as functions of slab thickness T : (a) effective mode volume (b) cavity Q ; (c) Purcell factor F_p (d) Purcell factor F_p

photonic crystal using the method of images [1]. TE-like modes in a photonic crystal with slab thickness T on PEC is equivalent to TM-like modes in one with thickness $2T$. Indeed, if we apply the same method to the mode profiles, bands 1, 5, 6, and 7 in Figure 14(e) are but modes with an antinode mid-slab in the photonic crystal of thickness $2T$, whereas bands 2, 3, 4, and 8 have a node mid-slab. We can thus analyze many of the cavity characteristics, such as optical confinement mechanism for the metallo-photonic crystal, as we would a air-suspended thick-slab device with twice the dielectric thickness. This very much simplifies numerical simulations: the metal substrate presents a rapid evanescent field decay inside it, requiring fine resolution of $1/2$ nm, and it breaks the symmetry in the z -direction, further increasing computation memory and time

requirements; in contrast, an air-suspended dielectric thick-slab can be simulated using coarser resolution of 10-20 nm pixel size and also enables us to use odd or even symmetry in z .

With no in-plane PBG modes, the optical confinement in our thick-slab photonic crystal can be understood based on dispersion along the z -direction. Instead of the band diagrams we are used to for conventional photonic crystal slabs, we look at the dispersion relations. The fact that we can achieve Qs of a couple of thousand is very encouraging for building room temperature CW current-injection lasers. In designing an electrically-pumped device based on this geometry, a thin low-index dielectric can be inserted between the photonic crystal slab and the gold substrate to further reduce mode overlap with the metal and with a small gold-filled aperture under the cavity to act as a current aperture. Furthermore, the results suggest that we do not have to adhere to optically-thin photonic crystal cavities.

We also looked at how to design for directional emission from metallophotonic crystal cavities: Using 3D FDTD and near-to far-field transformation, we tune T and see how the far-field radiation pattern changes. The results in Figure 15(a) show that this single parameter changes things drastically. When $T = 600$ nm, emission is concentrated within a 15° cone, yet $T = 700$ nm results in a divergent emission where field intensity is evenly distributed within a 60° angle. At the optimum $T = 600$ nm, the radiation is also mostly linearly polarized in the x -direction, as shown in Figure 15(b), promising

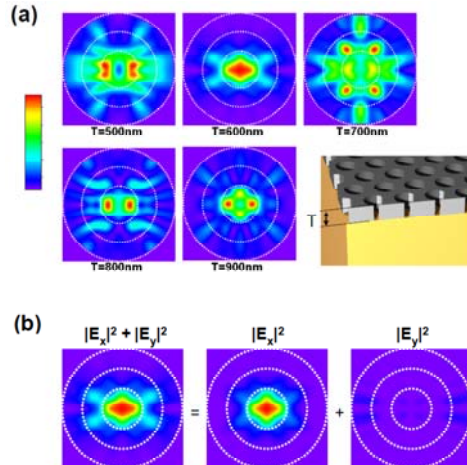


Figure 15: Far-field radiation pattern of the modified dipole mode on a gold substrate: (a) far-field pattern modulation due to changes in T ; (b) linear polarization decomposition of far-field radiation from a $T = 600$ nm slab.

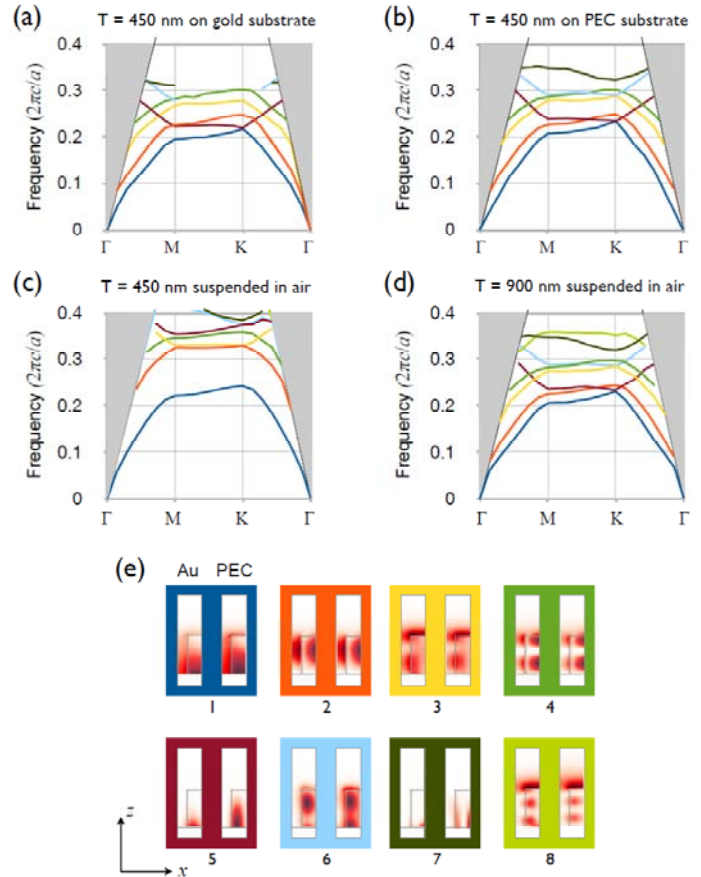


Figure 14: Band structures (dispersion relations) of $T = 450$ nm and $T = 900$ nm triangular lattice photonic crystal: (a) TE modes in $T = 450$ nm slab on room temperature gold substrate; (b) TE modes in $T = 450$ nm slab on PEC substrate; (c) TE modes in $T = 450$ nm slab suspended in air; (d) TM modes $T = 900$ nm slab suspended in air; (e) jE_jz mode profile of the different bands in (a) and (b), left panels are for gold substrate, right panels are for PEC substrate, panel colors correspond to color code in the band structure diagrams.

easy coupling into optical fibers or waveguides.

Thick-slab photonic crystal lasers

Our investigation into photonic crystal bonded on metal substrate shows that an in-plane bandgap is not necessary to achieve high enough Q cavities for lasing. This prompted us to look into the possibility of lasing in optically-thick single-defect cavities

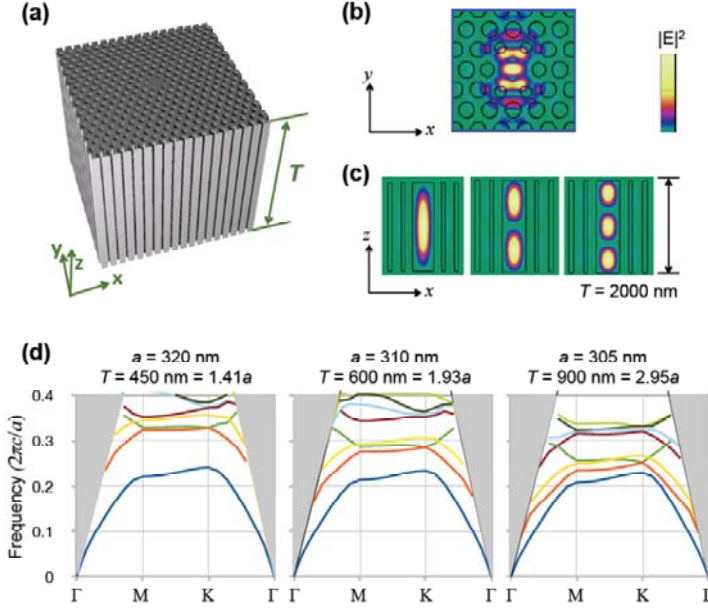


Figure 16: Modified dipole mode in optically-thick single-defect photonic crystal cavity: (a) schematic of device structure; (b) fundamental $|E_z|^2$ mode profile in x - y plane; (c) $|E_z|^2$ mode profile for fundamental, first, and second order modes when $T = 2000$ nm, in x - z plane; (d) band structures with increasing slab thickness from $T = 1.4a$ to $T = 3a$.

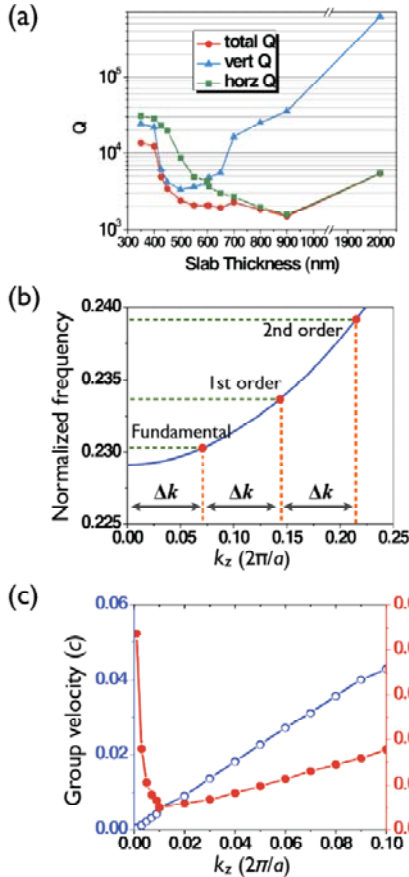


Figure 17: Analysis of optical confinement mechanisms in the modified dipole mode: (a) Q as a function of T and its decomposition into Q and Q_k ; (b) dispersion relation with the fundamental, first order and second order modes labeled; (c) group velocity v_g and normalized waveguide loss coefficient as functions of k_z . mirror facets

optical confinement mechanisms at work that were not previously considered in optically-thin slabs.

To gain some insight, we decompose Q_{tot} into Q_v and Q_k , where the former measures loss in the vertical direction and the latter quantifies loss in-plane in the photonic crystal slab, and plot the result as a function of T in Figure 17(b). When the slab is optically-thin, Q_v depends very much on the particulars of cavity design, such as R_m and R_p parameters [52], and is in the range of 10^4 for $T < 400$ nm, in agreement with other published results [51]. It drops to a few thousand when $T = 1.5a - 2a$, then shoots up to a surprising value of 6

[101]. Thicker slabs have the advantage of lower thermal resistance and allow us more room and freedom in designing the device's vertical p-i-n doping profile for better electrical properties. In fact, concurrent with our work, Tandaechanurat and colleagues studied the same problem, and demonstrated CW lasing at a cryogenic temperature of 4 K in a thick-slab cavity with $T = 1.1a - 1.6a$ [132]. Consider the modified dipole mode in an air-suspended single-defect photonic crystal cavity with a large thickness T , shown in Figure 16(a). The cavity design is the same as that shown in Figure 10(a), where $R = 0.35a$, $R_m = 0.25a$, and $R_p = 0.05$. First, let us look at the TE-like band structures of the background photonic crystal in Figure 16(d).⁴ At $T = 1.4a$, the second guided band begins to droop down to lower frequencies in the Γ -M and Γ -K directions, decreasing bandgap. When $T > 2a$, the band gap disappears, a resonant mode at any frequency would overlap with at least one guided band. The band structure for $T = 3a$ is just a tangle. Lack of PBG notwithstanding, FDTD simulations show that we still have well-defined resonant modes in the cavity that have the same transverse mode profile but different numbers of intensity lobes in the z -direction, as shown in Figure 16(b)(c). The three modes are closely spaced spectrally. When $T = 2000$ nm, for example, resonant wavelength is $\lambda = 1324, 1305$, and 1275 nm, $Q = 5390, 1580$, and 750 , and $V_{\text{eff}} = 2.45, 2.65$, and 2.86 $(\lambda/n)^3$ for the fundamental, first order, and second order modes, respectively. Moreover, Q of the fundamental dipole mode ranges between 1000 and 6000 for $T = 2a$ to $6a$ (see Figure 17(a)), indicating effective

10⁵ at $T = 2000$ nm. Q_k drops from 10⁴ to several thousand as PBG disappears and seems to remain in that range. This contrast in Q and Q_k prompts one to think of vertical confinement no longer as total internal reflection in a very thin 2D slab wavelength [15] but perhaps as a vertical Fabry-Perot in a short photonic crystal fiber. At the same time, the in-plane confinement can be understood to be due to mode mismatch between the cavity mode and guided mode(s) in momentum space, allowing only weak coupling

between the two [132]. Consider a device with a very large T , which resembles a photonic crystal fiber. In the absence of both TE- and TM-like PBG in the transverse direction, our dipole mode is analogous to the index-guided modes in a fiber with a dielectric core, confined by the index contrast between the defect region and the holey photonic crystal background [66] and in contrast to the bandgap guided Bragg fibers usually with a hollow core [40]. We can then define a k_z and plot the waveguide dispersion in the z -direction, shown in Figure 17(b). We have also labeled the intersection of the fundamental, first order, and second order mode frequencies on the dispersion curve. These intersections appear to be evenly spaced in k_z , confirming a satisfied Fabry-Perot condition [23]:

Transverse optical confinement by index contrast is a plausible explanation, but it does not explicitly address the potential coupling between the resonant mode and the propagating modes guided by the photonic crystal slab as we see in the band diagrams (Figure 16(d)). We postulate that there is little coupling between the resonant mode and the guided modes due to momentum mismatch. To confirm, the modified dipole mode's E-field intensity distribution jE_jz in momentum space is calculated using 3D FDTD for several slab thicknesses $T = 1.40a$; $1.94a$; $2.95a$, as shown in Figure 18. The light cone is indicated by the white circles. The equifrequency lines for the guided modes at the resonance frequency are drawn in grey lines by interpolating their locations in the Γ -M and Γ -K directions. The majority of the resonant mode resides far from the light cone, and the guided modes do not intercept areas of high intensity. Thus moderate Q s can be achieved despite the lack of a PBG in optically-thick photonic crystal slabs.

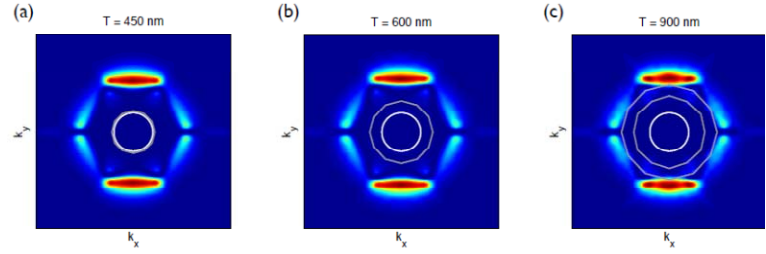


Figure 18: E-field intensity jE_jz distribution in momentum space. $T = 450$ nm (1:40a), 600 nm (1:94a), and 900 nm (2:95a). White circle indicate the light cone. Grey lines are the locations of the guided modes at the resonant frequency, based on the equifrequency contours' intercepts with the Γ -M and Γ -K vectors.

Coupled-cavities for enhanced far-field emission directionality

Coupled-cavity photonic crystal lasers have been studied to increase lasing power and differential quantum efficiency [133]. Single mode operation can be achieved from coupled cavities even when they are individually multimode, as the constituent cavities act as mode filters for each other [134]. At the same time, most of the wavelength-scale laser cavities are so far optimized for high Q and small V_{eff} in attempt to maximize F_p , but are not particularly designed for efficient light extraction. Extraction methods such as evanescent coupling to a tapered microfiber [83] and monolithic integration with a passive waveguide using wafer regrowth techniques [135] have been demonstrated; lasers with highly directional surface emission can provide an alternative way to achieve efficient free-space light coupling [51]. To further investigate and improve on these issues, we have designed coupled photonic crystal cavities that exhibit single mode lasing and enhanced emission directionality. Our devices are formed in an InP slab with a thickness T of 240 nm on top of a 1.16 μ m thick sacrificial InGaAs layer. Cylindrical holes etched into the slab in a hexagonal lattice form the photonic crystal. One missing air hole forms a simple H1 cavity; 3 or 5 missing air holes along the Γ -K direction form an L3 or L5 cavity, respectively. We laterally couple these cavities as shown in Figure 3.19: Design A consists of L3-L5-L3 cavities, Design B consists of H1-L3-L5-L3-H1 cavities. FDTD simulations show that for both designs there are resonant modes with Q of a couple hundred within the InP/InAsP QWs' gain spectrum; however, there is one prominent mode with $Q = 1690$ for Design B, and $Q = 3110$ for Design A. Thus, we can expect single-mode lasing from these designs. Efficient free-space coupling requires the laser to have a directional far-field radiation pattern.

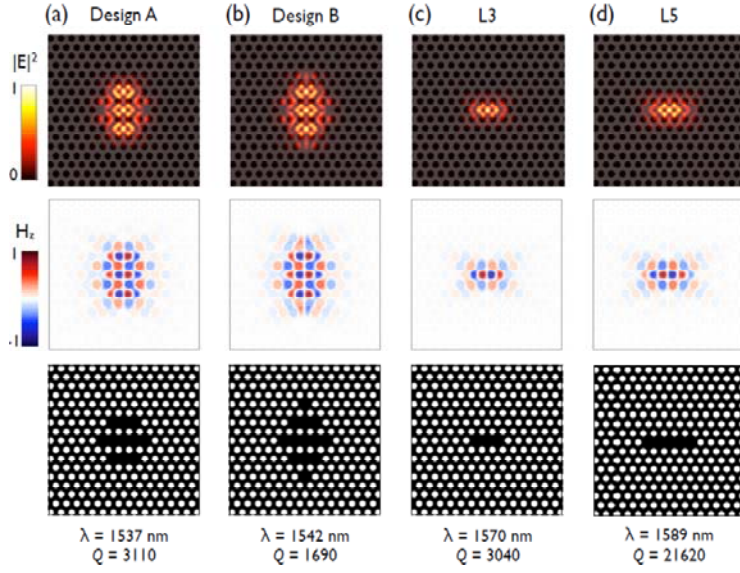


Figure 19: $|E|^2$ and H_z mode profiles and top view device schematic of coupled-cavity designs, L3 and L5 cavities are shown for comparison: (a) coupled-cavity Design A; (b) coupled-cavity Design B; (c) L3 cavity; (d) L5 cavity.

pattern is noticeably affected, making the reactivity and distance of the substrate an important design parameter. Single L3 or L5 cavities radiate light with poor directionality. Most of Design A's emission is at 60° in the x-direction, making free-space light collection difficult. Under the comparison, Design B has much enhanced emission directionality along the laser's surface normal, suggesting efficient free-space coupling. For Design B of a coupled-cavity laser suspended $1.16 \mu\text{m}$ above the InP substrate as is our case, the emitted light has a Gaussian-like dominant center peak. The center emission lobe represents $>40\%$ of the light emitted from the laser's top surface and has a FWHM beam divergence of 20° from surface normal in the x-direction and 8° in the y-direction.

Nanobeam lasers

The photonic crystal microlaser cavities we have studied so far are designed for room temperature CW lasing with potential for current-injection operation. However, their relatively large mode volume precludes strong Purcell effect in realistic QW materials. Using the expression for Purcell effect in a laser cavity,

The proposed schemes so far for directional emission from photonic crystal microcavity lasers involve fine modification of the air-holes in the vicinity of the main cavity [51, 136]. In fact, Kang and colleague have experimentally confirmed the effect of nearest air-hole tuning on the single-defect laser's far-field pattern from a hexapole mode [137]. Here, we show that far-field directionality can be engineered by proper arrangement of coupled cavities to a level that is satisfactory for practical application without fine-tuning the PhC air-holes. We calculate the coupled cavities' far-field radiation pattern using methods described by Kim et al. [51], the results are shown in Figure 3.20. While the PhC cavities' mode profile and Q hardly change with the presence of the substrate under the suspended PhC slab, the far-field

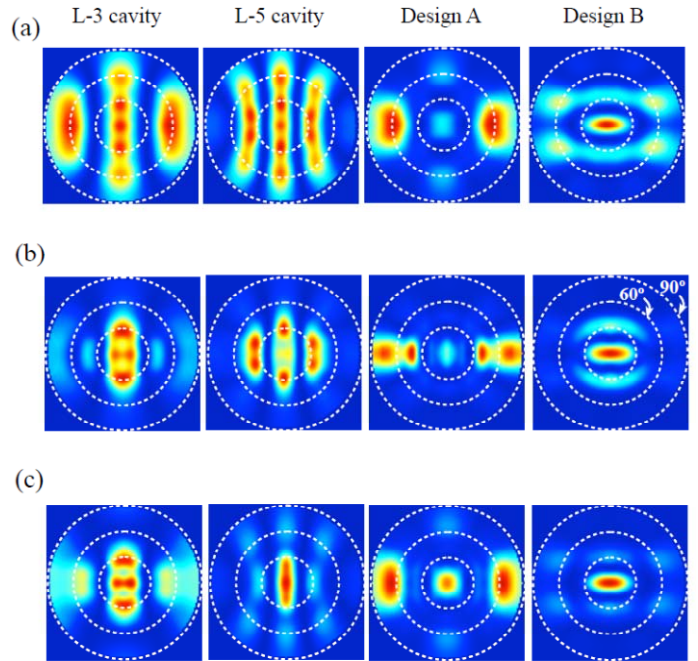


Figure 20: Simulation of far-field emission patterns single L3, L5, and coupled-cavity lasers: (a) suspended PhC slab with no substrate; (b) PhC slab suspended 1160 nm above the InP substrate; (c) PhC slab suspended 770 nm above the InP substrate. Dashed white circles indicate 30° , 60° , and 90° from surface normal.

With InGaAsP, the commonly used gain material for $\lambda = 1.3\text{--}1.55\mu\text{m}$, spectral linewidth due to homogeneous broadening is about 4.3 meV or 8.8 nm [131], wider than the linewidth of any cavity with $Q > 150$. High F_p lasers, therefore, are achieved with small V_{eff} . For example, assume $a_p = 0.4$ and $\lambda = 1.5\mu\text{m}$, $F_p > 5$ when $V_{\text{eff}} < 0.7(\lambda/n)^3$, which is roughly the mode volume of a typical L3 cavity in optically-thin slab [49]. The ultimate small mode volume cavities with $Q > 1000$ to give a reasonable g_{th} for lasing, thus plasmonic cavities are excluded are the point-shift photonic crystal cavity and chirped nanobeam photonic crystal, both with $V_{\text{eff}} \sim 0.3(\lambda/n)^3$ [50, 58]. Lasing with pronounced Purcell enhancement and thus soft threshold turn-on was demonstrated with the point-shift cavity on SQW InGaAsP [19]. We set out to demonstrate competitive lasing properties using the nanobeam photonic crystal cavities. They have the advantage of small on-chip footprint and no mode degeneracy like that present in microdisks and 2D photonic crystals with rotational symmetry. Design principles for nanobeam (sometimes also called nanowire) photonic crystal cavities have been explored since the early days of the photonic crystal field [48, 59, 142, 143, 144, 145]. Our suspended InP beam has a cross-section of thickness $T = 240\text{ nm}$ and width $W = 450\text{--}500\text{ nm}$, forming a single-mode waveguide, both to confine light within a small cross-sectional area and to control the polarization of the guided light. The periodic modulation in dielectric constant between $\epsilon = 10:1$ and $\epsilon = 1$ leads to a bandgap for quasi-TE modes at the Brillouin zone edge. When $T = 0.51a$ and $W = 1.06a$, the bandgap is 27% of the mid-gap frequency, extending from normalized frequency of 0.286 to 0.377. To create a cavity, one can simply insert a defect, i.e. a disruption in the periodicity, between two sets of waveguide DBRs. For example, by increasing the distance between the two center air-holes in Figure 21(c), the Q of this cavity can be tuned by changing the gap distance, however to a disappointing maximum value of a few hundred [48], due to the scattering loss at the interface of the defect and the DBRs analogous to the low- Q unmodified single defect cavities in 2D photonic crystal slabs. The solution to minimizing scattering loss at mirror boundaries and increasing cavity Q comes from constructing tapered air-hole gratings by fine tuning air-holes nearest to the cavity, a method that is already used in 2D photonic crystal slabs, examples include modified H1, L3, and doubleheterostructure cavities [56, 49, 52]. Several models have been proposed to explain this phenomenon, including cancellation of the multipole far-field radiation [149], Bloch-wave engineering for increasing the modal reactivity [54, 55], or momentum space tuning to minimize the resonant mode's coupling to radiative modes in the light cone [49, 150].

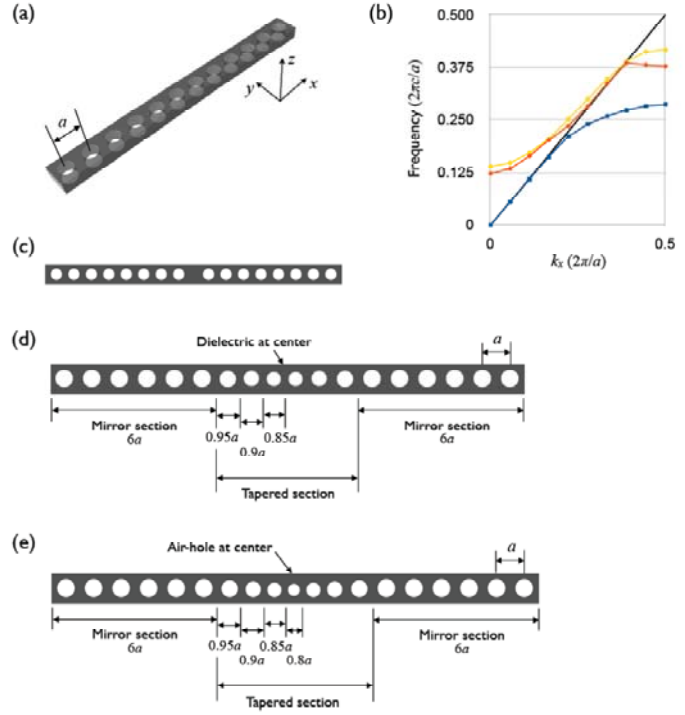


Figure 21: Waveguide DBR: (a) device schematic with the cartesian coordinates set-up; (b) band structure $!-k_x$ of the three lowest order TE-like modes, solid black line indicates the light line; (c) top view of a single defect cavity between two sets of DBRs; (d) structure of the tapered air-hole cavity with semiconductor vein in the middle; (e) structure of the tapered air-hole cavity with air-hole in the middle. $R = 0.3a$, $T = 0.5a$, $W = 1.06a$, $\lambda = 1.5\mu\text{m}$

There are many degrees of freedom in tuning the design parameters of a tapered air-hole grating. The tapering may be introduced by narrowing or widening the nanobeam width, or tapering the air-hole size without disturbing the lattice constant, or changing both the lattice constant and airhole radius. The tapering can be linear [58], quadratic [59], or parabolic [60]. We have not fully explored the large space of

parameters for tapered nanobeam photonic crystal cavity design. We chose to begin our study with linear tapering. Design parameters of the nanobeam photonic crystal cavities are shown in Figure 21(d)(e). The mirror sections each consist of six air-holes with lattice constant a and radius $R = 0.3a$. In the tapered section that forms the cavity, successive lattice constants are tapered by $0.05a$ for three periods, giving $0.95a$, $0.9a$, and $0.85a$. In the case where an air-hole is at the center of the cavity, its lattice constant is $0.8a$. Air-hole radius in the tapered region is scaled according to their respective lattice constant. A tapered air-hole cavity in the nanobeam photonic crystal geometry can have one of two symmetries—it has either a semiconductor vein in the middle of the cavity and thus supports a fundamental mode whose E_y field has even symmetry across the $x = 0$ plane, shown in Figure 22(a); or it has an air-hole at the middle and support a fundamental mode with odd E_y symmetry across $x = 0$, shown in Figure 22(b). These two designs have quite different radiation characteristics. With $0.05a$ tapering, the former design has a Q of 30,000, while the latter has a Q of 110,000. Both Q -factors are more than enough to build a laser cavity. In both cases, the E_x field component shows odd symmetry across the $y = 0$ plane and thus interferes destructively along the z -axis. The E_y field, the major E -field component for our TE-like modes, has even symmetries across $x = 0$ and $y = 0$ planes in Figure 22(a). In contrast, it has an odd symmetry across the $x = 0$ plane in Figure 22(b). Therefore, only designs with semiconductor vein at the center of the cavity, instead of an air-hole, can potentially achieve vertical emission. For laser applications, we will focus on this design.

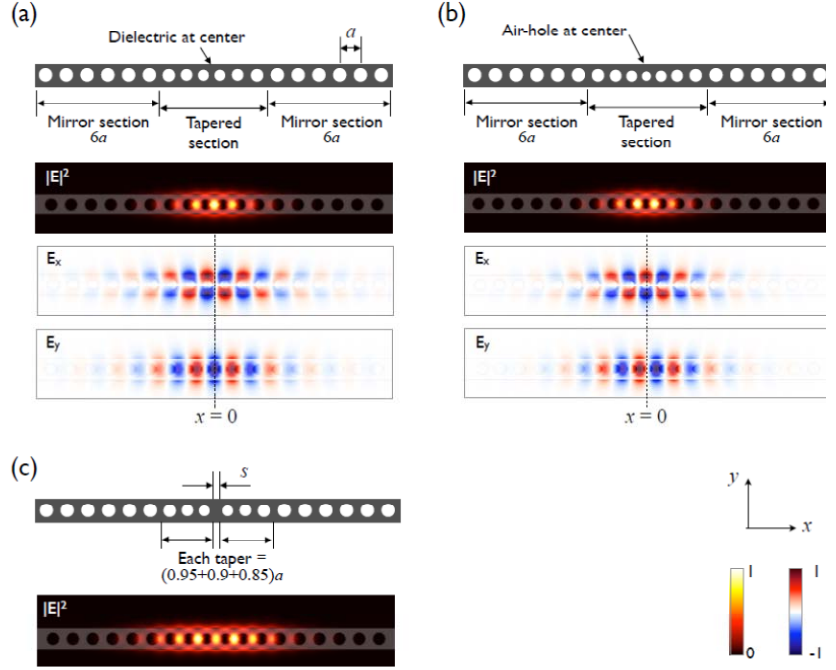


Figure 22: Waveguide DBR: (a) cavity formed by chirped air-holes in the tapered section between two sets of DBRs the mirror sections with jE_z , E_z , and E_x profiles; (b) cavity formed by chirped air-holes between DBRs, with an air-hole at the center; (c) defect of length s can be introduced in the tapered section to tune the cavity's Q and radiation characteristics. $R = 0.3a$, $T = 0.5a$, $W = 1.06a$. The vertical dotted line in (d) and (e) indicate the $z = 0$ plane.

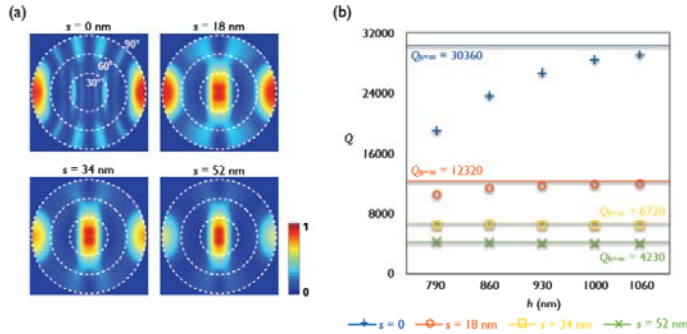


Figure 23: Radiation characteristics by tuning s and h the distance between the cavity and the underlying substrate: (a) far-field radiation patterns for different values of s ; (b) Q -factor as a function of h for cavities with different s .

We find that the insertion of an extra gap size s , see Figure 22(c), in the middle of the cavity has the most effect on enhancing vertical emission. Figure 23(a) shows the evolution of far-field radiation pattern as s increases from 0 to 52 nm; the amount of emitted power contained in the 30° cone from surface normal increases from 6.5% with $s = 0$ to 33.2% with $s = 52$ nm, where the center lobe in the radiation profile represents 56% of the total surface-emitted power with a FWHM of 30° in x and 66° in y -direction. Larger s also results in lower Q . Assuming a suspended nanobeam without other dielectric structure nearby such as a substrate, Q is 30,360 when $s = 0$, but it is

4230 when $s = 52$ nm. For laser cavities, however, this may be an advantage. Investigations by T. Baba and colleagues showed that thresholdless lasing behavior is more pronounced with lower Q of a couple thousand. In higher Q cavities, photons coupled to the lasing mode are strongly re-absorbed below the transparency condition because of the long photon lifetime. Carriers generated by re-absorbed photons may then be redistributed to non-lasing modes or non-radiative recombination, resulting in carrier loss and reduced spontaneous emission [19, 86]. Lastly, we look at the influence of substrate feedback on the far-field radiation pattern, see Figure 3.24. Surprisingly, unlike 2D photonic crystals such as the coupled-cavities in Section 3.4, the presence of the substrate nearby hardly changes the nanobeam photonic crystal cavity's far-field pattern at all. Regardless of h , radiation from the cavity is 80% linearly polarized in the y -direction when $s = 52$ nm and 75% y -polarized for $s = 34$ nm.

Device fabrication

The laser devices are made on epitaxially grown quantum well materials. The generalized sequence of device fabrication follows the standard planar lithography used in semiconductor device manufacturing, where we have two options for defining the etch mask: a photo- or electron-beam resist mask, or a hard mask such as SiO_x , SiON , or metal. Design of the fabrication process begins with the critical step of semiconductor dry etch using ion beam or plasma. The other process materials and parameters evolve from how well they work with the dry etch recipe at hand.

Compared with disk laser structures, which involve open-space etching with relaxed requirement on etch verticality [83, 114], photonic crystals have a particular intolerance for fabrication errors that deviate from the design [147, 148]. To etch III-V compounds involving indium, we can use either chlorine or iodine as the halogen reagent. The main by-product InCl_3 has a melting point of 586°C and a boiling point of 800°C [152, 153], resulting in a passivating layer on the surface, unless it is heated to increase volatility and evaporate off of the substrate during the etch. An iodide etch chemistry forms InI_x as by-products, of which InI_3 has a melting point of 210°C and a boiling point of 500°C , InI has a melting point of 350°C and a boiling point of 710°C , and InI_2 a melting point of 225°C [152, 154]. The InI_x by-products have enough volatility due to local heating during the etch, so that we can carry out the etch without the need for a heated substrate stage. We were able to implement these etch chemistries using either inductively-coupled plasma reactive ion etch (ICP-RIE) or chemically-assisted ion beam etch (CAIBE). The basic operations of both ICP-RIE and CAIBE are laid out in the following sub-

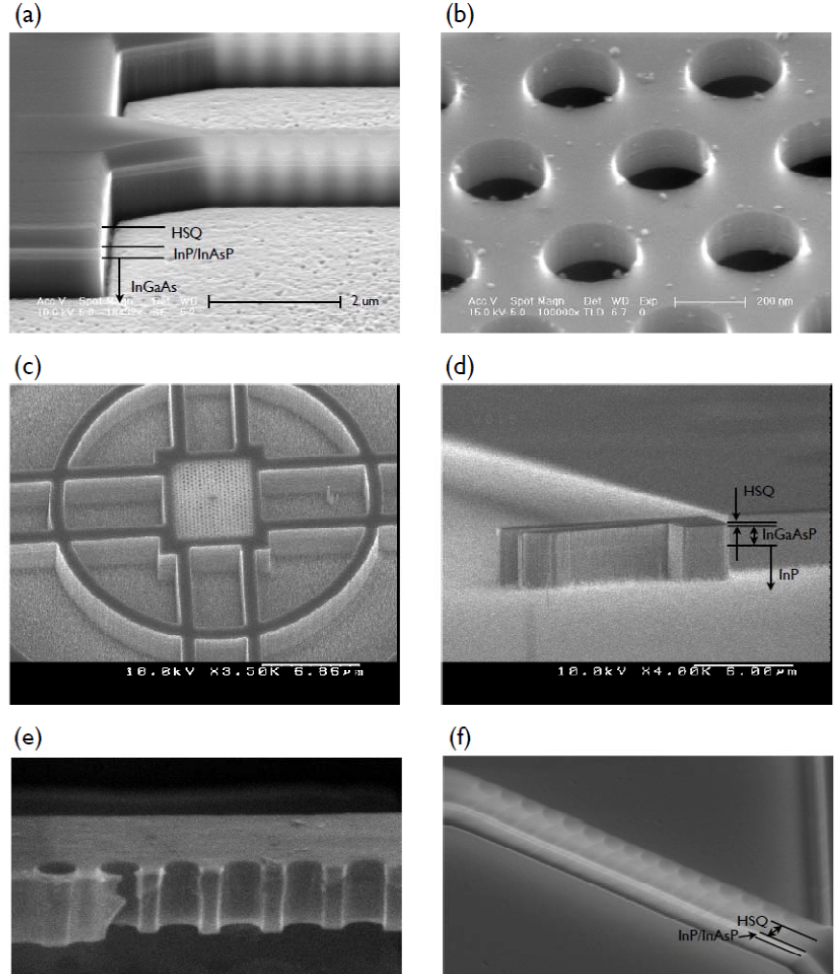


Figure 4.2: Etch results from optimized recipes: (a){(b) InP with InAsP QWs etched using CAIBE; (c){(d) InGaAsP etched using CAIBE; (e) AlGaInP etched using ICP-RIE with $\text{Ar}/\text{H}_2/\text{Cl}$ chemistry; (f) InP etched using ICP-RIE with $\text{CH}_4/\text{H}_2/\text{Cl}_2$ chemistry.

sections, followed by details of our optimized etch recipes. We developed three options to etch our indium-compound quantum well material: First, ICPRIE without heated stage using Ar/H₂/HI gas chemistry; second, ICP-RIE with heated stage using CH₄/H₂/Cl₂ gas chemistry; third, CAIBE with heated stage using Ar/Cl₂ chemistry. Most etch recipe calibration is in essence striking a balance between physical milling and chemical etching to optimize side wall verticality and etch rate, and a balance between semiconductor etch rate and mask erosion rate. However, we would like to add a word of caution for high temperature CAIBE. First, when Cl₂ ow is too high, the sample will undergo spontaneous chemical etch when at elevated temperatures of 135 – 160 °C, even in the absence of any ion beam, as shown in Figure 4.1(a). Etch temperatures can be as high as 190 °C to avoid solid In_xCl_y micromasking the device. The solution to curb spontaneous isotropic etch is to reduce the Cl₂ ow rate. Second, when Cl₂ is introduced through small nozzles in the chamber, the gas may not diffuse evenly over the sample, resulting in non-uniform etch rates and profiles, shown in Figure 4.1(b). One can carefully center the sample below the Cl₂ nozzle, or use a ring-shaped shower head gas inlet to evenly distribute Cl₂ in the chamber. After many etch calibrations and sad-looking samples, we arrived at the optimized recipes and results shown in Figure 4.2.

An appropriate etch mask needed to be developed to use with the etch recipes. Criteria for the etch mask include high etch resistance giving high etch rate contrast and vertical sidewalls to minimize signs of mask erosion on the resulting device. Figure 4.3(a) and (b) show problems with mask deformation due to local heating and etch artifact due to mask erosion, respectively. Photonic crystals' small air-holes pose an additional challenge. Gas species diffusion is also limited in small holes in the substrate compared with large open areas, and so etch rate decreases as is evident in Figure 4.3(c). The high ICP power or high etch temperature required in the dry etch makes polymer resists with a carbon backbone, such as the commonly used poly(methyl methacrylate) (PMMA) or even ZEP520₂, extra vulnerable to deformation and erosion. The absence of a good SiO_x or SiON etch recipe at the time dissuaded the use of dielectric hard masks. Metal masks tend to distort the local electromagnetic field and temperature profile, resulting in artifacts such as undercut and not very vertical side walls that proved difficult to eliminate. Our best option came when we developed a high-contrast e-beam lithographic process on very thick hydrogen silsesquioxane (HSQ) resist[a high resolution negative tone resist that can be exposed using extreme ultraviolet (EUV) [155] or electron beam [156, 157, 158]. It consists of a network of Si-O-H polymer, whose monomer structure is shown in Figure 4.5(a) [159]. Upon exposure to electron beam and immersion in tetramethylammonium hydroxide (TMAH), the resist gives up H₂ and becomes an amorphous Si_xO_y; unexposed resist dissolves completely in TMAH. Exposed and developed HSQ has an etch resistance slightly lower than thermally grown or plasma-enhanced chemical vapor deposition (PECVD) grown SiO₂, but much higher than any carbon-based polymer. Moreover, our high-contrast lithography gives vertical side walls regardless of pattern feature size (Figure 4.5) The etch resistance of HSQ mask depends on the amount of ion milling and plasma power in the etch. We found that high power plasma, predominant in ICP-RIE etches, is much more efficient at resist thinning than high power ion milling that is predominant in CAIBE. Moreover,

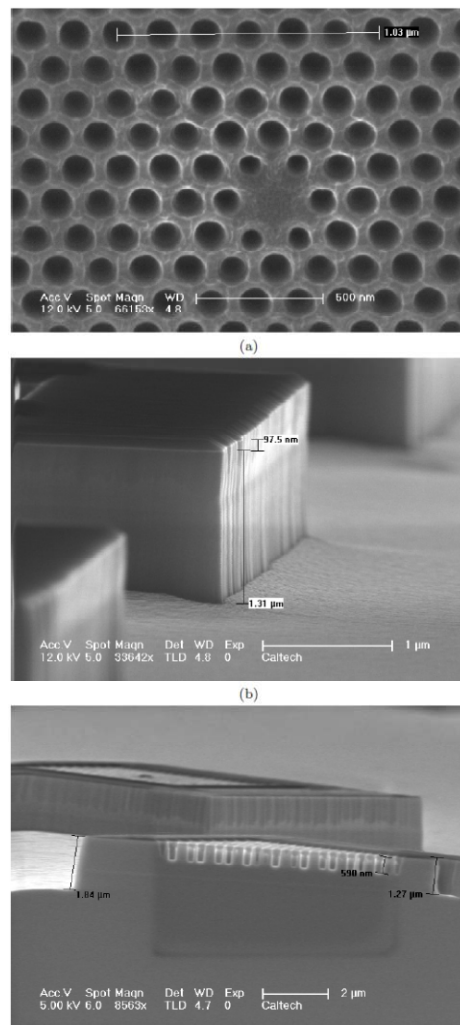


Figure 4.3: Common dry etch problems encountered in etching photonic crystals in In-based III-V compound: (a) air-hole non-uniformity due to PMMA mask deformation during etch; (b) rough side wall due to mask erosion; (c) non-uniform etch rate due to device feature size.

ICP-RIE etch rate appears to decrease much more rapidly with decreasing air-hole size, thus reducing etch selectivity in small device features.

Following the dry etch, a wet-etch is needed to remove the sacrificial InP or InGaAs layer. To remove InP from 1.12Q and 1.3Q InGaAsP, we use 4:1 HCl:H₂O at 4 °C [160]. To remove InGaAs from InP and InGaAsP, we developed a version of the H₂CrO₄:HF etchant mentioned in [161], diluted in H₂O and used at room temperature. Its etch rate depends on the dilution and whether the solution is freshly made. Regardless of etch rate, however, the wet-etch selectivity against 1.12Q InGaAsP is about 30:1, 40:1 against 1.3Q InGaAsP. Selectivity of InGaAs against InAsP and InP is near infinite; by that we mean that in undiluted H₂CrO₄:HF, we were able to undercut into >30 μm of InGaAs when the epitaxial layer is only 100 nm thick, all the while with no visible damage to InP/InAsP. SEM image from H₂CrO₄:HF:H₂O etch rate and selectivity test are shown Figure 4.7.

Complete fabrication procedure

After developing and optimizing each step of the fabrication procedure, our final process is summarized here. Finished devices are shown in Figures 4.8-4.10.

1 E-beam lithography

- _ Beam voltage: 100 kV
- _ Resist: FOx-16 from Dow Corning
- _ Spin at 4000 RPM for 375 nm resist thickness
- _ Bake at 170°C for 2 min
- _ Expose at 250-700C/cm², depending on substrate material and feature size
- _ Develop in AZ 300MIF at 70°C for 4 min, rinse in H₂O, N₂ blow dry

2 Dry etch

- _ For deep etch, use CAIBE:
- InP/InAsP/InGaAsP etch rate is 1.8 μm/min, HSQ resist erosion rate is 80 nm/min

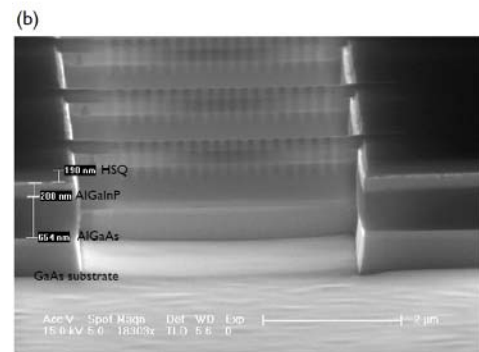
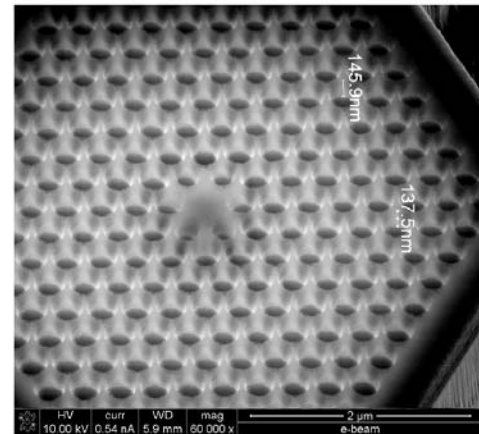


Figure 4.6: SEM images of HSQ mask after dry etch: (a) 140 nm of HSQ resist remains after CAIBE; (b) 190 nm of resist remains after Ar/H₂/HI ICP-RIE.

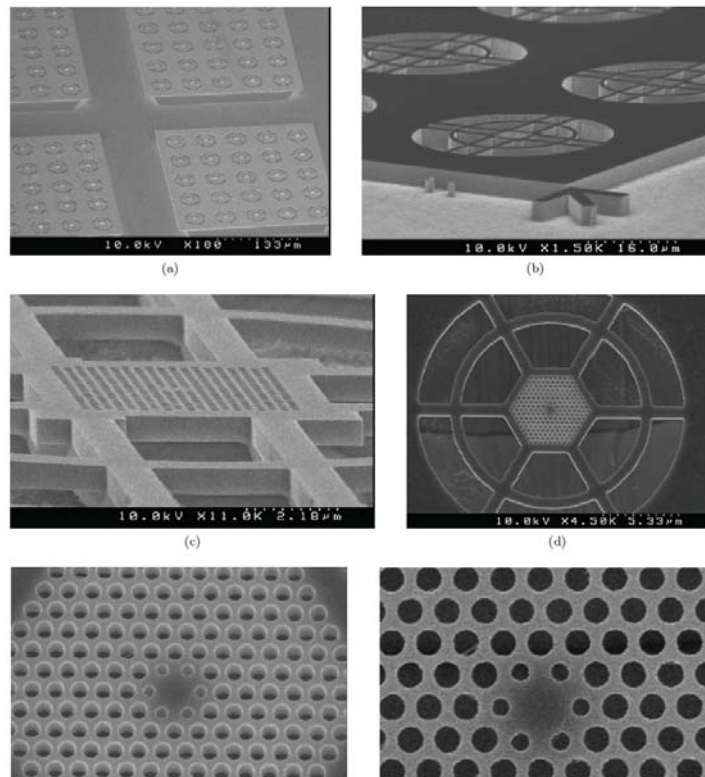


Figure 4.8: SEM images of finished thick-slab microlasers, active material is 1.3Q InGaAsP quantum wells in 1.12Q InGaAsP cladding, in order of progressive zoom-in: (a) arrays of thick-slab lasers ready for testing; (b) after CAIBE etch before wet etch, etch depth is 3 μm; (c) glancing angle view of a finished device, slab thickness is 606 nm; (d) top view of an undercut device; (e) a tilted view of the air-holes, showing straight CAIBE etched sidewalls and very little damage from wet etch; (f) top view close of the cavity region, air-hole periodicity is 305 nm.

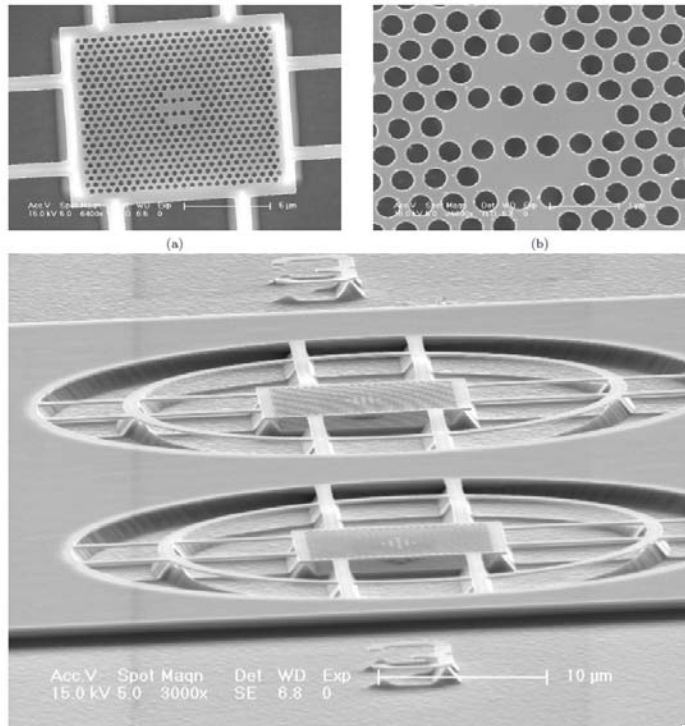


Figure 4.9: SEM images of finished coupled-cavity microlasers, active material is InAsP with InP cladding

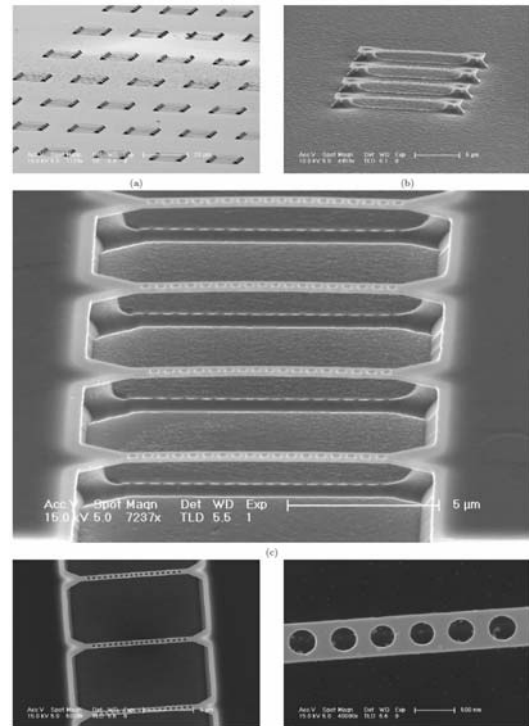


Figure 4.10: SEM images of finished nanobeam photonic crystal microlasers, active material is InAsP quantum wells in InP cladding.

Table 4.2: Calibrated etch recipes for III-V compounds with In, including InP, InGaAsP, InAsP, AlGaInP

(a) Ar/H₂/HI ICP-RIE

Parameter	Value
Ar flow	3 sccm
H ₂ flow	10 sccm
HI flow	30 sccm
Chamber pressure	10 mT
Forward power	90 W
ICP power	900 W
Stage temperature	Not controlled
He backing flow	0

(b) CH₄/H₂/Cl₂ ICP-RIE

Parameter	Value
CH ₄ flow	8 sccm
H ₂ flow	14 sccm
Cl ₂ flow	18 sccm
Chamber pressure	4 mT
Forward power	180 W
ICP power	2200 W
Stage temperature	120 °C
He backing flow	10 Torr

(c) Ar/Cl₂ CAIBE

Parameter	Value
Ar flow	5 sccm
Cl ₂ flow	1.4 sccm
Cathode	5.9 A / 6.0 V
Discharge	0.34 A / 40 V
Beam	30 mA / 750 V
Acceleration	2.6 mA / 100 V
Neutralization	22 mA
Stage temperature	190 °C

or III-V slab thickness of >250 nm, ICP-RIE can be used without resist erosion artifact

3 $\text{H}_2\text{CrO}_4\text{:HF:H}_2\text{O}$ wet-etch

- _ Dissolve 10 g CrO_3 in 100 g H_2O
- _ Mix H_2CrO_4 solution, 48% HF, and H_2O with ratio 1:1:460
- _ At 4°C , InGaAs to 1.12Q InGaAsP selectivity is 30:1, InGaAs to 1.3Q InGaAsP selectivity is 40:1, InGaAs to InP selectivity is $>5000:1$.

4 Drying after wet-etch

- _ For 2D photonic crystal, rinse in H_2O , N_2 blow dry For nanobeam photonic crystal, rinse in filtered IPA, critical-point drying required

Microlaser characterization

In the absence of an electrical current path through the laser cavity, such as a p-i-n doping profile to allow current injection to the QW or QD layers [17, 162, 163], optical pumping is used to excite the laser cavity. A light source with shorter emission wavelength than that of the gain material generates electron-hole pairs that recombine to give off spontaneous emission or coherent light when lasing is achieved in the microcavity. By analyzing the optical pump power absorbed and the power, spectrum, mode pattern, and polarization of light emitted by the cavity, we can evaluate our numerical simulation and theoretical prediction, and parse out details of the microlaser's characteristics. In the measurement, the sample is mounted on an xyz stage. A 830 nm pump laser light is collimated, then focused through a long working distance 50x microscope objective to a $4\text{-}\mu\text{m}$ diameter spot on the sample at an angle normal to the surface. The pump laser is actuated by a function generator, which tunes the pump light duty cycle from 1% to 100% CW. A small percentage of it is split off by a low reflection beam splitter to a broad area Si photodetector for measuring pump laser power at the particular operating voltage and duty cycle. Emitted light from the sample is collected by the same objective lens, re-directed by the 50-50 beam splitter to a lower power objective, which focuses the signal into a multimode optical fiber connected to an optical spectrum analyzer (OSA). A collimated white light, a flip mirror, and a CCD camera are integrated into the measurement set-up for visual alignment of the pump spot and the microcavity devices. A long pass filter with a cut-off wavelength of 1150 nm is placed in the beam path after the 50-50 beam splitter to block most of the 830 nm pump light from the CCD camera and the OSA. The microlasers studied in this work emit at $\lambda = 1.3$ or $1.55\text{ }\mu\text{m}$. The photoluminescence measurement set-up is shown in Figure 5.1.

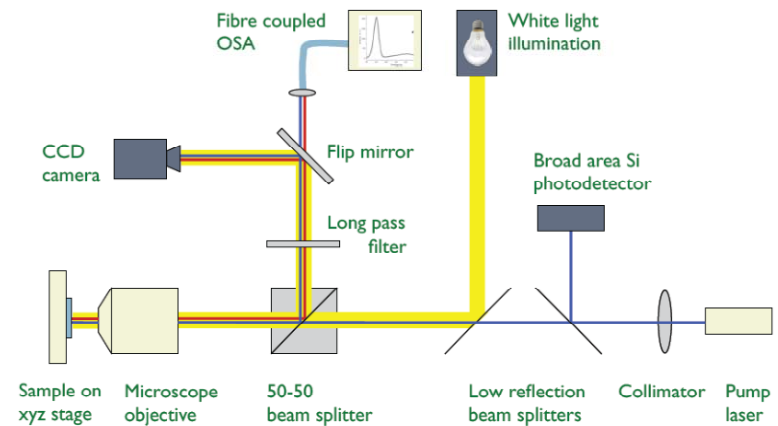


Figure 5.1: Photoluminescence measurement set-up used to characterize microlasers. Blue lines indicate pump laser path, red lines indicate path of light emitted from the microlaser device. Thick yellow line is the path of the white light illumination.

When we scan the sample by passing the pump laser spot over the arrays of microcavities, it is not difficult to distinguish lasing devices from the non-lasing ones. On the CCD camera, incoherent light from non-lasing devices appears as a diffuse spot, while coherent light is much brighter and shows distinct fringe patterns that result from the interference of a monochromatic light. In fact, for devices operating at its longest lasing duty cycle, we see its emitted light turn to a diffuse spot when duty cycle is increased and return to a fringed pattern when duty cycle is turned down again. The fringe pattern mentioned above is itself a manifestation of coherence [26]. In spectral measurement, it is characterized by sharp peaks with narrow linewidths $<100\text{ pm}$ in CW lasers and can be a few nm in pulsed operation when widened by thermally induced wavelength chirping [86] and peak intensity much above the background noise. Then, the device's output power as a function of the input pump power is recorded. The result is a light-in versus light-out (L-L) curve. Most lasing devices so far experimentally realized still have a moderate F_p value, such that the L-L curve has a discernible threshold, beyond which output power increases linearly with

much higher differential efficiency dL_{out}/dL_{in} than below threshold. More than an evidence of lasing action, the L-L curves can be fitted to the laser rate equations to extract more quantitative data about the device.

When the devices achieve CW lasing, linewidth narrowing as pump power increases is another signature of lasing. Turning up the pump power from zero, the below-threshold linewidth narrows as described by the Schawlow-Townes linewidth formula. When the pump power reaches the threshold region, linewidth broadens slightly with increasing power due to gain-refractive index coupling. Then as pump power rises beyond the threshold, laser linewidth narrows again, given by the non-modified Schawlow-Townes formula [164]. The threshold region thus represents a kink in the decreasing trend of linewidth as a function of power. Linewidth measurements are not quite applicable when the devices operate in pulsed mode; thermal chirping brings overwhelming phase noise and results in linewidth widening with increasing pump power [86]. Lastly, a direct proof of lasing action is given by coherence measurement of photon correlation functions [165, 166]. The second order function as a function of pump power L_{in} , where $hI(t)$ is the expectation value of intensity at time t , has been experimentally implemented [124, 167]. Second order photon correlation measurements were not performed in this work. However, it becomes increasingly important in proving above-threshold lasing and determining threshold pump power as the research field gets closer to demonstrating high F_p laser with thresholdless-like L-L behavior. In the subsequent sections where we present results from device characterization, we pay particular attention to several metrics to quantify the quality of our microcavity lasers: (1) room temperature CW operation, (2) threshold pump power, (3) far-field emission directionality, (4) thermal resistance manifested by the emission wavelength as a function of input power, and (5) comparative differential quantum efficiency measured by the slope of L-L curve above threshold.

Thick-slab laser results

We defined the photonic crystal cavities using high-contrast electron-beam lithography with thick HSQ resist and high temperature Ar/Cl₂ CAIBE. The sacrificial InP layer was removed in a selective wet chemical etch of H₂CrO₄/HF/H₂O. Particulars of the fabrication recipes are detailed in Section 4.4. SEM images of finished devices are shown in Figure 4.8. The thick-slab microlasers are photopumped at room temperature using a 832 nm laser diode with a 1 MHz repetition rate and 2% duty cycle. L-L curve and lasing spectrum for one of the devices is shown in Figure 5.3.

We compare the lasing wavelength of 1323.7 nm with the resonance wavelength from FDTD simulations, and confirm that the laser emission comes from one of the degeneracy-split dipole modes. The linewidth in the figure may seem wider than should be for a laser, although a resolution of 0.1 nm was used in the spectral scan. The reason is that when pumped at 2% duty cycle, thermal chirping in the cavity results in significant frequency noise [86, 185]. We assume that the pump light undergoes multiple reflections at the slab and substrate interfaces and the fraction that overlaps with the cavity area is absorbed. Thus, 20% of the incident power contributes to carrier generation in the slab; the effective peak pump power is estimated to be 78 μ W [101]. With these results, we show that photonic crystal cavities in optically-thick slabs can have enough Q to achieve room temperature lasing. Although the present work only demonstrates optically pumped devices in pulsed operation, we believe that improvement in material quality[such as InAsP/InP QWs used coupled-cavity and nanobeam photonic crystal laser presented in subsequent sections]can help us achieve CW lasing, and that we can take advantage of the increased slab thickness to better design p-i-n doped epitaxial layers for more efficient current injection.

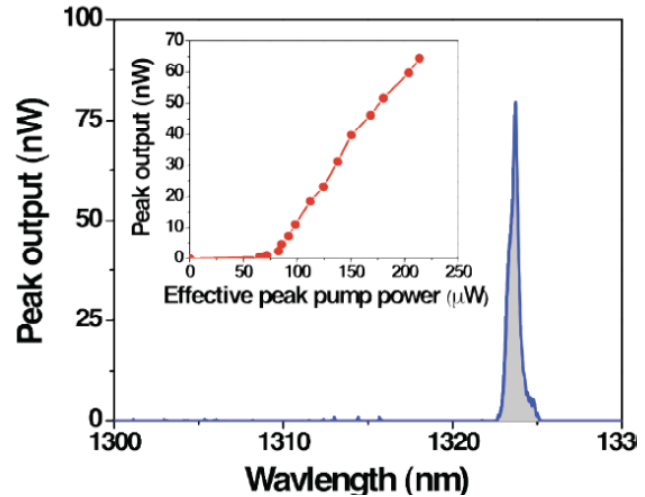


Figure 5.3: Characteristics of the thick-slab laser: single mode spectrum, inset is the L-L curve when the device is pumped at 1 MHz and 2% duty cycle.

Coupled-cavity laser results

We show experimental measurements of fabricated devices and fit the measured data to laser rate equations to estimate the lasers threshold, spontaneous emission coupling factor β , as well as the $1.5\ \mu\text{m}$ wavelength emitting InAsP/InP QW material properties for future nanolaser designs in this not yet commonly used material system.

Our devices are formed in an InP slab with a thickness T of $240\ \text{nm}$ on top of a $1.16\ \mu\text{m}$ thick sacrificial InGaAs layer. The InP slab contains 4 InAsP QWs with the photoluminescent emission peak at $1550\ \text{nm}$. The samples are fabricated using electron beam lithography on PMMA resist, followed by CAIBE with Ar/Cl_2 to form the air holes and an oxygen plasma to remove the residual resist. Finally, the InGaAs layer is etched away in a dilute $\text{H}_2\text{CrO}_4/\text{HF}$ mixture to suspend the InP/InAsP PhC slab. The best performing devices have a lattice period of $a = 470\ \text{nm}$ and air hole radius of $r = 0.3a$. Figure 4.9 shows SEM images of finished devices. The coupled-cavity lasers are measured in a photoluminescence set-up at room temperature, pumped continuously with a $\lambda = 832\ \text{nm}$ diode laser. The pump laser beam is focused to an approximately $4\ \mu\text{m}$ diameter spot on the sample surface using a $50\times$ microscope objective. Emitted light from the devices is collected through the same objective and recorded using an optical spectrum analyzer (OSA). Finite-difference-time-domain (FDTD) simulations reveal that the coupled-cavities in Design A have several resonance modes within the InP/InAsP QW material's gain spectrum, among which the highest Q mode has a Q of 3100, while all other modes have Q of a few hundred to 1300. In Design B, the highest Q mode within the photoluminescence bandwidth is 1700, all other modes have Qs of below 1000. Only the highest Q mode, whose mode profile is shown in Figure 3.19, tends to achieve the lasing threshold condition, making our devices single-mode lasers, as is evidenced in measured lasing spectra shown in Figure 5.4. CCD camera images of lasing devices are shown in insets. They represent vertically directed Poynting energy

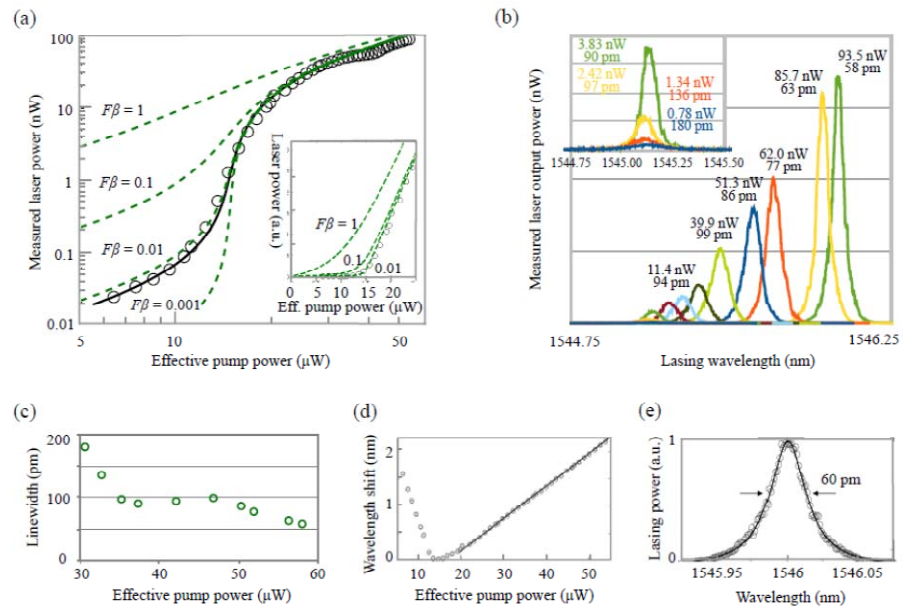


Figure 5.5: Design B device measurements: (a) rate equation fitted L-L measurement on log-log scale, circles represent measured data, solid black line is the fit, calculated $F\beta = 1, 0.1, 0.01$, and 0.001 . L-L curves using the fit data are in green dashed lines. Inset shows a zoom-in at the threshold in linear scale. (b) Linewidth narrowing and wavelength shift at different pump powers. (c) Lasing linewidth as a function of pump power. (d) Measured wavelength shift versus effective pump power, solid line is the above-threshold $d=dW$ fit. (e) Measured linewidth, solid line shows the Lorentzian

ux P_z from the lasing mode at approximately one lasing wavelength above the devices' top surface. The corresponding FDTD simulations of this Poynting ux distribution confirm the main features in the lobed patterns seen on CCD: Design A has two major side lobes, Design B has a bright center with four minor lobes. Figure 5.4: Lasing spectra of coupled-cavity lasers, insets show CCD camera image of the lasing device and the corresponding FDTD simulation results: (a) Design A; (b) Design B. InAsP/InP QWs have the potential advantage of higher temperature and lower threshold operation, due to their greater band-

edge ϕ_{set} and thus better carrier confinement compared with the commonly used InGaAsP/InP QW slabs [186]. However, this material system has not received much attention for 1.55 μm wavelength-scale lasers. We proceed to characterize our best performing device using Design B to provide more insight into device performance and material properties. We estimate that about 1 percent of the laser's output power is coupled to the OSA due to loss through optical elements in the optical path from the device to the OSA. Thus the coupled-cavity laser's output power is on the order of 10 μW .

One important consequence of high power, room temperature CW laser operation is that the lasing linewidth is not smeared by phase noise from thermal chirping and narrows as output power increases [71, 86]. This ability to obtain narrow linewidth directly influences the device's performance in applications such as spectroscopy and coherent optical communication. We measure the lasing spectrum at different pump powers and overlay the data in Figure 5.5(b), which shows both a linewidth narrowing and a wavelength red-shift when the effective pump power increases from 30 μW to 60 μW . As a function of pump power is extracted and plotted in Figure 5.5(c). At threshold, phase transition into lasing results in a pronounced kink in the linewidth decrease [164]. To determine the actual achievable linewidth when the coupled-cavity device is pumped at high powers, Figure 5.5(e) shows a single linewidth measurement when the device is pumped at 3 times the threshold pump power. The data is fitted to a Lorentzian. We find that the FWHM is 60 pm. Measurement accuracy is limited by the OSA's minimum achievable resolution of 15 pm.

Another feature seen in Figure 5.5(b) is that lasing frequency shifts with increasing pump intensity as the combined result of blue shift due to carrier plasma effect with increased free carrier density in the cavity and red shift due to device heating. A more detailed measurement of lasing wavelength shift versus effective pump power is plotted in Figure 5.5(d), clearly showing free carrier dominant blue-shift below threshold and heating dominant red-shift above threshold. The red-shift measures to be 0.059 nm/ μW . From this data, one can estimate the device's thermal resistance. at 0.615 K/ μW , a value comparable to devices of the same dimensions made in InGaAsP QW materials [96]. This lead us to conjecture that the low N_{tr} and high thermal tolerance of InP/InAsP QW materials contribute significantly to the low threshold, high power room temperature CW operation achieved here.

The coupled-cavity lasers demonstrate very stable and high power room temperature CW singlemode operation on the order of 10 μW , with a very low threshold of 14.6 μW despite having 4 QWs as the gain material and a larger cavity area compared with single-defect cavities. They have directional emission with 40% of the light emitted from the lasers top surface and have a FWHM beam divergence of 20° in the x-direction and 8° in the y-direction. The devices exhibit one of the narrowest linewidths reported so far in photonic crystal lasers. For comparison, Kita and colleagues reported a linewidth of 60 pm for point-shift lasers suspended in air [86]. This makes the coupled-cavity lasers useful for applications ranging from refractive index sensing to being the light source for potential on-chip optical signal processing. The larger area coupled-cavity will be advantageous in applications where both the laser output power and the threshold are of concern. However, the cavity's large V_{eff} of $1:9(\lambda/n)^3$ precludes it from showing enhanced spontaneous emission|a sharp threshold transition remains. Moreover, the 2D photonic crystal slab experiences significant influence from substrate feedback, partially evidenced by the obvious modification of far-field radiation pattern by the size of the underlying air-gap h (Figure 3.20). In the next section, we proceed to address these two weaknesses using a nanobeam photonic crystal laser design.

Nanobeam photonic crystal laser results

The nanobeam photonic crystal cavities are designed in hope of showing lasing with enhanced spontaneous emission due to their high F_p , and of finding out more about the InP/InAsP QW material's thermal tolerance as nanobeams are expected to have much higher thermal resistance than the 2D slab photonic crystal cavities. Our devices are made in the InP/InAsP QW material detailed in Chapter 4. They are defined using e-beam lithography with FOX resist, followed by Ar/Cl_2 CAIBE, dipped in HF to remove residual resist, and finished with $\text{H}_2\text{CrO}_4/\text{HF}/\text{H}_2\text{O}$ wet etch and critical point drying to remove the sacrificial 1.06 μm thick InGaAs layer. The devices we fabricated include a range of design parameters: a

= 430 - 480 nm in steps of 10 nm, $W = 1:06a$, $s = 0, 18, 34$, and 52 nm. SEM images of the finished devices are shown in Figure 4.10.

Using the photoluminescence set-up, we excite the nanobeam photonic crystal cavities at room temperature with a $\lambda_p = 830$ nm pump laser. FDTD simulation predicts a single resonant mode within the InP/InAsP QWs' gain spectrum. Modulating the pump laser at 1 MHz, we tune the duty cycle from 5% through to 100% CW. At 10%, lasing is observed in all of the devices, with emission wavelength ranging from 1314 nm to 1524 nm depending on their design geometries a and s as well as variation in dosage during e-beam lithography. Although the InP/InAsP material exhibits such a large gain spectrum, only single mode operation is observed for each individual nanobeam device. Because the QW material is designed for peak gain at 1550 nm, devices lasing at shorter wavelengths have higher threshold, lower output power, and many stop lasing when the pump duty cycle increases. Devices with $\lambda_l > 1500$ nm have noticeably better performance. We focus our attention on two of the best performing devices, whose parameters are detailed in Table 5.3, to further analyze their characteristics. Pumping

the devices at 5% - 15%, we can measure a bright single-mode laser peak within a 1250 nm to 1650 nm spectrum span. We note that at 15%, the pump pulse width of 150 ns is already much longer than any recombination time scale in the device, corresponding to a quasi-CW regime of operation. The laser signal is ~ 17 dB above background noise. As we turned up the pump power, the devices showed little sign of thermal degradation at higher powers. The L-L curves at these duty cycles show a soft turn-on at threshold transition that is a trait of high F_p lasers with enhanced spontaneous emission into the lasing

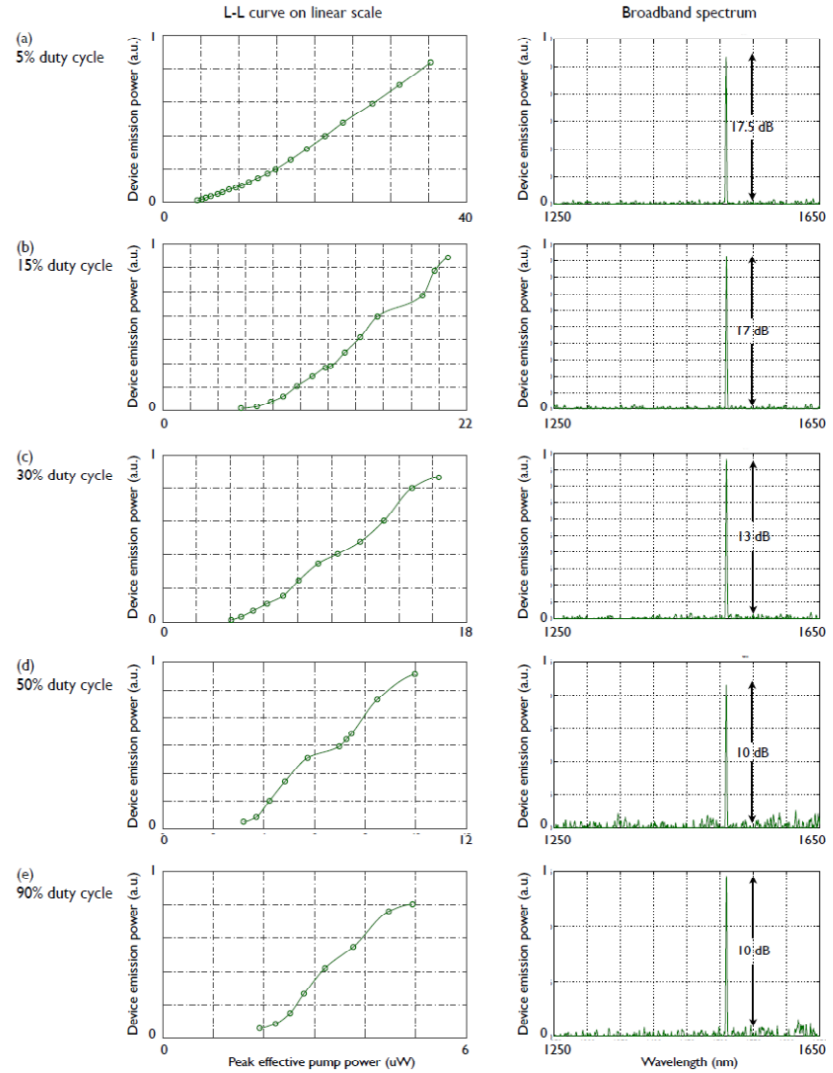


Figure 5.6: L-L curves and broadband spectra of Device B optically pumped at various duty cycles. Duty cycles are (a) 5%, (b) 15%, (c) 30%, (d) 50%, and (e) 90%. $Q = 6500$ from FDTD simulation, $V_{eff} = 0.646(\lambda/n)^3$.

Table 5.3: Design parameters of two select devices for further characterization

Device	a (nm)	W (nm)	s (nm)	Q	V_{eff} (μm^3)	V_{eff} ($(\lambda/n)^3$)	λ_l (nm)
A	480	510	52	4050	0.0908	0.720	1514
B	480	510	34	6500	0.0810	0.646	1510

mode [19, 21, 22]. Examples of L-L curves and broadband spectra

measured on Device B are shown in Figure 5.6. In all of the L-L plots in this section, peak effective pump powers are reported. Peak pump power is the time-averaged power measured with a photodiode divided by the duty cycle. Effective power points to the fact that the $4\text{-}\mu\text{m}$ diameter pump spot size is much larger than the nanobeam photonic crystal cavities footprint on chip. Peak pump power is then multiplied by the fraction of the pump spot that overlaps the device to obtain peak effective pump power. This method provides an estimate of the upper bound of pump power, since not all of the light incident on the cavity is absorbed. Due to the $>10\text{ dB}$ transmission loss in the optical path from the device to the OSA, we are unable to obtain much data below the threshold.

When the duty cycle is increased to 30%, 50%, 70%, and 90%, fringed radiation patterns as seen on CCD camera remain, though dimmer at higher duty cycles. The single-mode peak remains on the

spectral measurement, however with decreasing contrast until 10 dB above background noise at 90% duty, see Figure 5.6(c)(e). The L-L plots show threshold transitions indicative of lasing. When we pump the device in CW condition, however, the fringe pattern disappears, a diffuse spot of light from the cavity is seen on the CCD instead. In spectra measured by the OSA, the single-mode peak all but disappears. Eliminating the 100 ns turn-off time in going from 1 MHz 90% duty cycle to CW pumping, the devices cease to show any sign of lasing. It would seem then the nanobeam photonic crystal cavities show quasi-CW operation up to 90%.

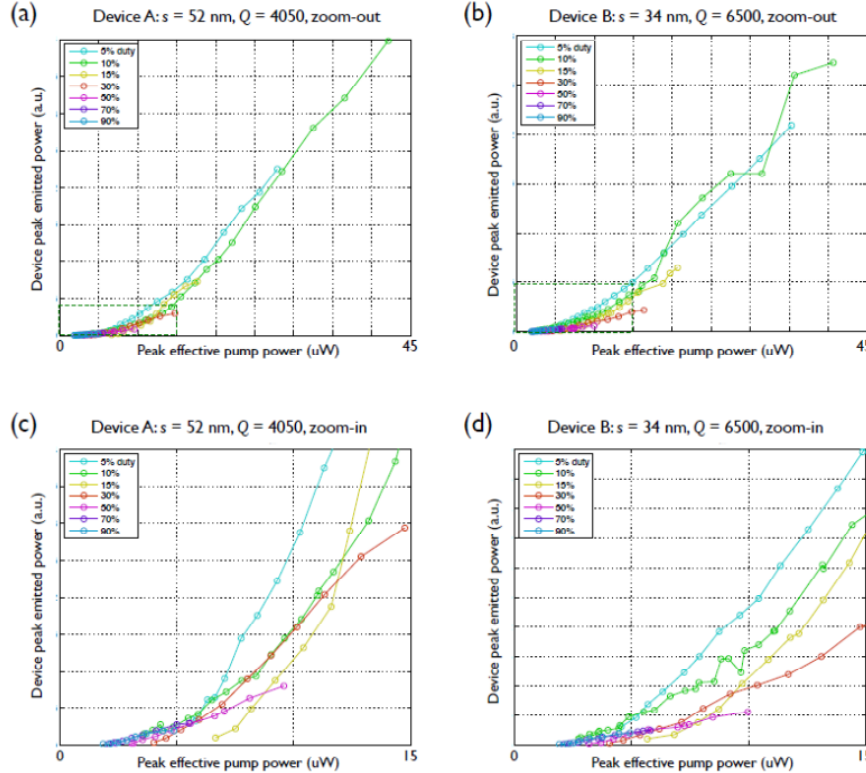


Figure 5.7: L-L curves of Devices A and B on linear scale. (a) and (b) shows all measured data.(c) and (d) are zoom-ins of when pump power is low. They correspond to the area enclosed by the green dotted line in (a) and (b), respectively.

see large differences in the $dL_{out}=dL_{in}$ efficiency between lower and higher duty cycles. $dL_{out}=dL_{in}$ is the differential quantum efficiency η_d [71]. In fact, η_d at 5% duty cycle is 16 times that with 90% duty cycle for Device A, and 10 times for Device B. This much decrease in efficiency would be due to increased heating at higher duty cycles. Similar temperature dependent effects have been observed InGaAsP diode lasers [189]. As a comparison, the $dL_{out}=dL_{in}$ contrast between below and above threshold should be much greater, for example, the coupled-cavity laser in Section 5.5 has an above-threshold $dL_{out}=dL_{in}$ 350 times that of below-threshold. Another characteristic of higher duty cycles of 50% and above, the devices are pumped to a saturated output power at less than three times the apparent threshold, beyond which any extra pump power results in the same output level or lower. In Figure 5.7, L-L curves of 30% _ 90% end at the pump power where the device begins to show saturated output power. While it is likely that the nanobeam devices are lasing at duty cycles up to 90%|second order photon correlation experiments would be needed to validate the coherence of the devices' emission|we believe that their low η_d and output power saturation renders them unsuitable for device applications including refractive index sensing, spectroscopy, or optical signal processing.

The nanobeam photonic crystal cavities are designed for small V_{eff} and single resonant mode within the InP/InAsP QWs' gain spectrum, in hope to experimentally realize characteristics of high F_p lasers. The L-L curves in Figure 5.6 show reasonably soft turn-on at threshold transitions. We proceed to fit the data to the laser rate equations, to extract values of threshold $L_{\text{in,th}}$. The InP/InAsP QW material is not as well characterized as commonly used materials such as InGaAsP, we estimate its material parameters based on several assumptions: first, surface and Auger recombination coefficients A and C are similar to those of InP, detailed in Table 5.2; second, g_0 is similar to other III-V indium compound semiconductors, in the range of 1000 - 2000 cm; third, lifetimes should be on the order of a few ns. If we assume that the spectral linewidth of the InAsP QWs is similar to the 4.3 meV in InGaAsP, then we can calculate F_p . We use the F_p value thus obtained as the upper bound, and vary F_p between it and 1 in the process of rate equation fit. Unlike the coupled-cavity lasers, where the threshold is a pronounced kink in the linear L-L plot and the data on log-log scale is a distinct S-shape, the soft threshold transition of the nanobeam devices means that their log-scale L-L curve is a shallow S-shape. Moreover, due to the devices' low threshold, we could not gather data much below threshold.

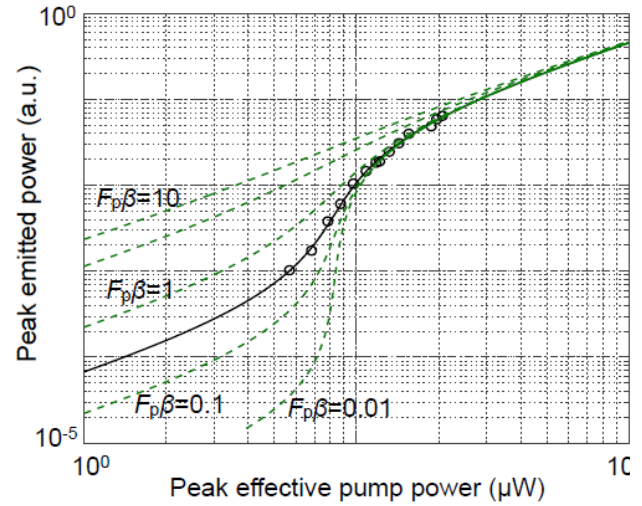


Figure 5.9: d_{λ}/dW measurements at different pump duty cycles: (a) $s = 52$ nm, $Q = 4050$, $V_{\text{eff}} = 0.720(-n)^3$; (b) $s = 34$ nm, $Q = 6500$, $V_{\text{eff}} = 0.646(-n)^3$.

Device thermal resistance and Emission directionality

We expect the main reason that we were not able to push the nanobeam photonic crystal lasers to CW operation is high thermal resistance R_{th} . Even larger area lasers such as microdisk or H7 photonic crystal cavity⁴ can have thermal resistance as high as 10^6 K/W. The air-suspended nanobeams concentrate light into an even smaller volume that is connected to less semiconductor material for heat dissipation; the device thermal resistance must be higher.

We estimate R_{th} using the same method elaborated in Section 5.5.3. We measure d_{λ}/dW and plot the data in Figure 5.9. Unsurprisingly, d_{λ}/dW increases monotonically with pump duty cycle. At 90% duty cycle, d_{λ}/dW is 0.2446 nm/ μ W for $s = 52$ nm and 0.2948 nm/ μ W for $s = 34$ nm.

For both designs, FDTD simulations give $d_{\lambda}/dn \sim 442$ nm/RIU. R_{th} of the nanobeam photonic crystal lasers is 2.63 - 3.18 K/ μ W, five times higher than the coupled-cavity lasers. Moreover, dT/dW at 90%

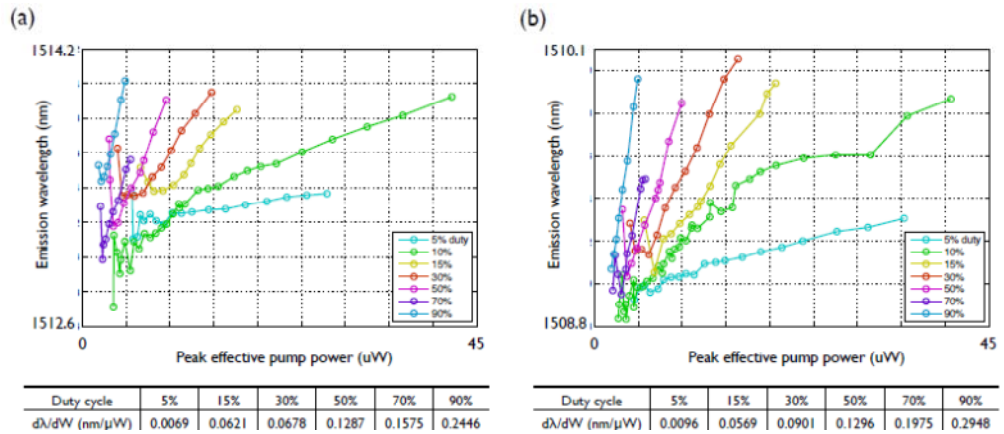


Figure 5.9: d_{λ}/dW measurements at different pump cycles for $s=52$ and $s=34$ nm cavities with Q s of 4050 and 6500, respectively

duty only gives us an estimate, R_{th} for true CW operation would be even higher and, in our devices, seems to be the last straw that prevents room temperature CW lasing.

We notice obvious difference in the radiation pattern from devices with different s . We calculated the far-field radiation pattern of the nanobeam photonic crystal lasers and showed that emission directionality can vary significantly when $s = 0$ versus $s \sim 18$ nm in Figure 24.

This effect is clearly seen in the CCD camera image of lasing devices. In Figure 5.10(a), the left most image is that of a device with $s = 0$. Its emission pattern as seen on the CCD has left and right lobes, corresponding to the two intensity local maxima near 30° in the x -direction in the corresponding far-field radiation pattern in Figure 5.10(b). The two bright spots north of the two-lobed main spot are light reected from an adjacent nanobeam $6 \mu\text{m}$ away. They disappear in devices well isolated from other structures in the y -direction. In contrast, the CCD images of $s = 18, 34$, and 52 nm devices all show a bright oval center spot, corresponding to the intensity maximum within 15° from surface normal in their corresponding FFT calculated far-field pattern in Figure 5.10(b). The respective emission directionality of devices with different s is further confirmed by large domain FDTD simulation, shown in Figure 5.10(c), where even finer features of the emission pattern, such as decreasing amount of light emitted to $>60^\circ$ in the x -direction when s increases from 18 nm to 52 nm, is clearly seen. The fabricated nanobeam lasers confirm our simulation results that increasing s at the center of the cavity vastly improves the emission directionality and the amount of laser output power collected.

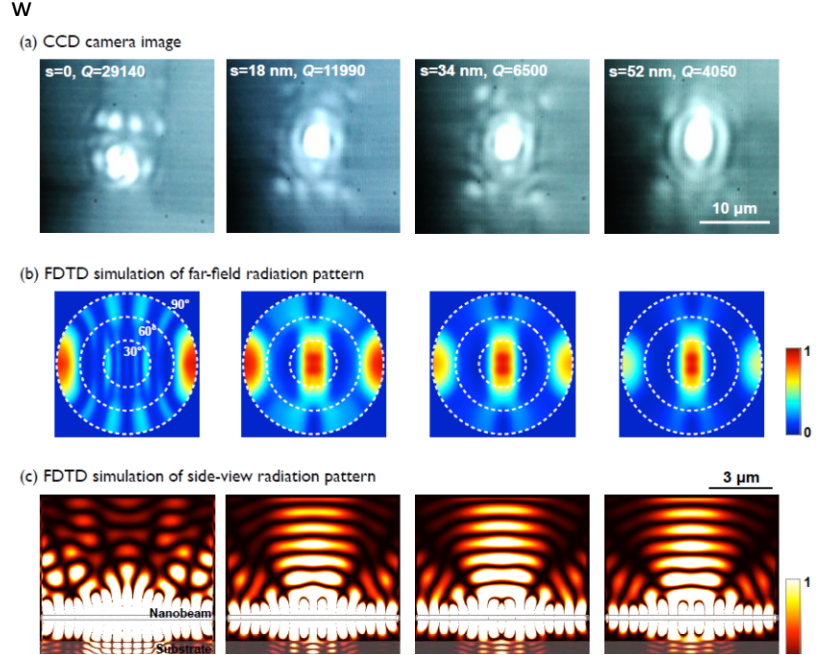


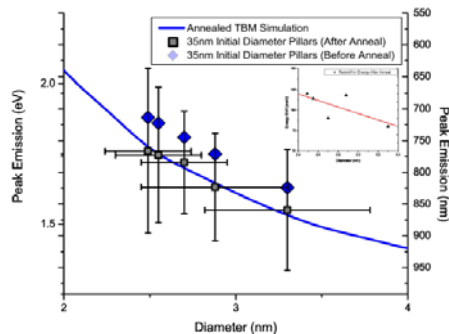
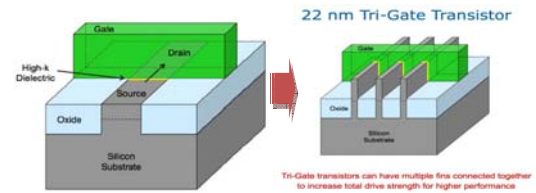
Figure 5.10: Radiation directionality of nanobeam photonic crystal cavities, tuned by varying s : (a) seen on CCD camera; (b) FFT calculation of far-field radiation pattern based on FDTD near-field simulation, dotted white lines indicate 30° , 60° , and 90° from surface normal; (c) y - z plane side-view of radiation patterns from the devices from FDTD simulation, locations of the nanobeam and the substrate are indicated. Columns 1 to 4 correspond to $s = 0, 18, 34$, and 52 nm, respectively. Scale bars for (a) and (c) are shown.

In summary, we designed nanobeam photonic crystal cavities with small V_{eff} of $0.44 - 0.72 (\lambda/n)^3$ and single resonant mode with the gain spectrum of the In/InAsP QW material used in this study, with the goals to experimentally realize high F_p lasing with soft threshold transition and to investigate the behavior of the InP/InAsP material in these high thermal resistance devices. We demonstrate reliable room temperature single-mode lasing with up to 30% duty cycle at 1 MHz repetition rate, a threshold of $6 - 8 \mu\text{W}$ effective peak pump power, and F_p of $0.25 - 0.45$. Laser-like L-L behavior and single-mode emission spectrum are observed up to 90% duty cycles. Based on measurements of emission wavelength as a function of pump power, we estimate the devices' thermal resistance at 90% to be about $3 \text{ K}/\mu\text{W}$. We also confirm in experiment that emission directionality is much improved by introducing a small distance s in the middle of the cavity, as predicted in FDTD and FFT calculations in Section 3.5. Concurrent with this work, room temperature nanobeam photonic crystal lasers were achieved by other researchers in the field, with InGaAsP QWs under 0.27% [190] and 1% duty cycle pulsed operation [60] and InAs/InGaAs QDs embedded in GaAs under CW pumping below the bandgap of GaAs [191].

Silicon Nanowire Results

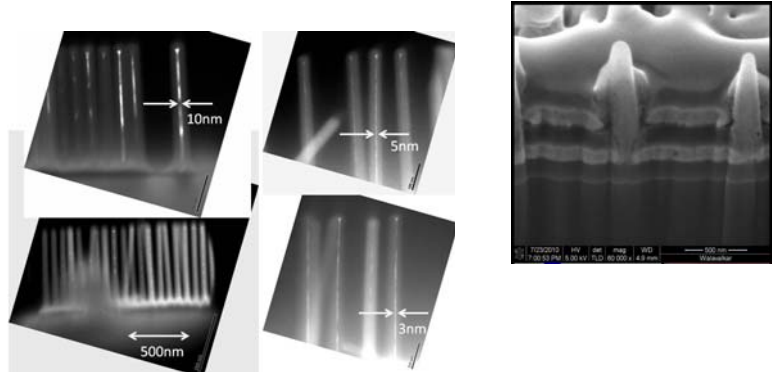
10 nm wide structures and below – Silicon roadmap

Over the past decades, the silicon electronics industry has been able to reduce the sizes of transistors by over 4 orders of magnitude. Now, modern transistors approach the 22nm node and in 2015 transistor structures with lateral dimensions of 10nm are on the Intel roadmap. In modern transistors, silicon channels are surrounded by gates within two-dimensional FINFET structures, and devices are rapidly reaching dimensions at which impurity doping is no longer adequate for reliably controlling transistor performance.



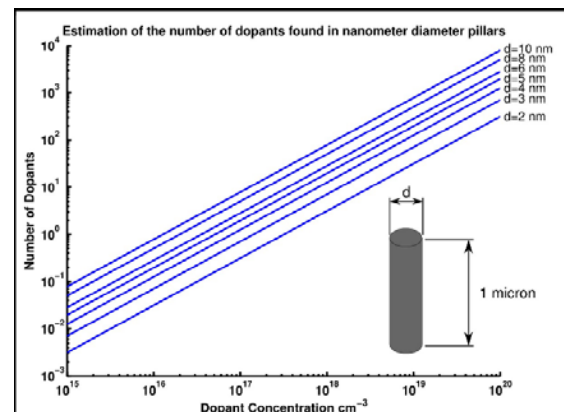
Under the DARPA/NACHOS program, we have developed silicon devices with lateral dimensions even smaller than those developed by the state of the art industry – with channel widths as small as 2nm. In these fully depleted structures, which can be described as lithographically defined quantum wires, we observe large bandgap shifts, from the bulk energy bandgap of silicon of 1.1eV to over 1.5eV. When strain is added to the silicon through an oxidation process, and the silicon quantum wire is oriented in the (100) direction, the bandgap increases even further to energies of over 2 eV. The band structure changes in such small silicon structures to permit more direct and radiative carrier recombination and consequently increased light emission efficiency. Nanometer quantum wires

can be defined from larger, 35nm wide, structures by oxidizing these, and can be fabricated over entire 300mm wafers. The oxidation process self-terminates as the silicon dioxide is formed with a tremendous compressive stress, which ultimately stops the oxygen diffusion process. Thinning through oxidation enables the exploration of manufacturable nanometer quantum structures today that will be relevant to the silicon fabrication infrastructure in the year 2020, and concepts developed based on our quantum wires will readily be translated into realistic devices.

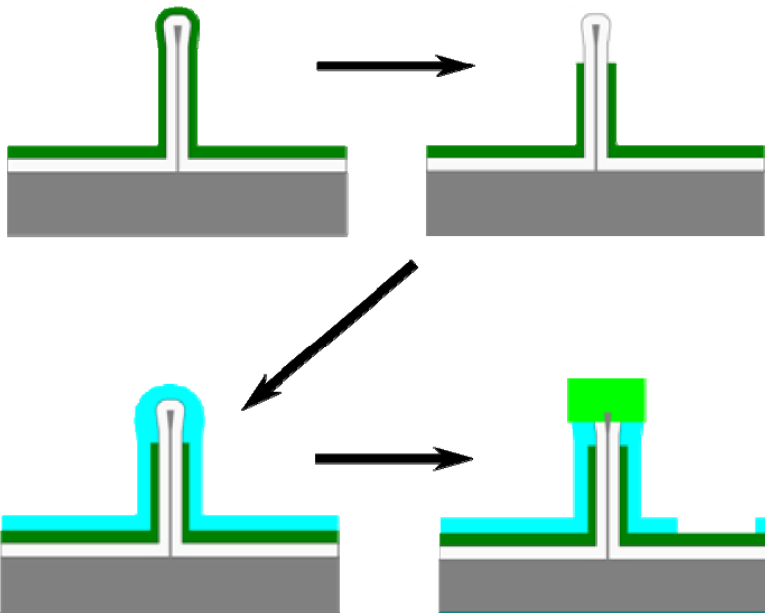
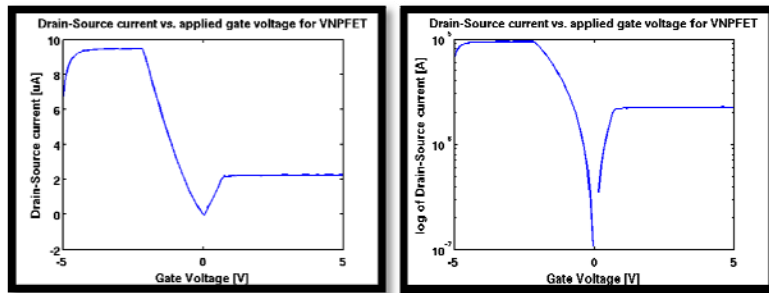


Next generation transistors – fully depleted vertical structures with metal gates

As the size of electronic transistors is reduced from the 32nm to the 22nm node and below, the electronic properties of silicon cannot be controlled through impurity doping through traditional mechanisms such as diffusion or ion implantation alone. Doping no longer provides homogeneous regions of predictable electron densities, but instead results in stochastic variations that limit device reproducibility and prevents the design of reliable circuits. Figure 3 shows graphically the statistics of the number of ionized impurities contributing electrons or holes within nanostructures as a function of their size. Instead of impurity doping, control over carrier densities in



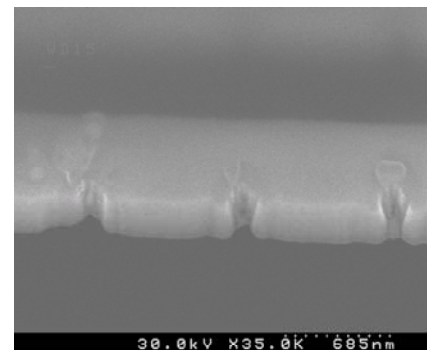
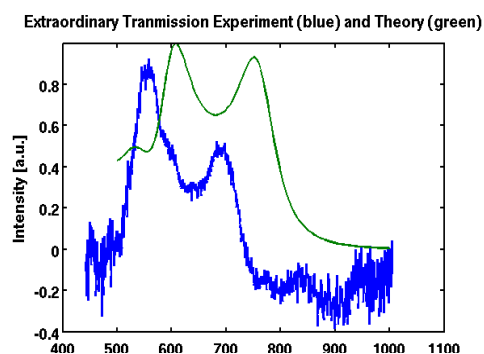
nanostructures can be performed by introducing electrostatic gates that enable the accumulation and depletion of electrons and holes in desired locations. Such gates can efficiently control the interaction

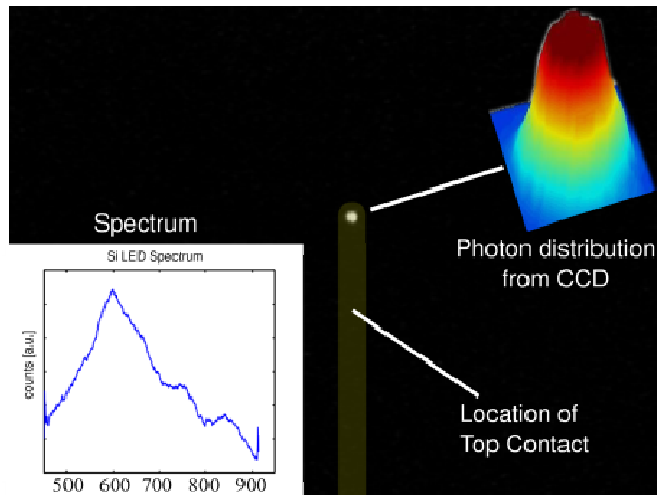


between these carriers to fulfill the device functions. We have developed metal-oxide field effect transistors with vertical channels (V-MOSFETs) based on this principle, and their performance is summarized in Figure 4. By depositing metal gates onto the oxidized vertical quantum wires described above, the channel conductivity can be controlled with “wrap-around” gates. The resulting transistors show much promise in sensors, and are reconfigurable from PMOS to NMOS devices depending on the bias of the gates. Vertical channel MOSFETs also enables low threshold operation and the introduction of optical activity either as a light source or as a detector. One unique property resulting from the control of the carrier densities and transistor function through biased gates is their use in re-configurable circuits where PMOS or NMOS devices can be switched and converted into diodes or other functional electronics. Another exciting opportunity of these devices results from the higher bandgap obtained through quantum confinement in the transistor channels, which results in higher operation temperature ranges. Finally, as these devices are reduced in size to the nanometer scale, their crosssection with ionizing radiation becomes much lower and radiation-hard devices can be defined.

between these carriers to fulfill the device functions. We have developed metal-oxide field effect transistors with vertical channels (V-MOSFETs) based on this principle, and their performance is summarized in Figure 4. By depositing metal gates onto the oxidized vertical quantum wires described above, the channel conductivity can be controlled with “wrap-around” gates. The resulting transistors show much promise in sensors, and are reconfigurable from PMOS to NMOS devices depending on the bias of the gates. Vertical channel MOSFETs also enables low threshold operation and the introduction of optical activity either as a light source or as a detector. One unique property resulting from the control of the carrier densities and transistor function through biased gates is their use in re-configurable circuits where PMOS or NMOS devices can be switched and converted into diodes or other functional electronics. Another exciting opportunity of these devices results from the higher bandgap obtained through quantum confinement in the

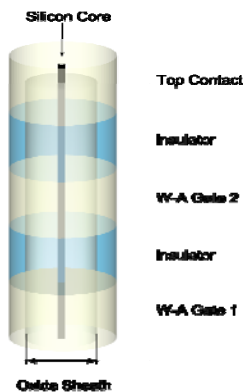
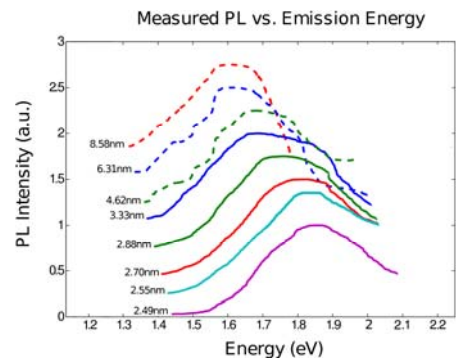
Reconfigurable Optoelectronics by Integrating Plasmonic Metals into Nanotransistors





When converting a fully depleted silicon quantum wire into the channel of a field effect transistor, it is necessary to deposit several gates and contacts (Figure 3) around this semiconductor channel. These contacts are typically metal layers, and can be chosen to be made from low-loss metals, such as aluminum, copper, silver or gold that exhibit plasmon resonances at the same energy as the silicon band-gap. Thus, nano-scale transistors can be designed into plasmonic devices in which the gate geometries can be controlled with nanoscale accuracy. Indeed, arrays of transistors surrounded by a common gate form a planar metal layer perforated with holes where the vertical channels are

penetrating the metal. If the metal surrounding the transistor channels is chosen to be a plasmonic material, the gate metal exhibits the unusual optical properties first described as “extraordinary transmission” in the 1990s. In such devices, light can be transmitted at specific wavelengths due to the coherent interaction between surface plasmons, and light is concentrated within the holes defined through the lithographic patterning of the electronic structures defining the transistor channels. In such devices, optical overlap with the semiconductor transistor channel can be enhanced, and the electronic gates can serve as efficient optical “antenna” structures rendering the transistors optically active into efficient photodetectors. Conversely, Figure 6 shows light emission from an electrically connected silicon nanowire, emitting at a blue-shifted wavelength of 600nm expected for a 2nm quantum wire (Figure 6b), confirming that our small silicon nanostructures can be used as opto-electronic sources. We propose to design more efficient light emitters and detectors by optimizing the metal structure surrounding the silicon nanowires and to improve the optical field overlap with the nanometer-scale silicon conductor.



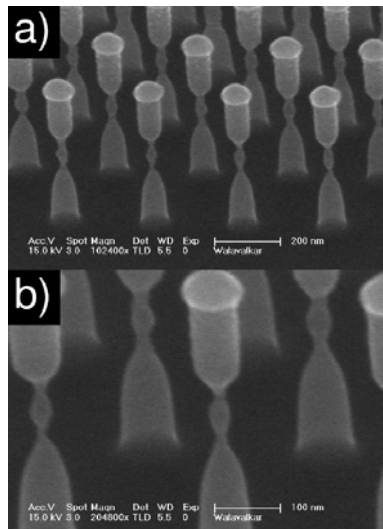
In a light emitter, energy from the recombination of electrons and holes typically generates either light or heat. Within most semiconductors, such radiative and non-radiative recombination takes place, and within an efficient light emitter the radiative recombination predominates. It was shown in the 1990s that by introducing a metal close to the surface of an emitting material, and by choosing the plasmon resonance of the resulting metal/dielectric surface to match the emission energy of the light emitter, it is possible to excite surface plasmons rather than either radiative or non-radiative emission. Indeed, the recombination lifetime of energy into the plasmon mode typically is a much faster process than the typical non-radiative carrier lifetimes found in most semiconductors. If such structures are designed to re-emit the plasmon mode into light, light emitters with a higher radiative efficiency can result. For example, by coating InGaN, with a 10% radiative quantum efficiency with

silver, the emission of light can be increased by over 10-fold. We plan to use the same approach to increase the quantum efficiency of silicon. Indeed, if electrons and holes are injected and recombine within our small silicon channels that are surrounded by gate metal supporting surface plasmons at appropriate energies, the recombination energy can be used to excite surface plasmons with high efficiency. These surface plasmons can be re-radiated by geometrically patterning the metal surface.

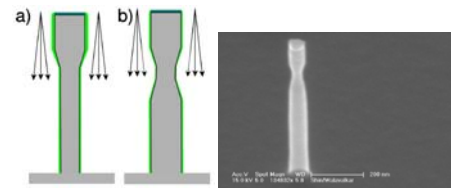
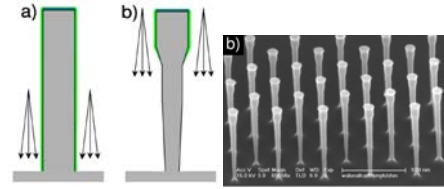
3-dimensional fabrication of structures with nanometer dimensions

Nanostructures can be defined through lithography to sizes as small as 10nm in research laboratories and down to 22nm in modern silicon fabrication lines. These structures, defined by optical or electron beam lithography, are typically etched into the semiconductor substrate to faithfully reproduce the shapes and sizes of the masks with minimal changes in lateral dimension. Recently, we have developed methods to control the etch profile of nanostructures with nanometer control over their lateral dimensions in the vertical – or third dimension. Indeed, structures starting with masks dimensions of 30nm can be controllably undercut to provide constrictions of 10nm by controlling the plasma chemistry and power of the reactive ion etching system (Figure 7). Here we have used this control over the vertical etch profile to define a new class of devices in which the change in geometry leads to a change in band structure.

Indeed, the functions of such devices is very similar to traditional “bandgap engineered” devices such as single or double barrier resonant tunneling devices typically defined within GaAs/AlGaAs or InP/InGaAsP, but instead of using changes in the composition to control the local band structure, we use changes in the geometry of our nano-wires. In such geometrically bandgap engineered structures it becomes possible to observe electron coherence effects without the requirements of complex materials growth.

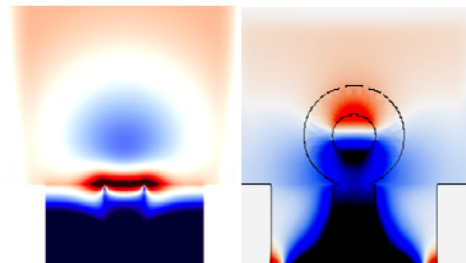


this device, a silicon quantum wire is defined during the etching process to exhibit two narrow regions constricting the channel. In these narrow “barrier” regions, the Si bandgap is higher, and carriers are quantum confined, resulting in a higher bandgap. Between these high bandgap regions, a “quantum dot” is defined which can be gated with a wrap-around metallic gate, made from a plasmonic material. The combination of high optical field intensity with the high electrostatic fields obtained in such nanostructures enables a truly opto-electronic device to be constructed with overall dimensions below 100nm. Such opto-electronic devices can define completely reconfigurable electronic circuits, defined by gate biasing rather than lithography, and these can be optically pumped or interrogated. Conversely, the optical performance (wavelength, emission or absorption efficiency) of these optoelectronic nanodevices can be controlled by the electrostatic gate biases as well as by controlling the refractive index by carrier injection.

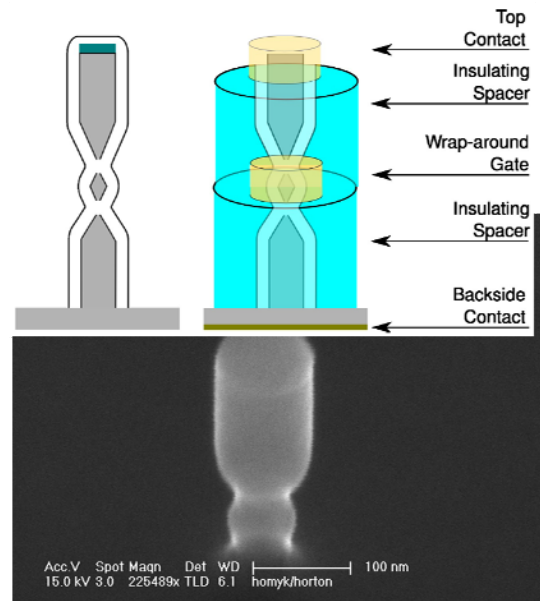


Electron turnstile transistors and quantum devices

Quantum optical systems require both single photon light emitters as well as single photon detectors. One technology that has been suggested for single photon detectors is the “electron turnstile” device, a transistor structure that is excited by single photons. These transistors can be “triggered” by single photons to allow single electrons to pass through a circuit, efficiently converting a quantum signal from the optical to the electrical domain with the lowest possible noise or leakage currents. Our silicon nanostructures are ideal for this task, as they combine control over bandgap by virtue of their size as well as concentration of light through design of their plasmonic geometries. Figure 8 shows the concept of a double barrier resonant tunneling transistor, which can serve this function. In



Under the DARPA/NACHOS program we have developed the concept of new transistor structures (Figure 10) which take advantage of the three-dimensional nano-scale control over both gate and channel geometries. An example of such a device is shown schematically in Figure 9, where we show a resonant tunnel diode, with gates to bias both the quantum well as well as the contact region. The gates again can perform both electrostatic function as well as plasmonic light concentration, and will be defined through multiple metallization steps. Such a structure, we believe, will lead to improvements in both threshold and device speed, and can be manufactured within already existing CMOS fabrication technology. Moreover it is expected to function at room temperature as high barrier heights can be included by appropriate definition of the device geometry.



References

- [1] J. D. Jackson, *Classical Electrodynamics*, 3rd ed. Wiley, New York, 1998.
- [2] A. Yariv, *Quantum Electronics*, 3rd ed. John Wiley & Sons, Inc., 1989.
- [3] E. M. Purcell, "Spontaneous emission probabilities at radio frequencies," *Phys. Rev.*, vol. 69, p. 681, 1946.
- [4] G. Björk and Y. Yamamoto, "Analysis of semiconductor microcavity lasers using rate equations," *IEEE J. Quantum Electron.*, vol. 27, p. 2386, 1991.
- [5] T. Yoshie, M. Loncar, A. Scherer, and Y. M. Qiu, "High frequency oscillation in photonic crystal nanolasers," *Appl. Phys. Lett.*, vol. 84, p. 3543, 2004.
- [6] H. Altug, D. Englund, and J. Vučković, "Ultrafast photonic crystal nanocavity laser," *Nat. Physics*, vol. 2, p. 484, 2006.
- [7] J. L. Jewell, J. P. Harbison, A. Scherer, Y. H. Lee, and L. T. Florez, "Vertical-cavity surface-emitting lasers: design, growth, fabrication, characterization," *IEEE J. Quantum Electron.*, vol. 27, p. 1332, 1991.
- [8] J. M. Gerard, D. Barrier, J. Y. Marzin, R. Kuszelewicz, L. Manin, E. Costard, V. Thierry-Mieg, and T. Rivera, "Quantum boxes as active probes for photonic microstructures: The pillar microcavity case," *Appl. Phys. Lett.*, vol. 69, p. 499, 1996.
- [9] M. Notomi, "Strong light confinement with periodicity," *Proc. IEEE*, vol. 99, p. 1768, 2011.
- [10] J. M. Gerard, B. Sermage, B. Gayral, B. Legrand, E. Costard, and V. Thierry-Mieg, "Enhanced spontaneous emission by quantum boxes in a monolithic optical cavity," *Phys. Rev. Lett.*, vol. 81, p. 1110, 1998.
- [11] J.-M. Gerard and B. Gayral, "Strong Purcell effect for InAs quantum boxes in three-dimensional solid-state microcavities," *J. Lightwave Technol.*, vol. 17, p. 2089, 1999.
- [12] B. Gayral, J.-M. Gerard, B. Sermage, A. Lemaître, and C. Depuis, "Time resolved probing of the Purcell effect for InAs quantum boxes in GaAs microdisks," *Appl. Phys. Lett.*, vol. 78, p. 2828, 2001.
- [13] G. S. Solomon, M. Pelton, and Y. Yamamoto, "Single-mode spontaneous emission from a single quantum dot in a three-dimensional cavity," *Phys. Rev. Lett.*, vol. 86, p. 3903, 2001.
- [14] R. E. Slusher, A. F. J. Levi, U. Mohideen, S. L. McCall, S. J. Pearton, and R. A. Logan, "Threshold characteristics of semiconductor microdisk lasers," *Appl. Phys. Lett.*, vol. 63, p. 1310, 1993.
- [15] O. Painter, R. K. Lee, A. Scherer, A. Yariv, J. D. O'Brien, P. D. Dapkus, and I. Kim, "Two-dimensional photonic band-gap defect mode laser," *Science*, vol. 284, p. 1819, 1999.
- [16] P. Michler, A. Kiraz, L. Zhang, C. Becher, E. Hu, and A. Imamoglu, "Laser emission from quantum dots in microdisk structures," *Appl. Phys. Lett.*, vol. 77, p. 184, 2000.
- [17] H.-G. Park, S.-H. Kim, S.-H. Kwon, Y.-G. Ju, J.-K. Yang, J.-H. Baek, S.-B. Kim, and Y.-H. Lee, "Electrically driven single-cell photonic crystal laser," *Science*, vol. 305, p. 1444, 2004.
- [18] H. Y. Ryu, M. Notomi, E. Kuramoti, and T. Segawa, "Large spontaneous emission factor (> 0.1) in the photonic crystal monopole-mode laser," *Appl. Phys. Lett.*, vol. 84, p. 1067, 2004.
- [19] K. Nozaki, S. Kita, and T. Baba, "Room temperature continuous wave operation and controlled spontaneous emission in ultrasmall photonic crystal nanolaser," *Opt. Express*, vol. 15, p. 7506, 2007.
- [20] M. T. Hill, Y.-S. Oei, B. Smalbrugge, Y. Zhu, T. de Vries, P. J. van Veldhoven, F. W. M. van Otten, T. J. Eijkemans, J. P. Turkiewicz, H. de Waardt, E. J. Geluk, S.-H. Kwon, Y.-H. Lee, R. Nötzel, and M. K. Smit, "Lasing in metallic-coated nanocavities," *Nat. Photonics*, vol. 1, p. 589, 2007.
- [21] G. Björk, A. Karlsson, and Y. Yamamoto, "Definition of a laser threshold," *Phys. Rev. A*, vol. 50, p. 1675, 1994.
- [22] M. P. V. Exter, G. Nienhuis, and J. P. Woerdman, "Two simple expressions for the spontaneous emission factor β ," *Phys. Rev. A*, vol. 54, p. 3553, 1996.
- [23] A. Yariv and P. Yeh, *Photonics: Optical Electronics in Modern Communications*. Oxford University Press, USA, 2007.
- [24] S.-W. Chang and S. L. Chuang, "Normal modes for plasmonic nanolasers with dispersive and inhomogeneous media," *Opt. Lett.*, vol. 34, p. 91, 2009.
- [25] J. J. Li, "Fundamental formulation for plasmonic nanolasers," *IEEE J. Quantum Electron.*, vol. 45, p. 1014, 2009.

- [26] B. E. A. Saleh and M. C. Teich, Fundamentals of Photonics, 2nd ed. John Wiley & Sons, Inc., Hoboken, NJ, 2007.
- [27] J. Huang, S.-H. Kim, and A. Scherer, "Design of a surface-emitting, subwavelength metal-clad disk laser in the visible spectrum," *Opt. Express*, vol. 18, p. 19581, 2010.
- [28] E. D. Palik, ed., Handbook of Optical Constants of Solids I. Academic, San Diego, Calif., 1998.
- [29] N. W. Ashcroft and N. D. Mermin, Solid State Physics. Thomson Learning, Inc., 1976.
- [30] M. Dressel and G. Grüner, Electrodynamics of Solids: Optical Properties of Electrons in Matter. Cambridge University Press, 2002.
- [31] S.-H. Kim, "Reference Manual for pFDTD," 2011, unpublished document. 134
- [32] S.-H. Kim, J. Huang, and A. Scherer, "From vertical-cavities to hybrid metal/photonic-crystal nanocavities: towards high-efficiency nanolasers," *J. Opt. Soc. Am. B*, vol. 29, p. 577, 2012.
- [33] J. W. S. Rayleigh, "On the maintenance of vibrations by forces of double frequency and on the propagation of waves through a medium endowed with a periodic structure," *Phil. Mag.*, vol. 24, p. 145, 1887.
- [34] J. J., "On the reflection of light from a regularly stratified medium," *Proc. R. Soc. A*, vol. 93, p. 565, 1917.
- [35] J. C. Slater, Microwave Electronics. Dover, New York, NY, 1969.
- [36] L. Brillouin, Wave Propagation in Periodic Structures, 2nd ed. Dover Publications, Inc., Mineola, NY, 1953.
- [37] S. L. McCall, P. M. Platzman, R. Dalichaouch, D. Smith, and S. Schultz, "Microwave propagation in two-dimensional dielectric lattices," *Phys. Rev. Lett.*, vol. 67, p. 2017, 1991.
- [38] H. A. Harris and C. V. Shank, "Antisymmetric taper of distributed feedback lasers," *IEEE J. Quantum Electron.*, vol. 15, p. 532, 1976.
- [39] P. Yeh, A. Yariv, and C.-S. Hong, "Electromagnetic propagation in periodic stratified media. I. general theory," *J. Opt. Soc. Am.*, vol. 67, p. 423, 1976.
- [40] P. Yeh, A. Yariv, and E. Marom, "Theory of Bragg grating," *J. Opt. Soc. Am.*, vol. 68, p. 1196, 1978.
- [41] E. Yablonovitch, "Inhibited spontaneous emission in solid-state physics and electronics," *Phys. Rev. Lett.*, vol. 58, p. 2059, 1987.
- [42] S. John, "Strong localization of photons in certain disordered dielectric superlattices," *Phys. Rev. Lett.*, vol. 58, p. 2486, 1987. 135
- [43] S. Y. Lin, J. G. Fleming, D. L. Hetherington, B. K. Smith, R. Biswas, K. M. Ho, M. M. Sigalas, W. Zubrzycki, S. R. Kurtz, and J. Bur, "A three-dimensional photonic crystal operating at infrared wavelengths," *Nature*, vol. 394, p. 251, 1998.
- [44] S. Noda, K. Tomoda, N. Yamamoto, and A. Chutinan, "Full three-dimensional photonic bandgap crystals at near-infrared wavelengths," *Science*, vol. 289, p. 604, 2000.
- [45] K. Aoki, D. Guimard, M. Nishioka, M. Nomura, S. Iwamoto, and Y. Arakawa, "Coupling of quantum-dot light emission with a three-dimensional photonic-crystal nanocavity," *Nature Photonics*, vol. 2, p. 688, 2008.
- [46] A. Tandraechanurat, S. Ishida, K. Aoki, D. Guimard, M. Nomura, S. Iwamoto, and Y. Arakawa, "Demonstration of high-Q (> 8600) three-dimensional photonic crystal nanocavity embedding quantum dots," *Appl. Phys. Lett.*, vol. 2009, p. 171115, 2009.
- [47] J. P. Zhang, D. Y. Chu, S. L. Wu, W. G. Bi, R. C. Tiberio, R. M. Joseph, A. Taove, C. W. Tu, and S. T. Ho, "Nanofabrication of 1-D photonic bandgap structures along a photonic wire," *IEEE Photon. Tech. Lett.*, vol. 8, p. 491, 1996.
- [48] J. S. Foresi, P. R. Villeneuve, J. Ferrera, E. R. Thoen, G. Steinmeyer, S. Fan, J. D. Joannopoulos, L. C. Kimerling, H. I. Smith, and E. P. Ippen, "Photonic bandgap microcavities in optical waveguides," *Nature*, vol. 390, p. 143, 1997.
- [49] Y. Akahane, T. Asano, B.-S. Song, and S. Noda, "High-Q photonic nanocavity in a two-dimensional photonic crystal," *Nature*, vol. 425, p. 944, 2003.
- [50] K. Nozaki and T. Baba, "Laser characteristics with ultimate-small modal volume in photonic crystal slab point-shift nanolasers," *Appl. Phys. Lett.*, vol. 88, p. 211101, 2006.
- [51] S.-H. Kim, S.-K. Kim, and Y.-H. Lee, "Vertical beaming of wavelength-scale photonic crystal resonators," *Phys. Rev. B*, vol. 73, p. 235117, 2006.
- [52] H.-Y. Ryu, M. Notomi, and Y.-H. Lee, "High-quality-factor and small-mode-volume hexapole modes in photonic-crystal-slab nanocavities," *Appl. Phys. Lett.*, vol. 83, p. 4294, 2003. 136
- [53] M. Notomi, T. Tanabe, A. Shinya, E. Kuramochi, H. Taniyama, S. Mitsugi, and M. Morita, "Nonlinear and adiabatic control of high-Q photonic crystal nanocavities," *Opt. Express*,

vol. 15, p. 17458, 2007.

[54] M. Palamaru and P. Lalanne, "Photonic crystal waveguides: out-of-plane losses and adiabatic modal conversion," *Appl. Phys. Lett.*, vol. 78, p. 1466, 2001.

[55] P. Lalanne and J. P. Hugonin, "Bloch-wave engineering for high Qs, small Vs microcavities," *IEEE J. Quantum Electron.*, vol. 39, p. 1430, 2003.

[56] B.-S. Song, S. Noda, T. Asano, and Y. Akahane, "Ultra-high-q photonic double-heterostructure nanocavity," *Nat. Mater.*, vol. 4, p. 207, 2005.

[57] E. Kuramochi, M. Notomi, S. Mitsugi, A. Shinya, and T. Tanabe, "Ultrahigh-q photonic crystal nanocavities realized by the local width modulation of a line defect," *Appl. Phys. Lett.*, vol. 88, p. 041112, 2006.

[58] P. B. Deotare, M. W. McCutcheon, I. W. Frank, M. Khan, and M. Loncar, "High quality factor photonic crystal nanobeam cavities," *Appl. Phys. Lett.*, vol. 94, p. 121106, 2009.

[59] M. Notomi, E. Kuramochi, and H. Taniyama, "Ultrahigh-Q nanocavity with 1D photonic gap," *Opt. Express*, vol. 16, p. 11095, 2008.

[60] B.-H. Ahn, J.-H. Kang, M.-K. Kim, J.-H. Song, B. Min, K.-S. Kim, and Y.-H. Lee, "Onedimensional parabolic-beam photonic crystal laser," *Opt. Express*, vol. 18, p. 5654, 2010.

[61] T. Tanabe, M. Notomi, E. Kuramochi, A. Shinya, and H. Taniyama, "Trapping and delaying photons for one nanosecond in an ultrasmall high-Q photonic-crystal nanocavity," *Nat. Photonics*, vol. 1, p. 49, 2007.

[62] W. L. Barnes, A. Dereux, and T. W. Ebbesen, "Surface plasmon subwavelength optics," *Nature*, vol. 424, p. 824, 2003.

[63] W.-D. Li, F. Ding, J. Hu, and S. Y. Chou, "Three-dimensional cavity nanoantenna coupled plasmonic nanodots for ultrahigh and uniform surface-enhanced raman scattering over large area," *Opt. Express*, vol. 19, p. 3925, 2011.

[64] H. J. Lezec, J. A. Dionne, and H. A. Atwater, "Negative refraction at visible frequencies," *Science*, vol. 316, p. 430, 2007.

[65] J. Valentine, S. Zhang, T. Zentgraf, E. Ulin-Avila, D. A. Genov, G. Bartal, and X. Zhang, "Three-dimensional optical metamaterial with a negative refractive index," *Nature*, vol. 455, p. 376, 2008.

[66] J. D. Joannopoulos and S. G. Johnson, *Photonic Crystals: Molding the Flow of Light*, 2nd ed. Princeton University Press, Princeton, NJ, 2008.

[67] K. Ishizaki and S. Noda, "Manipulation of photons at the surface of three-dimensional photonic crystals," *Nature*, vol. 460, p. 367, 2009.

[68] H.-J. Chang, S.-H. Kim, Y.-H. Lee, E. P. Kartalov, and A. Scherer, "A photonic-crystal optical antenna for extremely large local-field enhancement," *Opt. Express*, vol. 18, p. 24163, 2010.

[69] M. Notomi, "Theory of light propagation in strongly modulated photonic crystals: Refraction like behavior in the vicinity of the photonic band gap," *Phys. Rev. B*, vol. 62, p. 10696, 2000.

[70] M. I. Stockman, "Nanofocusing of optical energy in tapered plasmonic waveguides," *Phys. Rev. Lett.*, vol. 93, p. 137404, 2004.

[71] L. A. Coldren and S. W. Corzine, *Diode Lasers and Photonic Integrated Circuits*. John Wiley & Sons, Inc., 1995.

[72] S.-W. Chang, T.-R. Lin, and S. L. Chuang, "Theory of plasmonic fabry-perot nanolasers," *Opt. Express*, vol. 18, p. 15039, 2010.

[73] M. Fujita, A. Sakai, and T. Baba, "Ultrasmall and ultralow threshold GaInAsP-InP microdisk injection lasers: design, fabrication, lasing characteristics, and spontaneous emission factor," *IEEE J. Sel. Top. Quantum Electron.*, vol. 5, p. 673, 1999.

[74] W. W. Chow, P. M. Smowton, P. Blood, A. Girndt, F. Jahnke, and S. W. Koch, "Comparison of experimental and theoretical GaInP quantum well gain spectra," *Appl. Phys. Lett.*, vol. 71, p. 157, 1997.

[75] K. S. Yee, "Numerical solution of initial boundary value problems involving Maxwell's equations in isotropic media," *IEEE Trans. Antennas Propagat.*, vol. 14, p. 302, 1966.

[76] J. P. Berenger, "A perfectly matched layer for the absorption of electromagnetic waves," *J. Computational Physics*, vol. 114, p. 185, 1994.

[77] M. Okoniewski, M. Mrozowski, and M. A. Stuchly, "Simple treatment of multi-term dispersion in FDTD," *IEEE Microwave Guided Wave Lett.*, vol. 7, p. 121, 1997.

[78] A. Taove and S. C. Hagness, *Computational Electrodynamics|The Finite-Difference Time-*

Domain Method. Artech House, Norwood, 2005.

- [79] J. G. Maloney and G. S. Smith, "The efficient modeling of thin material sheets in the fdtd method," *IEEE Trans. Antennas Propagat.*, vol. 40, p. 323, 1992.
- [80] (2012) Thorlabs, Inc. [Online]. Available: <http://www.thorlabs.us>
- [81] S. L. McCall, A. F. J. Levi, R. E. Slusher, S. J. Pearton, and R. A. Logan, "Whispering-gallery mode microdisk lasers," *Appl. Phys. Lett.*, vol. 60, p. 289, 1991.
- [82] A. F. J. Levi, S. L. McCall, S. J. Pearton, and R. A. Logan, "Room temperature operation of submicrometre radius disk laser," *Electron. Lett.*, vol. 29, p. 1666, 1993.
- [83] K. Srinivasan, M. Borselli, O. Painter, A. Stintz, and S. Krishna, "Cavity Q, mode volume, and lasing threshold in small diameter AlGaAs microdisks with embedded quantum dots," *Opt. Express*, vol. 14, p. 1094, 2006.
- [84] A. F. J. Levi, R. E. Slusher, S. L. McCall, J. L. Glass, S. J. Pearton, and R. A. Logan, "Directional light coupling from microdisk lasers," *Appl. Phys. Lett.*, vol. 62, p. 561, 1993.
- [85] S.-K. Kim, S.-H. Kim, G.-H. Kim, H.-G. Park, D.-J. Shin, and Y.-H. Lee, "Highly directional emission from few-micron-size elliptical microdisks," *Appl. Phys. Lett.*, vol. 84, p. 861, 2004.
- [86] S. Kita, K. Nozaki, S. Hachuda, H. Watanabe, Y. Saito, S. Otsuka, T. Nakada, Y. Arita, and T. Baba, "Photonic crystal point-shift nanolasers with and without nanoslots|design, fabrication, lasing, and sensing characteristics," *IEEE J. Sel. Top. Quantum Electron.*, vol. 17, p. 1632, 2011.
- [87] J. Huang, S.-H. Kim, P. Regreny, C. Seassal, P. A. Postigo, and A. Scherer, "InAsP/InP nanobeam photonic crystal laser with quasi-continuous-wave operation and directional emission," 2012, manuscript in preparation.
- [88] C. A. Balanis, *Advanced Engineering Electromagnetics*. Wiley, New York, 1989.
- [89] J. Vuckovic, M. Loncar, H. Mabuchi, and A. Scherer, "Optimization of the q factor in photonic crystal microcavities," *IEEE J. Quantum Electron.*, vol. 38, p. 850, 2002.
- [90] O. Painter, J. Vuckovic, and A. Scherer, "Defect modes of a two-dimensional photonic crystal in an optically thin dielectric slab," *J. Opt. Soc. Am. B*, vol. 16, p. 275, 1999.
- [91] L. A. Graham, D. L. Huffaker, and D. G. Deppe, "Spontaneous lifetime control in a nativeoxide-apertured microcavity," *Appl. Phys. Lett.*, vol. 74, p. 2408, 1999.
- [92] Y. Yamamoto and S. Machida, "Microcavity semiconductor laser with enhanced spontaneous emission," *Phys. Rev. A*, vol. 44, p. 657, 1991.
- [93] H. Yokoyama and S. D. Brorson, "Rate equation analysis of microcavity lasers," *J. Appl. Phys.*, vol. 66, p. 4801, 1989.
- [94] H. Yokoyama, "Physics and device application of optical microcavities," *Science*, vol. 256, p. 66, 1992.
- [95] J. Gerard and B. Gayral, "Toward high-efficiency quantum-dot single-photon sources," *Proc. SPIE*, vol. 5361, p. 88, 2004.
- [96] K. Inoshita and T. Baba, "Fabrication of GaInAsP/InP photonic crystal lasers by ICP etching and control of resonant mode in point and line composite defects," *IEEE J. Sel. Top. Quantum Electron.*, vol. 9, p. 1347, 2003.
- [97] J. K. Hwang, H. Y. Ryu, D. S. Song, I. Y. Han, H. K. Park, D. H. Jang, and Y. H. Lee, "Continuous room-temperature operation of optically pumped two-dimensional photonic crystal lasers at 1.6 μm ," *IEEE Photon. Technol. Lett.*, vol. 12, p. 1295, 2000.
- [98] J. Cao, W. Kuang, Z.-J. Wei, S.-J. Choi, H. Yu, M. Bagheri, J. O'Brien, and P. Dapkus, "Sapphire-bonded photonic crystal microcavity lasers and their far-field radiation patterns," *IEEE Photon. Technol. Lett.*, vol. 17, p. 4, 2005.
- [99] O. J. Painter, "Optical nanocavities in two-dimensional photonic crystal planar waveguides," Ph.D. dissertation, California Institute of Technology, Pasadena, CA, 2001.
- [100] S. G. Johnson, S. Fan, P. R. Villeneuve, J. D. Joannopoulos, and L. A. Kolodziejaki, "Guided modes in photonic crystal slabs," *Phys. Rev. B*, vol. 60, p. 5751, 1999.
- [101] S.-H. Kim, J. Huang, and A. Scherer, "A photonic crystal nanocavity laser in an optically very thick slab," *Opt. Lett.*, vol. 37, p. 488, 2012.
- [102] J. Huang, S.-H. Kim, J. Gardner, P. Regreny, C. Seassal, P. A. Postigo, and A. Scherer, "Room temperature, continuous-wave coupled-cavity InAsP/InP photonic crystal laser with enhanced far-field emission directionality," *Appl. Phys. Lett.*, vol. 99, p. 091110, 2011.
- [103] P. B. Johnson and R. W. Christy, "Optical constants of the noble metals," *Phys. Rev. B*,

vol. 6, p. 4370, 1972.

[104] J. A. Dionne, L. A. Sweatlock, and H. A. Atwater, \Plasmon slot waveguides: Towards chipscale propagation with subwavelength-scale localization," *Phys. Rev. B*, vol. 73, p. 035407, 2006.

[105] H. T. Miyazaki and Y. Kurokawa, \Controlled plasmon resonance in closed metal/insulator/metal nanocavities," *Appl. Phys. Lett.*, vol. 89, p. 211126, 2006.141

[106] A. Hosseini and Y. Massoud, \Nanoscale surface plasmon based resonator using rectangular geometry," *Appl. Phys. Lett.*, vol. 90, p. 181102, 2007.

[107] K. Yu, A. Lakhani, and M. C. Wu, \Subwavelength metal-optic semiconductor nanopatch lasers," *Opt. Express*, vol. 18, p. 8790, 2010.

[108] J.-C. Weeber, A. Bouhelier, G. C. des Francs, L. Markey, and A. Dereux, \Submicrometer in-plane integrated surface plasmon cavities," *Nano Lett.*, vol. 7, p. 1352, 2007.

[109] A. Mizrahi, V. Lomakin, B. A. Slutsky, M. P. Nezhad, L. Feng, and Y. Fainman, \Low threshold gain metal coated laser nanoresonators," *Opt. Lett.*, vol. 33, p. 1261, 2008.

[110] M. P. Nezhad, A. Simic, O. Bondarenko, B. Slutsky, A. Mizrahi, L. Feng, V. Lomakin, , and Y. Fainman, \Room-temperature subwavelength metallo-dielectric lasers," *Nat. Photonics*, vol. 4, p. 395, 2010.

[111] Y. Arakawa and H. Sakaki, \Multidimensional quantum well laser and temperature dependence of its threshold current," *Appl. Phys. Rev.*, vol. 40, p. 939, 1982.

[112] T. Baba, \Photonic crystals and microdisk cavities based on GaInAsP-InP system," *IEEE J. Sel. Top. Quantum Electron.*, vol. 3, p. 808, 1997.

[113] Z. Zhang, L. Yang, V. Liu, T. Hong, K. Vahala, and A. Scherer, \Visible submicron microdisk lasers," *Appl. Phys. Lett.*, vol. 90, p. 111119, 2007.

[114] Q. Song, H. Cao, S. T. Ho, and G. S. Solomon, \Near-IR subwavelength microdisk lasers," *Appl. Phys. Lett.*, vol. 94, p. 061109, 2009.

[115] (2001) Io_e physico-technical institute electronic archive of new semiconductor materials, characteristics, and properties. [Online]. Available: http://www.io_e.ru/SVA/NSM

[116] C. E. Hofmann, E. J. R. Vesseur, L. A. Sweatlock, H. J. Lezec, F. J. G. de Abajo, A. Polman, and H. A. Atwater, \Plasmonic modes of annular nanoresonators imaged by spectrally resolved cathodoluminescence," *Nano Lett.*, vol. 7, p. 3612, 2007. 142

[117] H. Kato, S. Adachi, H. Nakanishi, and K. Ohtsuka, \Optical properties of $(\text{Al}_x\text{Ga}_{1-x})_{0.5}\text{In}_{0.5}\text{P}$ quaternary alloys," *Jpn. J. Appl. Phys.*, vol. 33, p. 186, 1994.

[118] G. Hunziker, W. Knop, and C. Harder, \Gain measurement on one, two, and three strained GaInP quantum well laser diodes," *IEEE Trans. Quantum Electron.*, vol. 30, p. 2235, 1994.

[119] M. T. Hill, M. Marell, E. S. P. Leong, B. Smalbrugge, Y. Zhu, M. Sun, P. J. van Veldhoven, E. J. Geluk, F. Karouta, Y.-S. Oei, R. Nötzel, C.-Z. Ning, and M. K. Smit, \Lasing in metalinsulator-metal sub-wavelength plasmonic waveguides," *Opt. Express*, vol. 17, p. 11107, 2009.

[120] F. Qian, Y. Li, S. Gradecak, H.-G. Park, Y. Dong, Y. Ding, Z. L. Wang, and C. M. Lieber, \Multi-quantum-well nanowire heterostructures for wavelength-controlled lasers," *Nat. Mater.*, vol. 7, p. 701, 2008.

[121] E. F. Schubert, Y.-H. Wang, A. Y. Cho, L.-W. Tu, and G. J. Zydzik, \Resonant cavity lightemitting diode," *Appl. Phys. Lett.*, vol. 60, p. 1992, 1992.

[122] H. Benisty, H. D. Neve, and C. Weisbuch, \Impact of planar microcavity e_ects on light extraction|Part I: basic concepts and analytical trends," *IEEE J. Quantum Electron.*, vol. 34, p. 1612, 1998.

[123] R. A. Matula, \Electrical resistivity of copper, gold, palladium, and silver," *J. Phys. Chem. Ref. Data*, vol. 8, p. 1147, 1979.

[124] S. Strauf, K. Hennessy, M. T. Rakher, Y.-S. Choi, A. Badolato, L. C. Andreani, E. L. Hu, P. M. Petro_, and D. Bouwmeester, \Self-tuned quantum dot gain in photonic crystal lasers," *Phys. Rev. Lett.*, vol. 96, 2006.

[125] Y. Akahane, T. Asano, B.-S. Song, and S. Noda, \Fine-tuned high-Q photonic-crystal nanocavity," *Opt. Express*, vol. 13, p. 1202, 2005.

[126] M. Loncar, M. Hochberg, A. Scherer, and Y. Qiu, \High quality factors and room-temperature lasing in a modi_ed single-defect photonic crystal cavity," *Opt. Lett.*, vol. 29, p. 721, 2004.143

[127] M. Fujita, A. Sugitatsu, T. Uesugi, and S. Noda, \Fabrication of indium phosphide compound photonic crystal by hydrogen iodide/xenon inductively coupled plasma etching," *Jpn. J. Appl. Phys.*, vol. 43, p. L1400, 2004.

- [128] K. Srinivasan, P. Barclay, and O. Painter, "Fabrication-tolerant high quality factor photonic crystal microcavities," *Opt. Express*, vol. 12, p. 1458, 2004.
- [129] J. P. Dowling, M. Scully, and F. DeMartini, "Radiation pattern of a classical dipole in a cavity," *Opt. Comm.*, vol. 82, p. 415, 1991.
- [130] S. Fan and J. D. Joannopoulos, "Analysis of guided resonances in photonic crystal slabs," *Phys. Rev. B*, vol. 65, p. 235112, 2002.
- [131] T. Baba and D. Sano, "Low threshold lasing and Purcell effect in microdisk lasers at room temperature," *IEEE J. Sel. Top. Quantum Electron.*, vol. 9, p. 1340, 2003.
- [132] A. Tandaechanurat, S. Iwamoto, M. Nomura, N. Kumagai, and Y. Arakawa, "Increase of Q-factor in photonic crystal H1-defect nanocavities after closing of photonic bandgap with optimal slab thickness," *Opt. Express*, vol. 16, p. 448, 2008.
- [133] H. Altug and J. Vučković, "Photonic crystal nanocavity array laser," *Opt. Express*, vol. 13, p. 8819, 2005.
- [134] A. R. Alija, L. J. Martinez, P. A. Postigo, C. Seassal, and P. Viktorovitch, "Coupled-cavity two-dimensional photonic crystal waveguide ring laser," *Appl. Phys. Lett.*, vol. 89, p. 101102, 2006.
- [135] K. Nozaki, H. Watanabe, and T. Baba, "Photonic crystal nanolaser monolithically integrated with passive waveguide for effective light extraction," *Appl. Phys. Lett.*, vol. 92, p. 021108, 2008.
- [136] N.-V.-Q. Tran, S. Combrie, and A. D. Rossi, "Directive emission from high-Q photonic crystal cavities through band folding," *Phys. Rev. B*, vol. 79, p. 041101(R), 2009.144
- [137] J.-H. Kang, M.-K. Seo, S.-K. Kim, S.-H. Kim, M.-K. Kim, H.-G. Park, K.-S. Kim, and Y.-H. Lee, "Polarized vertical beaming of an engineered hexapole mode laser," *Opt. Express*, vol. 17, p. 6074, 2009.
- [138] P. B. Deotare, M. W. McCutcheon, I. W. Frank, M. Khan, and M. Loncar, "Coupled photonic crystal nanobeam cavities," *Appl. Phys. Lett.*, vol. 95, p. 031102, 2009.
- [139] I. W. Frank, P. B. Deotare, M. W. McCutcheon, and M. Loncar, "Programmable photonic crystal nanobeam cavities," *Opt. Express*, vol. 18, p. 8705, 2010.
- [140] M. Eicheneld, R. Camacho, J. Chan, K. J. Vahala, and O. Painter, "A picogram- and nanometre-scale photonic crystal optomechanical cavity," *Nature*, vol. 459, p. 550, 2009.
- [141] T. P. M. Alegre, R. Perahia, and O. Painter, "Optomechanical zipper cavity lasers: theoretical analysis of tuning range and stability," *Opt. Express*, vol. 18, p. 7872, 2010.
- [142] S. Fan, J. N. Winn, A. Devenyi, J. C. Chen, R. D. Meade, and J. D. Joannopoulos, "Guided and defect modes in periodic dielectric waveguides," *J. Opt. Soc. Am. B*, vol. 12, p. 1267, 1995.
- [143] P. Lalanne, S. Mias, and J. P. Hugonin, "Two physical mechanisms for boosting the quality factor to cavity volume ratio of photonic crystal microcavities," *Opt. Express*, vol. 12, p. 458, 2004.
- [144] C. Sauvan, G. Lecamp, P. Lalanne, and J. P. Hugonin, "Modal-reactivity enhancement by geometry tuning in photonic crystal microcavities," *Opt. Express*, vol. 13, p. 245, 2005.
- [145] C. Sauvan, P. Lalanne, and J. P. Hugonin, "Slow-wave effect and mode-profile matching in photonic crystal microcavities," *Phys. Rev. B*, vol. 71, p. 165118, 2005.
- [146] R. D. Meade, A. M. Rappe, K. D. Brommer, and J. D. Joannopoulos, "Nature of the photonic band gap: some insights from a field analysis," *J. Opt. Soc. Am. B*, vol. 10, p. 328, 1993.145
- [147] Y. Tanaka, T. Asano, Y. Akahane, B.-S. Song, and S. Noda, "Theoretical investigation of a two-dimensional photonic crystal slab with truncated cone air holes," *Appl. Phys. Lett.*, vol. 82, p. 1661, 2003.
- [148] M.-K. Kim, J.-K. Yang, Y.-H. Lee, and I.-K. Hwang, "Influence of etching slope on two-dimensional photonic crystal slab resonators," *J. Korean Phys. Soc.*, vol. 5, p. 1027, 2007.
- [149] S. G. Johnson, S. Fan, A. Mekis, and J. D. Joannopoulos, "Multipole-cancellation mechanism for high-Q cavities in the absence of a complete photonic band gap," *Appl. Phys. Lett.*, vol. 78, p. 3388, 2001.
- [150] K. Srinivasan and O. Painter, "Momentum space design of high-Q photonic crystal optical cavities," *Opt. Express*, vol. 10, p. 670, 2002.
- [151] U. K. Khankhoje, S.-H. Kim, B. C. Richards, J. Hendrickson, J. Sweet, J. D. Olitzky, G. Khitrova, H. M. Gibbs, and A. Scherer, "Modelling and fabrication of GaAs photonic-crystal cavities for cavity quantum electrodynamics," *Nanotechnology*, vol. 21, p. 065202, 2010.
- [152] (2012) Wolfram Alpha. [Online]. Available: <http://www.wolframalpha.com>
- [153] S. Budavari, ed., *The Merck index: an encyclopedia of chemicals, drugs, and biologicals*, 11th ed. Merck, Rahway, NJ, 1989.

- [154] E. A. Peretti, "Thermal analysis of the indium-iodine system," *J. Am. Chem. Soc.*, vol. 78, p. 5745, 1956.
- [155] I. Junarsa, M. P. Stoykovich, P. F. Nealey, Y. Ma, F. Cerrina, and H. H. Solak, "Hydrogen silsesquioxane as a high resolution negative-tone resist for extreme ultraviolet lithography," *J. Vac. Sci. Technol. B*, vol. 23, p. 138, 2005.
- [156] H. Namatsu, Y. Takahashi, K. Yamazaki, T. Yamaguchi, M. Nagase, and K. Kurihara, "Threedimensional siloxane resist for the formation of nanopatterns with minimum linewidth fluctuations," *J. Vac. Sci. Technol. B*, vol. 16, p. 69, 1998.
- [157] T. Nakamura, M. Sasaki, A. Kobayashi, K. Sawa, and K. Mine, "Oxidative curing of hydrogen silsesquioxane resin films by electron beam irradiation without additional heatings and characterization of the cured films," *Jpn. J. Appl. Phys.*, vol. 40, p. 6187, 2001.
- [158] D. P. Mancini, K. A. Gehoski, E. Ainley, K. J. Nordquist, D. J. Resnick, T. C. Bailey, S. V. Sreenivasan, J. G. Ekerdt, and C. G. Willson, "Hydrogen silsesquioxane for direct electronbeam patterning of step and ash imprint lithography templates," *J. Vac. Sci. Technol. B*, vol. 20, p. 2896, 2002.
- [159] C.-C. Yang and W.-C. Chen, "The structures and properties of hydrogen silsesquioxane (HSQ) films produced by thermal curing," *J. Mater. Chem.*, vol. 12, p. 1138, 2002.
- [160] K. Srinivasan, P. E. Barclay, O. Painter, J. Chen, and A. Y. Cho, "Fabrication of high-quality-factor photonic crystal microcavities in InAsP/InGaAsP membranes," *J. Vac. Sci. Technol. B*, vol. 22, p. 875, 2004.
- [161] H. Huang, X. Wang, X. Ren, Q. Wang, and Y. Huang, "Selective wet etching of In-GaAs/InGaAsP in HCl/HF/CrO₃ solution: application to vertical taper structures in integrated optoelectronic devices," *J. Vac. Sci. Technol. B*, vol. 23, p. 1650, 2005.
- [162] A. F. J. Levi, R. E. Slusher, S. L. McCall, T. Tanbun-Ek, D. L. Coblenz, and S. J. Pearton, "Room temperature operation of microdisc lasers with submilliamp threshold current," *Electron. Lett.*, vol. 28, p. 1010, 1992.
- [163] T. Baba, P. Fujita, A. Sakai, M. Kihara, and R. Watanabe, "Lasing characteristics of GaInAsP/InP strained quantum-well microdisk injection lasers with diameter of 2-10 μ m," *IEEE Photonics Technol. Lett.*, vol. 9, p. 878, 1997.
- [164] G. Björk, A. Karlsson, and Y. Yamamoto, "On the linewidth of microcavity lasers," *Appl. Phys. Lett.*, vol. 60, p. 304, 1992.
- [165] R. J. Glauber, "The quantum theory of optical coherence," *Phys. Rev.*, vol. 130, p. 2529, 1963.
- [166] R. Jin, D. Boggavarapu, M. Sargent, P. Meystre, H. M. Gibbs, and G. Khitrova, "Photon-number correlations near the threshold of microcavity lasers in the weak-coupling regime," *Phys. Rev. A*, vol. 49, p. 4038, 1994.
- [167] S. M. Ulrich, C. Gies, S. Ates, J. Wiersig, S. Reitzenstein, C. Hofmann, A. Löffler, A. Forchel, F. Jahnke, and P. Michler, "Photon statistics of semiconductor microcavity lasers," *Phys. Rev. Lett.*, vol. 98, p. 043906, 2007.
- [168] L. J. Martinez, B. Alen, I. Prieto, D. Fuster, L. Gonzalez, Y. Gonzalez, M. L. Dotor, and P. A. Postigo, "Room temperature continuous wave operation in a photonic crystal microcavity laser with a single layer of InAs/InP self-assembled quantum wires," *Opt. Express*, vol. 17, p. 14993, 2009.
- [169] K. Tanabe, M. Nomura, D. Guimard, S. Iwamoto, and Y. Arakawa, "Room temperature continuous wave operation of InAs/GaAs quantum dot photonic crystal nanocavity laser on silicon substrate," *Opt. Express*, vol. 17, p. 7036, 2009.
- [170] S. W. Corzine, R.-H. Yan, and L. A. Coldren, *Optical gain in III-V bulk and quantum well semiconductors*. Academic Press, Inc., San Diego, CA, 1993.
- [171] S. Y. Hu, S. W. Corzine, K. K. Law, D. B. Young, A. C. Gossard, L. A. Coldren, and J. L. Merz, "Lateral carrier diffusion and surface recombination in InGaAs/AlGaAs quantum well ridge waveguide lasers," *J. Appl. Phys.*, vol. 76, p. 4479, 1994.
- [172] M. E. Heimbuch, J. A. L. Holmes, C. M. Reaves, M. P. Mack, S. P. DenBaars, and L. A. Coldren, "Tertiarybutylarsine and tertiarybutylphosphine for the MOCVD growth of low threshold 1.55 μ m In_xGa_{1-x}As/InP quantum-well lasers," *J. Electron. Mater.*, vol. 23, p. 87, 1994.
- [173] C. J. Sandro, R. N. Nottenburg, J.-C. Bischoff, and R. Bhat, "Dramatic enhancement in the gain of a GaAs/AlGaAs heterostructure bipolar transistor by surface chemical passivation," *Appl. Phys. Lett.*, vol. 51, p. 33, 1987.
- [174] S. R. Lunt, G. N. Fiyba, P. G. Santangelo, and N. S. Lewis, "Chemical studies of the passivation

of GaAs surface recombination using sulfides and thiols," J. Appl. Phys., vol. 70, p. 7449, 1991.

[175] D. Englund, H. Altug, and J. Vuckovic, "Low-threshold surface-passivated photonic crystal nanocavity laser," Appl. Phys. Lett., vol. 91, p. 071124, 2007.

[176] M. Boroditsky, R. Vrijen, V. F. Krauss, R. Coccioli, R. Bhat, and E. Yablonovitch, "Spontaneous emission and Purcell enhancement from thin-film 2-D photonic crystals," J. Lightwave Technol., vol. 17, p. 2096, 1999.

[177] T. Baba, K. Inoshita, H. Tanaka, J. Yonekura, M. Ariga, A. Matsutani, T. Miyamoto, F. Koyama, and K. Iga, "Strong enhancement of light extraction efficiency in GaInAsP 2-D-arranged microcolumns," J. Lightwave Technol., vol. 17, p. 2113, 1999.

[178] W. Shockley and J. W. T. Read, "Statistics of the recombinations of holes and electrons," Phys. Rev., vol. 87, p. 835, 1952.

[179] R. N. Hall, "Electron-hole recombination in germanium," Phys. Rev., vol. 87, p. 387, 1952.

[180] H.-Y. Ryu, J.-K. Hwang, D.-S. Song, I.-Y. Han, and Y.-H. Lee, "Effect of nonradiative recombination on light emitting properties of two dimensional photonic crystal slab structures," Appl. Phys. Lett., vol. 78, p. 1174, 2001.

[181] V. Swaminathan, J. M. Freund, L. M. F. Chirovsky, T. D. Harris, N. A. Kuebler, and L. A. D'Asaro, "Evidence for surface recombination at mesa sidewalls of self-electro-optic effect devices," J. Appl. Phys., vol. 68, p. 4116, 1990.

[182] D. D. Nolte, "Surface recombination, free-carrier saturation, and dangling bonds in InP and GaAs," Solid-State Electron., vol. 33, p. 295, 1990.

[183] B. Sermage, H. J. Eichler, J. P. Heritage, R. J. Nelson, and N. K. Dutta, "Photoexcited carrier lifetime and Auger recombination in 1.3 μm InGaAsP," Appl. Phys. Lett., vol. 42, p. 259, 1983.

[184] E. Wintner and E. P. Ippen, "Nonlinear carrier dynamics in $\text{Ga}_{1-x}\text{In}_x\text{As}_y\text{P}_{1-y}$ compounds," Appl. Phys. Lett., vol. 44, p. 99, 1984.

[185] H. Watanabe, K. Nozaki, and T. Baba, "Very wide wavelength chirping in photonic crystal nanolaser," in Int. Symp. Compound Semicond., Kyoto, Japan, October 2007, p. TuC 9.

[186] G. Dagnall, J.-J. Shen, T.-H. Kim, R. A. Metzger, A. S. Brown, and S. R. Stock, "Solid source MBE growth of InAsP/InP quantum wells," J. Electron. Mater., vol. 28, p. 933, 1999.

[187] J. A. McCaulley, V. M. Donnelly, M. Vernon, and I. Taha, "Temperature dependence of the near-infrared refractive index of silicon, gallium arsenide, and indium phosphide," Phys. Rev. B, vol. 49, p. 7408, 1994.

[188] F. G. D. Corte, G. Cocorullo, M. Iodice, and I. Rendina, "Temperature dependence of the thermo-optic coefficient of InP, GaAs, and SiC from room temperature to 600 K at the wavelength of 1.5 μm ," Appl. Phys. Lett., vol. 77, p. 1614, 2000.

[189] A. R. Adams, M. Asada, Y. Suematsu, and S. Arai, "The temperature dependence of the efficiency and threshold current of $\text{In}_{1-x}\text{Ga}_x\text{As}_y\text{P}_{1-y}$ lasers related to intervalence band absorption," Jpn. J. Appl. Phys., vol. 19, p. L621, 1980.

[190] Y. Zhang, M. Khan, Y. Huang, J. Ryou, P. Deotare, R. Dupuis, and M. Loncar, "Photonic crystal nanobeam lasers," Appl. Phys. Lett., vol. 97, p. 051104, 2010.

[191] Y. Gong, B. Ellis, G. Shambat, T. Sarmiento, J. S. Harris, and J. Vuckovic, "Nanobeam photonic crystal cavity quantum dot laser," Opt. Express, vol. 18, p. 8781, 2010.